HITACHI
Inspire the Next

SCIENTIFIC INSTRUMENT NEWS

Vol. 21

MARCH 2024

CONTENTS

March 2024 Vol.21

«Column

«Article

«Technical Explanation

«Topics

«Interview

SCIENTIFIC INSTRUMENT NEWS
2024 Vol.21 MARCH
Technical magazine of Electron Microscope and Analytical Instruments.
Column

Analysis of Chiral Amino Acids in Extraterrestrial Samples Using Multi-dimensional HPLC

Kenji Hamase
PhD
Professor
Department of Drug Discovery and Evolution
Graduate School of Pharmaceutical Sciences
Kyushu University

1. Introduction: Amino Acids in Extraterrestrial Samples

Amino acids are a basic family of molecules in living organisms. With the exception of the irregular case of glycine, the carbon atom at the α site of each amino acid serves as an asymmetric center. Due to the presence of this asymmetric carbon, two inequivalent forms exist, known as *enantiomers* called D- and L-forms. Amino acids are believed to have been synthesized by chemical reactions in the primitive Earth, and these chemical reactions normally produce the two enantiomers in equal proportion, yielding a 50/50 blend of D-form and L-form molecules known as a *racemic mixture*.

However, the amino acids found in living organisms on Earth today are mostly L-forms, a phenomenon known as *homochirality* whose origin remains unclear. In the study of *extraterrestrial* samples, the Murchison meteorite, which fell in the Australian village of Murchison in 1969, was discovered to contain a variety of amino acids. The finding suggested the possibility that amino acids on Earth may have extraterrestrial origins. It was also reported that some of the amino acids contained in the meteorite were predominantly L-forms, and a hypothesis that the homochirality was itself of extraterrestrial origin was inspired. Therefore, accurate analysis of chiral amino acids in extraterrestrial samples is expected. However, extraterrestrial samples collected on Earth may be contaminated by some proportion of terrestrial amino acids (L-form rich), and this concern has motivated the planning of *sample-return missions* to collect samples from cosmic space and return them to Earth.

However, the test specimens available from extraterrestrial samples are limited, and many varieties of organic compounds are present in these samples due to radical reactions occurring in extraterrestrial space. Therefore, the development of analytical methods capable of quantifying chiral amino acids with high sensitivity and high selectivity is required. In this work we developed a multi-dimensional HPLC system for the accurate determination of chiral amino acids in many types of extraterrestrial samples, and applied it to the analysis of meteorites and asteroids.

2. Multi-dimensional HPLC

In the extraterrestrial samples, we focus on the determination of five aliphatic amino acids shown in Figure 1: the proteinogenic amino acids alanine (Ala) and valine (Val), and the non-proteinogenic amino acids 2-aminobutyric acid (2AB), norvaline (Nva), and isovaline (Iva). These amino acids are heated for 2 min at 60°C in the presence of Na-borate buffer (pH 8.0) after adding 4-fluoro-7-nitro-2,1,3-benzoxadiazole (NBD-F) to yield fluorescent derivatives. Then the reaction is terminated by adding an aqueous trifluoroacetic acid (TFA) solution and a portion of this reaction mixture is analyzed by a multi-dimensional HPLC system. The analytical instrument is a three-dimensional HPLC system equipped with three types of separation columns: reversed-phase, anion-exchange, and enantioselective columns. For each dimension, fluorescence detection is carried out (excitation wavelength 470 nm, emission wavelength 530 nm).

Figure 2 shows a flow diagram of the three-dimensional HPLC system. By the reversed-phase column in the first dimension, the target amino acids are separated from other amino acids and interfering substances based on differences in hydrophobicity. After separation, the targeted amino acids are collected online as the mixtures of D- and L-forms, and entire volumes of the collected fractions are injected into the second-dimension anion-exchange column. In this column, the components that eluted together with targeted amino acids from the first-dimension column are separated via electrostatic interaction. The targeted amino acids are again collected online as the mixtures of D- and L-forms, and the entire volumes of the mixtures are injected into the third-dimension enantioselective column. In the third-dimension, the D- and L-forms of amino acids are separated and determined. For the first-dimension, a reversed-phase column (Singularity RP18, 1.0 mm ID × 250 mm) is adopted, and the gradient elution using 5-25% aqueous acetonitrile solutions containing 0.025% TFA is carried out. For the second-dimension, a Singularity AX column (1.0 mm ID × 150 mm) is used, and mixed solutions of methanol and acetonitrile (50/50, v/v) containing 0.03% or 0.06% formic acid are selected as the mobile phases. For the third-dimension, a Singularity CSP-001S column (1.5 mm ID × 500 mm) is adopted. For the enantiomer separations of Ala, Val, 2AB, and Nva, a mixture of methanol and acetonitrile (50/50, v/v) containing 0.2% formic acid is used as a mobile phase. For the enantiomer separation of Iva, a mixture of methanol and acetonitrile (90/10, v/v) containing 0.1% formic acid is used. All of these Singularity columns are developed in collaboration with KAGAMI Inc. (Osaka, Japan).

The three-dimensional HPLC system was validated using standard amino acids. The calibration curves showed good linearity (correlation coefficients of 0.9993 or higher) over a concentration range from 5 fmol to 5 pmol per injection. High precision with RSD values in the range 1.33-8.77% was also obtained. For meteorite samples, we obtained high precision with RSD values in the range 3.21-7.84% and accuracy values were in the range 96.6-106.8%, demonstrating that the three-dimensional HPLC technique is applicable to measure chiral amino acids accurately in extraterrestrial samples.

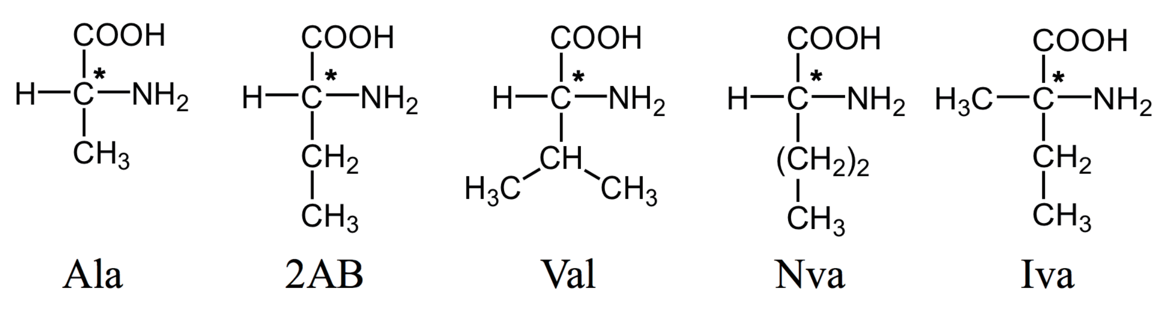

Fig. 1 Structures of target amino acids.

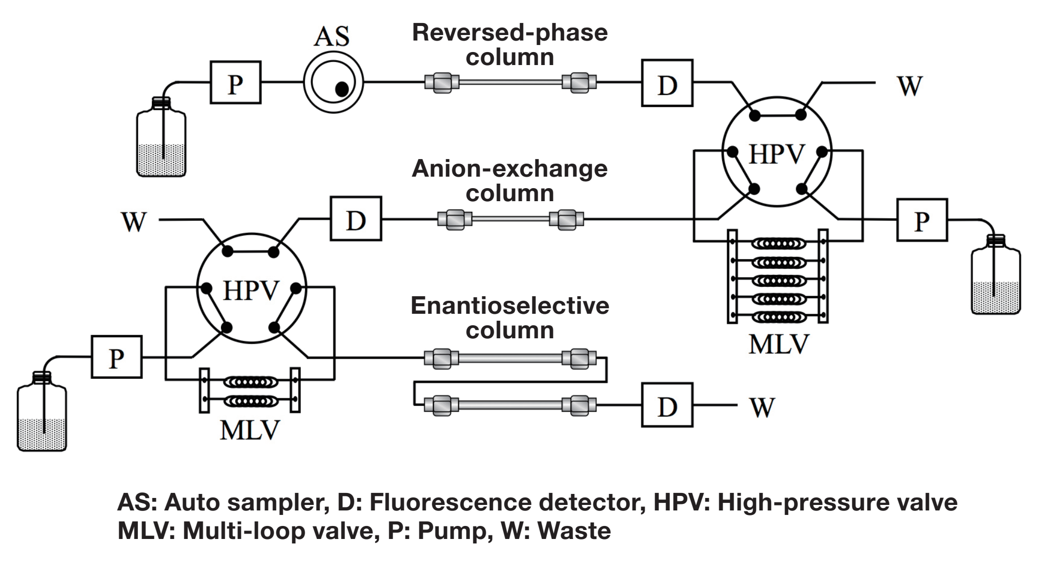

AS: Auto sampler, D: Fluorescence detector, HPV: High-pressure valve
MLV: Multi-loop valve, P: Pump, W: Waste

Fig. 2 Flow diagram of the three-dimensional HPLC system.

3. Analysis of Meteorite and Asteroid Samples

Organic molecules were extracted from meteorites and other extraterrestrial samples in hot water for 20 h, followed by the hydrolysis at 105°C in 6M aqueous hydrochloric acid for 20 h, then dried under reduced pressure. The residue was re-dissolved in water and neutralized by an aqueous sodium-hydroxide solution. Then, Na-borate buffer and NBD-F were added to yield fluorescent derivatives. After adding an aqueous TFA solution to terminate the reaction, a portion of the reaction mixture was subjected to the three-dimensional HPLC. To avoid contamination of terrestrial amino acids, glassware and vessels were heated at 500°C for 4 h. Figure 3 shows results analyzing the Yamato 002540 meteorite collected in the area of the Yamato mountains in Antarctica. In the results for the reversed-phase separation in the first dimension (Figure 3, upper), a variety of peaks for other substances is observed in addition to peaks for the target amino acids. The fractions for the target amino acids (indicated by solid black underlines in the figure) are collected online, and introduced into the second-dimension. In the results for anion-exchange separation representing the second-dimension (Figure 3, middle), several peaks corresponding to substances other than the targeted amino acids are still observed. The fractions of the target amino acids (indicated by solid black underlines) are again collected online, and introduced into the third-dimension to separate the D- and L-forms of amino acids by the enantioselective column. In the chromatograms of the third-dimension (Figure 3, bottom), the enantiomers of interest are clearly detected with no coexisting components, and the D- and L-forms are present in a roughly 50/50 blend.

Figure 4 shows the chromatograms obtained in the third-dimension enantioselective separation for a sample from the asteroid Ryugu collected by the Hayabusa 2 spacecraft. These results indicate that our technique can clearly identify and determine five amino acids of interest in the Ryugu particles. Concerning the enantiomer ratios, the D- and L-forms of alanine are present in roughly equal proportion; however, the L-form of valine is more abundant than the D-form. This may be due to the contamination of terrestrial amino acids. Although alanine and valine are both proteinogenic amino acids, extraterrestrial samples contain only small quantities of valine, making the effects of contamination non-negligible for this case. The non-proteinogenic amino acids (2-aminobutyric acid, norvaline, and isovaline) were present as almost racemic mixtures with D- and L-forms in roughly equal proportion. The fact that non-proteinogenic amino acids are almost entirely nonexistent on Earth avoids the problem of terrestrial contamination, and allows the accurate analyses of these amino acids reflecting the enantiomer ratios for amino acids in extraterrestrial specimens.

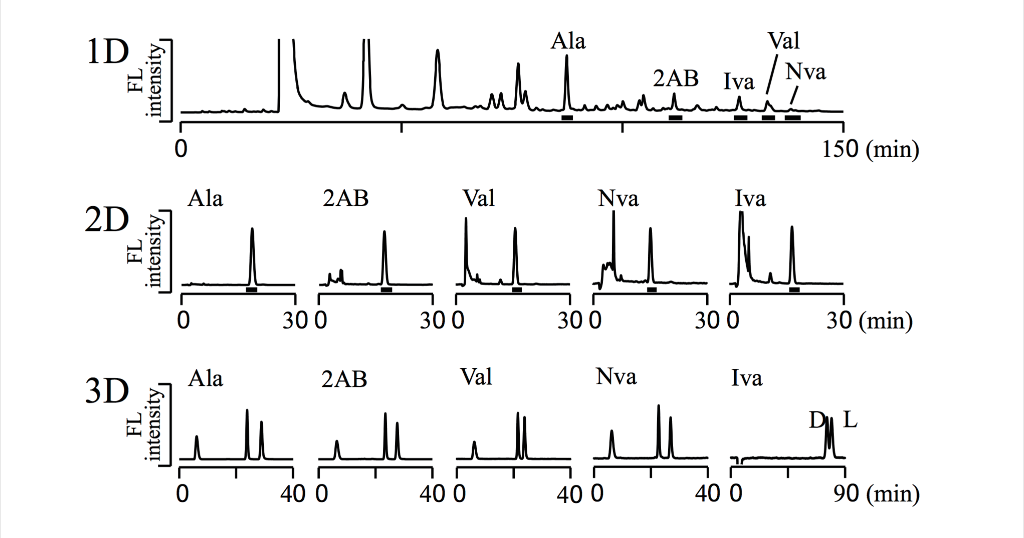

Fig. 3 Three-dimensional HPLC determination of amino acids in the Yamato 002540 meteorite.

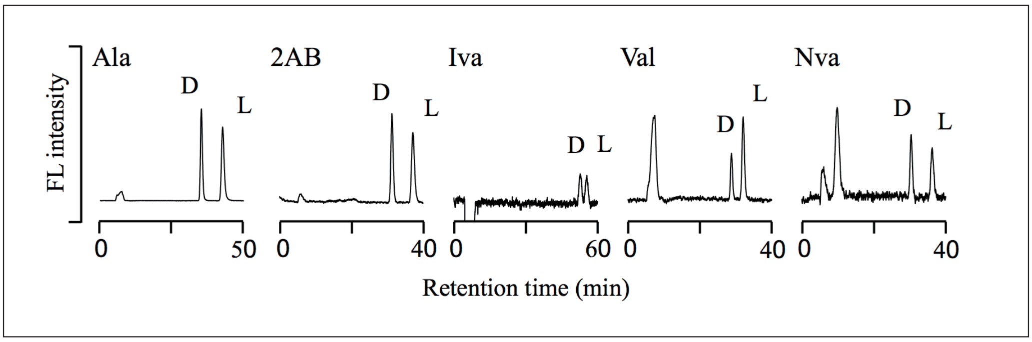

Fig. 4 Determination of amino acid enantiomers in the asteroid Ryugu.

4. Conclusions

In this work we presented a three-dimensional HPLC technique capable of accurately measuring chiral amino acids in extraterrestrial samples, and the method was applied to analyze the samples collected from the Yamato meteorite and from the asteroid Ryugu. The combination of multiple separation modes allows to achieve extremely high selectivity, and making the three-dimensional HPLC system a powerful tool for analyzing extraterrestrial samples and other complex real-world specimens.

The results obtained for both extraterrestrial samples clearly demonstrate the existence of amino acids in cosmic space. Our findings that such amino acids exist in almost racemic mixtures—with D- and L-forms in roughly 50/50 proportion—suggest that further studies will be needed to clarify the origins of the homochirality observed for amino acids on Earth.

References

C. Ishii, A. Furusho, C.-L. Hsieh, K. Hamase, Multi-dimensional high-performance liquid chromatographic determination of chiral amino acids and related compounds in real world samples, *Chromatography*, **41**, 1-17 (2020).

C. Ishii, K. Hamase, Two-dimensional LC-MS/MS and three-dimensional LC analysis of chiral amino acids and related compounds in real-world matrices, *Journal of Pharmaceutical and Biomedical Analysis*, **235**, 115627 (2023).

A. Furusho, T. Akita, M. Mita, H. Naraoka, K. Hamase, Three-dimensional high-performance liquid chromatographic analysis of chiral amino acids in carbonaceous chondrites, *Journal of Chromatography A*, **1625**, 461255 (2020).

H. Naraoka, K. Hamase, A. Furusho *et al.*, Soluble organic molecules in samples of the carbonaceous asteroid (162173) Ryugu, *Science*, **379**, eabn9033 (2023).

SCIENTIFIC INSTRUMENT NEWS
2024 Vol.21 MARCH
Technical magazine of Electron Microscope and Analytical Instruments.
Article
2024 Vol.21

On-Site Non-Destructive Analysis of Colorants in Cultural Properties

Susumu Shimoyama
PhD[*1]
Color Materials Science Laboratory, Den Material Company Ltd.
Professor Emeritus, Kibi International University

Table of Contents

Cultural properties are precious assets that furnish living, breathing witness to history and heritage. For this reason, scientific studies of cultural properties must rely exclusively on non-destructive analytical techniques, avoiding any chemical or physical processing steps that may risk damaging precious artifacts. In this article we focus in particular on the *colorants* used in cultural properties such as Ryukyuan *bingata* garments, lacquerware, ceramic pottery, *Nihonga* paintings, oil paintings, and *ukiyo-e* woodblock prints. We describe an experimental technique—including both analytical instruments for on-site measurements and methods for processing the information they provide—for analyzing such colorants non-destructively. This technique, which has been used extensively for practical field work, involves a multi-stage procedure for non-destructive analysis of colorants in cultural properties. We begin by taking infrared photographs to determine the infrared absorption properties of the colorants. Then we select points at which to make measurements and capture microscopy images at these points to yield enlarged views of the coloration states. Next, we obtain visible/near-infrared reflection spectra at different measurement points and use the shape of these spectra to analyze the colorants. Finally, we measure X-ray fluorescence (XRF) spectra and attempt to use the resulting elemental analysis data to identify pigments; when pigments cannot be identified in this way, we measure three-dimensional fluorescence (3DF) spectra and use the results to identify dyes.

[*1] Professor Emeritus, Kibi International University and Director, Den Material Company Ltd. Color Materials Science Laboratory, (3-4-19 Kadotabunkamachi, Naka-Ku, Okayama City, Okayama 703-8273 Japan). PhD in Science and Engineering, Iwaki Meisei University Graduate School of Science and Engineering, Department of Science and Engineering. Author of "Research on Non-destructive Methods for Identifying Dyes Used in Ancient Dyed Fabrics and Ukiyo-e Prints from 3D Fluorescence Spectra" (1998).

1. Infrared Photographs

1-1. Instruments

Our infrared photography setup is shown in Figure 1. We use a PENTAX 645D IR camera (effective pixel count: approximately 40 million pixels) equipped with an smcPENTAX-FA645 75 mm F2.8 lens. As light sources we use two Canon SPEEDLITE 420EX flash units with stroboscopic capabilities. On both the front surface of the camera lens and the light-emitting surfaces of the flash units we install IR-86 filters (a sharp-cutoff filter from Fuji Film that transmits infrared wavelengths of 860 nm or longer). We use a wireless remote-flash controller (NEEWER), triggered by the camera with receivers on both flash units, to synchronize the flash units with the shutter. This setup allows us to capture clear images with no need to operate in darkened surroundings: The flash units irradiate the sample surface with infrared light at wavelengths longer than 860 nm, and light reflected from the sample is received by the camera and recorded to yield digital images. Note that we removed the band-pass filter that is usually installed inside the camera to eliminate ultraviolet and infrared wavelengths and transmit only visible light.

Fig. 1 Setup for infrared photography.

Table 1 Behavior of colorants (pigments, metals, and dyes) in infrared photographs.

Pigment (alternative name) or metal		Appearance in infrared photographs
White	Chalk	□ White
	White lead (silver white)	□ White
	Chinese white (zinc white)	□ White
Red	Vermilion	□ White
	Red lead (minium)	□ White
	Bengala (red ochre)	▨ Grey
Yellow	Orpiment	□ White
	Chrome yellow	□ White
	Yellow ochre	▨ Grey
Green	Malachite	■ Black
	Viridian	□ White
	Emerald green	■ Black
Blue	Prussian blue	■ Black
	Azurite	■ Black
	Smalt	▨ Grey
Black	Sumi (carbon black)	■ Black
Metals	Gold	□ White (surface reflections)
	Brass (copper/zinc alloy)	
	Silver	
	Tin	
Dye (coloring matter)		Appearance in infrared photographs
Red	Safflower (carthamin)	□ White
	Lac (laccaic acid)	
	Japan madder (pseudo-purpurin)	
	Sappanwood (brazilin)	
Yellow	Gardenia (crocin)	□ White
	Turmeric (curcumin)	
	Amur cork (berberine)	
	Gamboge yellow (gambogic acid)	
Blue	Indigo	□ White
Purple	Purple gromwell (shikonin)	□ White
Black	Tannin black	▨ Grey - ■ black

1-2. Information derived from infrared photography[1)]

The longer wavelengths of infrared light compared to visible light ensure that infrared light is not reflected from the surfaces of material bodies—as is visible light—but instead penetrates into the body interior. For example, if the colorants in a *bingata* garment transmit infrared light without absorption, the light penetrates to deeper layers of the garment before eventually being reflected from the surface of fibers such as silk, cotton, or hemp; note that the reflected light passes through the colorant a second time as it exits the garment. Thus, when a colorant with high infrared transmittance is irradiated with infrared light for a photograph, the light is reflected at fiber surfaces and passes through the colorant a second time as it exits the sample to be captured and recorded by the camera, yielding white regions in captured images. In contrast, if the sample contains colorants that strongly *absorb* infrared radiation, incident infrared light is absorbed by the colorants before it can penetrate deeper into the material; in this case the light does not reach the fiber surfaces and is thus not reflected back toward the camera, yielding dark regions in captured images. Intermediate between these extremes are colorants with moderate infrared transmittance; in this case, only the transmitted portion of the incident radiation proceeds deeper into the sample to be reflected at fiber surfaces, yielding a lower-intensity reflected signal that produces grey regions in infrared photographs. Also, beneath high-transmittance colorants there may exist written characters or line drawings marked in *sumi ink* (or charcoal); although these are not visible by eye, they appear as dark regions in infrared photographs. In *bingata* garments and similar samples, ultra-fine ink lines drawn by hand on infrared-transmitting colorants appear as dark lines in infrared photographs. This is due to the fact that the ink used, which consists primarily of carbon, exhibits high infrared absorbance. Colorants (pigments, metals, and dyes) appearing as white, black, or grey regions of infrared photographs are listed in Table 1.

Analyzing infrared photographs of model oil painting

When sketches beneath oil paintings are drawn in charcoal (carbon), it is well known that these sketches may be seen in infrared photographs. In fact, this phenomenon is not limited to charcoal, but also applies to infrared-absorbing Prussian blue, as we confirmed by using a HORIBA XGT (X-ray Guide Tube)-5000 X-ray analytical microscope to carry out an elemental-mapping analysis of "Daubigny's Garden"—one of the best-known oil paintings of van Gogh's final years, held by the Hiroshima Museum of Art (dimensions: 530 mm tall × 1030 mm wide)—to determine whether or not a black cat, said to be drawn by van Gogh himself, was present behind the grass (that is, underneath the paint used to depict the grass) in the lower-left portion of the painting (Figure 2)[2,3]. To this day, the black cat remains hidden by brush strokes added by an unknown third party.

In this case, we cannot conduct experiments on the actual cultural property itself. Thus, when a preliminary investigation is required we perform experiments on models that we fabricate ourselves. For the analysis of Figure 2, we used a model of van Gogh's painting to test whether or not our elemental-mapping analysis could successfully identify a black cat hidden beneath the paint layers. This model was constructed by painter Hiroshi Yoshida, who prepared a facsimile—using the same paints van Gogh is thought to have used—of the region of the painting believed to be hiding the black-cat drawing. Yoshida began by blending Prussian blue with chrome yellow to yield "chrome green," then added more Prussian blue to yield a dark blue—nearly black—hue with which he painted a black cat (Figure 3A). Next, using colors thought to be used by van Gogh—primarily zinc white with some silver white, and with chrome yellow as a yellow hue and viridian and emerald green as green hues—Yoshida painted over the black cat to replicate the appearance of the grass in the van Gogh original, superposing multiple grains of grassy textures on top of each other until the black cat was hidden (Figure 3B). Finally, on top of this Yoshida added additional strokes of red ochre—as the unknown third party is believed to have used—to complete the preparation of our model painting[4].

Figure 3C shows an infrared photograph of the model painting. Two of the paints used to prepare the facsimile—Prussian blue and emerald green—are infrared-absorbing and thus appear as black regions in the photograph. Of the other paints, zinc white, silver white, chrome yellow, and viridian appear as white regions, while red ochre appears as grey. Although infrared-absorbing emerald green is present at points scattered throughout the grass in the painting, the black cat appears to be drawn primarily in Prussian blue. This is why the cat is visible in the infrared photograph despite being hidden beneath paint layers depicting the grass. This demonstrates the ability of infrared photography to reveal features drawn in charcoal or other infrared-absorbing substances hidden beneath paint layers.

Unfortunately, our infrared photographs of the original "Daubigny's Garden" did *not* reveal a black cat; we attribute this to the thickness of the paint layers being greater than we had anticipated. However, an elemental-mapping analysis based on scanning X-ray fluorescence (XRF) measurements—performed on-site (in a temporary laboratory set up at the museum) using an X-ray analytical microscope (Figure 4)—revealed, in the mapping image for elemental chrome, drawings outlining the head, neck, front paws, torso, and tail of a cat, thus confirming that van Gogh did in fact draw a black cat beneath his masterpiece.

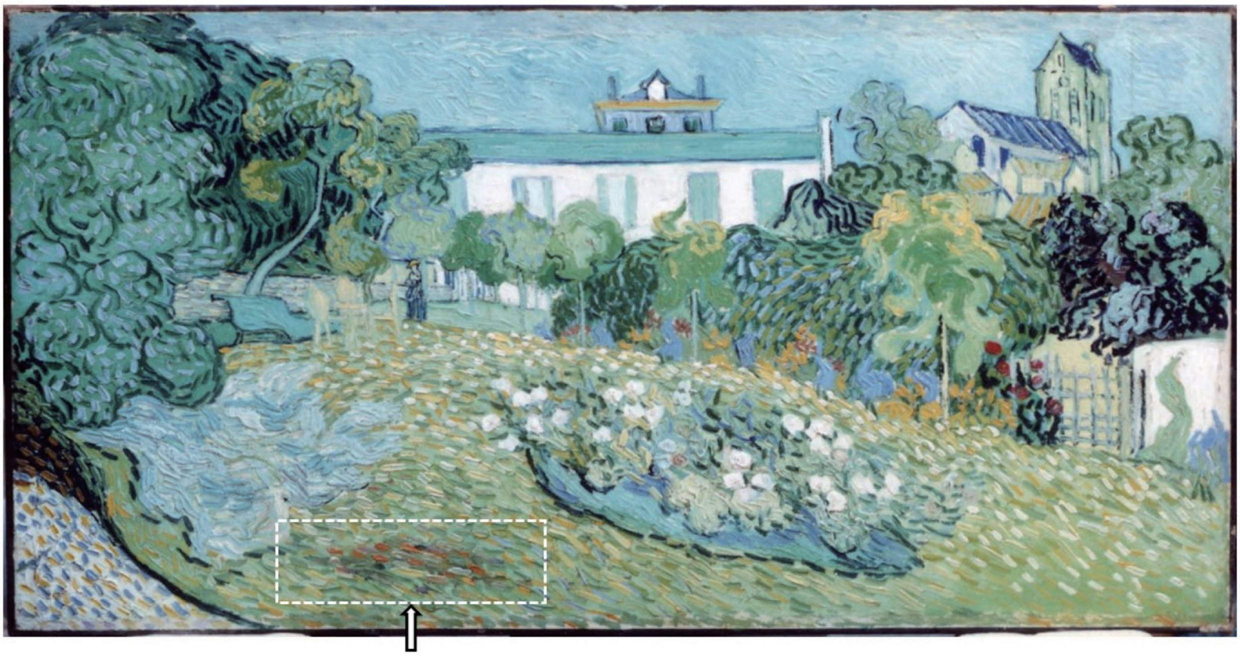

Region analyzed via elemental mapping

Fig. 2 Location of black cat hidden beneath van Gogh's "Daubigny's Garden".

A. The black cat and the surrounding grass are painted first.

B. Additional brushstrokes are then added until the black cat is hidden, completing the model painting.

C: An infrared photograph of the model painting (B) clearly reveals the black cat.

Fig. 3 Model painting prepared to reproduce portion of "Daubigny's Garden" (A, B) and infrared photograph of this model painting (C).

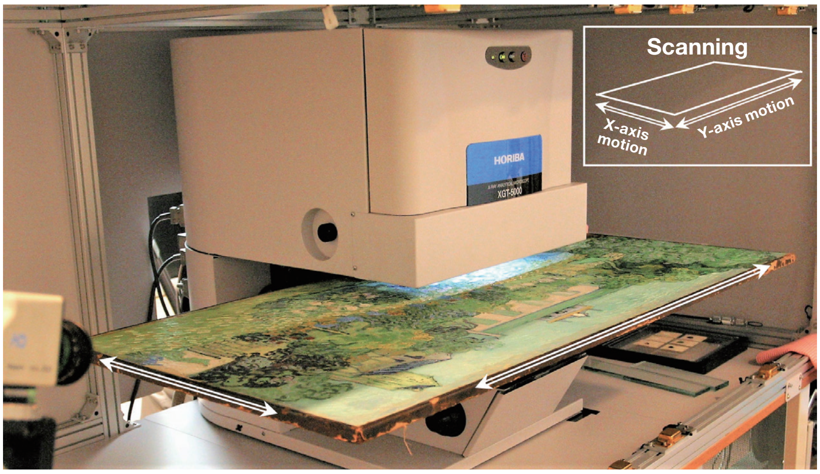

※The sample stage is translated horizontally while measuring X-ray fluorescence emissions induced by X-ray beam 100 μm irradiation.

Fig. 4 Original "Daubigny's Garden" mounted in X-ray analytical microscope for scanning X-ray fluorescence measurements.

Analyzing infrared photographs of bingata garments

Figure 5 shows standard and infrared photographs of a *bingata garment**2. With the exception of the black tannin-based mordant used as a black dye, most of the dyes, metals, and pigments used in this garment—including the *chalk* (Oyster Shell White) and *white lead* used as white pigments, *vermilion* and *red lead* used as red pigments, and *orpiment* used as a yellow pigment—are infrared-transmitting and appear as white regions in the infrared photograph. The garment also contains some colorants that are infrared-absorbing and appear as black regions in the infrared photograph—including *malachite* and *emerald green* for green coloring, *Prussian blue* and *azurite* for blue coloring, and *sumi* ink for black coloring—as well as some colorants that are partially infrared-absorbing and appear as grey regions in the infrared photograph, including *Bengala*, which contains iron oxide, for red coloring, *yellow ochre* for yellow coloring, and *smalt* (smalt mineral glass) for blue coloring. This demonstrates how white, black, and grey features in infrared photographs can be used to narrow down the list of candidates for the colorants that may be present in a specimen. This information, in combination with information obtained by other non-destructive analytical methods, can often be used to identify these colorants precisely.

For example, comparing the color photograph on the left with the infrared photograph on the right in Figure 5, we see that the base yellow color of the garment corresponds to white regions in the infrared image, while the blue and green tail feathers of the Chinese phoenix correspond to black regions. From this we infer, first, that the yellow base color of the garment is due either to *orpiment* (As_2S_3) or to *yellow dye*, as these two colorants appear white in infrared photographs. If XRF spectral measurements, discussed below, detect the presence of arsenic (As), we conclude the garment contains orpiment. On the other hand, if the XRF spectra do not suffice to settle the question, we measure 3DF spectra and identify the dyes present from the unique fluorescence fingerprints of their molecular structures.

Next, because the blue portions of tail feathers in the garment appear as black regions in the infrared photograph, we infer that the blue colorant is either *Prussian blue* ($KFe[Fe(CN)_6]_3 \cdot nH_2O$) or *azurite* ($Cu_3(CO_3)_2(OH)_2$). If XRF spectral measurements detect iron (Fe), we conclude that it is the former; if XRF measurements detect copper (Cu), we conclude that it is the latter.

Finally, because the green portions of tail feathers in the garment appear as black regions in the infrared photograph, we hypothesize that the green colorant is *malachite* (basic copper carbonate $CuCO_3 \cdot Cu(OH)_2$). This will be confirmed if a subsequent XRF detects the presence of Cu.

Actually, at this point we pause to mention one insight gleaned from the many *bingata* specimens we have non-destructively analyzed thus far: in general, *azurite* and *malachite* are never used to yield color features in *bingata* garments. The reason for this is that, when a brush is used to apply a pigment to fabric (fibers), large pigment particles fail to become thoroughly embedded among the cloth fibers, and the fabric does not retain the intended color. Thus, the colorants used to brush patterns onto *bingata* garments must be pigments containing *fine* particles and yielding vivid colors. However, although both *azurite* and *malachite* produce deep and vivid colors when used as *large* particles, when used as *small* particles they yield only mild "whitish" colors typically known as "whitish-blue" and "whitish-green." Consequently, green features in *bingata* garments are typically produced by combining *Prussian blue*—which yields a vivid blue color even as small particles—with *orpiment*, which yields a vivid yellow color. In the case of Figure 5, the presence of Prussian blue in green regions causes these regions to appear black in infrared photographs. This is confirmed by the XRF spectral measurements discussed below, in which green regions of garments are found to contain both Fe (in Prussian blue) and As (contained in orpiment), but *not* Cu (in azurite and malachite).

---

*2 Decorative patterns are added to *Bingata* garments by cutting out a piece of paper in the shape of, e.g., a peony, an iris, or a bird, placing this paper atop the garment, using an applicator tool known as a hera to apply a paste, and allowing the paste to dry. Then, a hake (or pressing brush) is used to press colorant into remaining regions of the pattern in which paste was not applied, after which colorant is painted over the region or a color shading is applied. This is known as hueing. After this step, the paste is rinsed away with water. Paste is then applied to the pattern subjected to hueing to hide it, and it is dried. Finally, the hake is used to apply the base color to fabric regions to which no paste was applied.

Fig. 5 Standard color photograph (left) and infrared photograph (right) of *bingata* garment.

2. Microscopy Images

2-1. Instruments

To capture microscopy images, we use a PENTAX WG-3 camera (lens focal length: 4.5-18.0 mm, aperture range F2.0(W) - F4.9(T), effective pixel count: approximately 16 million pixels) equipped with a micro-stand ring. As shown in Figure 6, for microscopy images of *bingata* garments we place a protective sheet—from which is cut out a circular hole the size of the camera lens—on the garment specimen, then place the camera on this sheet with its lens aligned in the hole. (The weight of the camera, including batteries and SD card, is 247 grams). Then, referring to the camera monitor, we move the camera until the image is centered on one of the predetermined measurement points, set the optical magnification to digital microscopy mode and capture images via remote control. The available optical magnifications are 1.2×, 2.5×, and a maximum of 4.0×, and the image data captured for each magnification can be viewed on a PC.

Fig. 6 Setup for capturing microscopy images.

2-2. Information derived from microscopy images

Microscopy images of *bingata* garments present enlarged views of the colorants used for the base color and for accent colors in the fiber structures selected as measurement points. If these colorants are *dyes*, then the images allow us to observe transparent dyes for chromatic colors penetrating into the interior of fibers to achieve coloration, and also to observe the structural composition of the fabric. On the other hand, if the colorants are *pigments*, then we observe non-transparent colorants affixed to the surfaces of fibers; in this case, there will be defect regions, through which the base fibers will appear as white regions in microscopy images. For example, Figure 7 shows a microscopy image (optical magnification 4.0×) of red flower petals within a peony pattern formed on a *bingata* specimen. The image reveals non-transparent red colorants affixed to fiber surfaces; small defect regions, in which the colorants have peeled away or detached, appear white. From this we conclude that flower petals in the peony pattern were formed using a red pigment. Note that these red areas will appear as white regions in infrared photographs; visible/near-infrared reflection spectra, discussed below, reveal spectral shapes similar to that for *vermilion* in Figure 9A, while XRF spectra, also discussed below, indicate the presence of mercury (Hg). From these findings we conclude that the red coloration seen in the microscopy image on Figure 7 is due to particles of the pigment *vermilion* (HgS) affixed to fabric fibers.

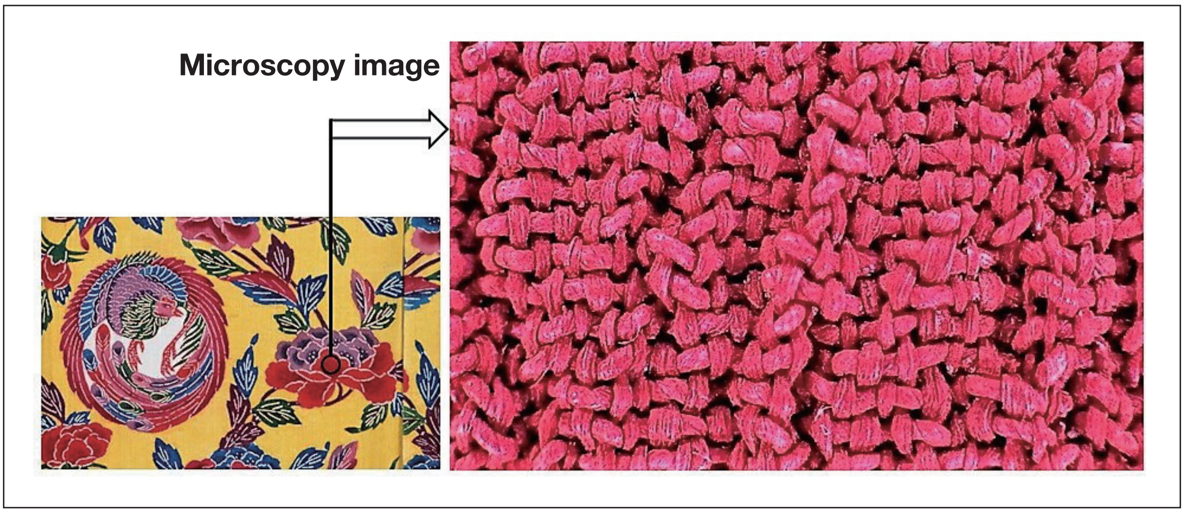

Fig. 7 Microscopy image of red flower petals in peony pattern formed on *bingata* garment.

3. Visible/Near-infrared Reflection Spectra

3-1. Instruments[6)]

Our setup for measuring visible/near-infrared reflection spectra is shown in Figure 8. We use a two-branch fiber-optic cable, (R400-7-VIS-NIR, Ocean Optics USA), connected at one end to a light source (LS-1 tungsten halogen lamp, Ocean Optics USA) and at the other end to a miniature multichannel spectrometer (USB4000, Ocean Optics USA). For example, to measure visible/near-infrared reflection spectra for a *bingata* specimen, we place a protective sheet—from which is cut out a circular hole—on top of the specimen, positioned with its hole centered on a preselected measurement point, and then place a light-blocking box (390 g), into which is inserted the end of the optical fiber, on top of the sheet. Next, we look through the view portal of the light-blocking box and make fine adjustments to ensure that light from the optical fiber is irradiating the vicinity of the preselected measurement point; we maintain a distance of approximately 3 mm from the end of the cable to the specimen surface, yielding a spot diameter of 1 mm irradiated by light with wavelengths ranging from the visible to the near-infrared region (380-1000 nm). Light reflected from the specimen is then carried by the other branch of the optical fiber to the spectrometer, where it is subdivided by wavelength to yield a visible/near-infrared reflection spectrum—that is, a curve plotting spectral reflectance vs. wavelength from the visible to the near-infrared region—which is displayed on a PC. Note that this setup can also be used without the light-blocking box: with the optical-fiber tip positioned approximately 3 mm from the preselected measurement point, reflected light is immediately captured and indicated on the PC display, allowing non-destructive measurement of visible/near-infrared reflection spectra. We have used this approach to measure large numbers of woodblock prints in a short period of time, as discussed below in the section *Identifying blue colorants used in ukiyo-e woodblock prints*.

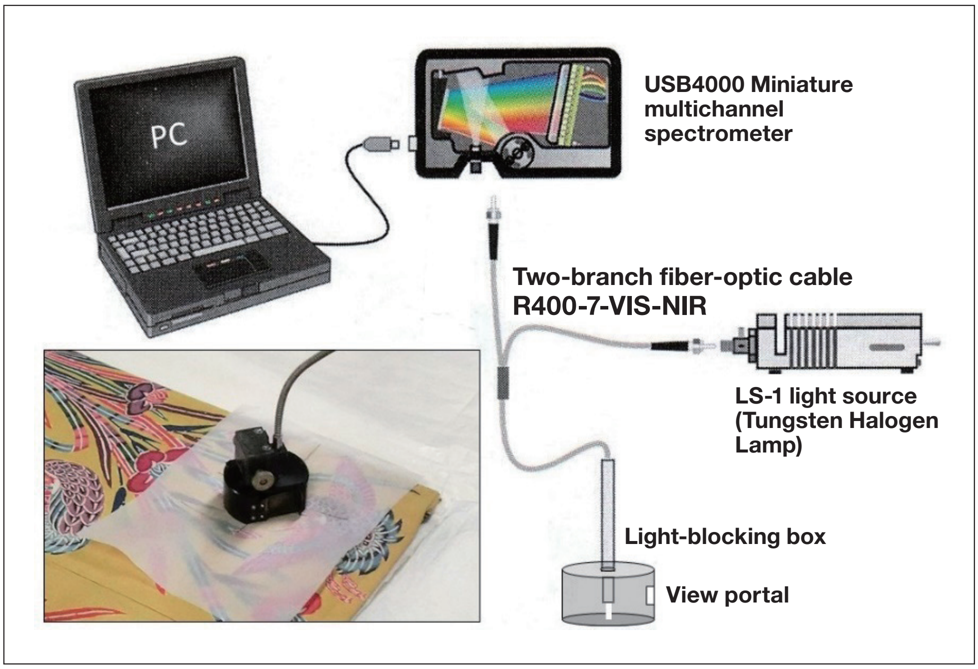

Fig. 8 Setup for measuring visible/near-infrared reflection spectra.

3-2. Information derived from visible/near-infrared reflection spectra

The visible/near-infrared reflection spectrum of a body plots the reflectance of the body (in units of percent) on the vertical axis vs. wavelength (in units of nanometers) on the horizontal axis. This yields a curve indicating how the body's reflectance varies with wavelength over the visible (380-700 nm) and near-infrared (700-1000 nm) regions. The visible-light portion of this curve contains information on the hue, brightness, and color intensity of colorants in the specimen, while the full curve spanning the visible and near-infrared regions contains information on the physical properties of the specimen. It is often possible to distinguish distinct colorants from the unique shapes of their spectra over this broad wavelength range, even if the colorant substances appear to be identical in color when viewed with the naked eye. Visible/near-infrared reflection spectra for some common colorants are shown in Figures 9-11.

Looking first at the spectrum of the pigment *vermilion* in Figure 9A, we see that the reflectance is low for short wavelengths, but begins to rise rapidly around 600 nm—a visible wavelength that the human eye recognizes as *red*—and remains high as the wavelength increases into the near-infrared region. Similarly, in the spectra of the iron-oxide-based pigments *Bengala* and *yellow ochre* in Figure 9B, we see characteristic absorption features near 655 nm in the visible region, and near 870 nm in the near-infrared region. Next, in the spectrum in Figure 10C for the pigment *smalt* we see a characteristic peak indicating a slight increase in reflectance near 565 nm in the visible region. In the spectrum in Figure 11B for the dye *lac* we see the reflectance increase rapidly near the 600 nm wavelength of *red*; and although this behavior is similar to that seen in the spectrum of the pigment *vermilion* (Figure 9A), the spectrum in Figure 11B is distinguished by a characteristic peak indicating a slight increase in reflectance near 545 nm in the visible region. Finally, in the spectrum in Figure 11C for the dye *indigo*, we see a characteristic spectral shape including a reflectance peak near the visible wavelength of 420 nm—interpreted by the human eye as *blue*—and a rapid increase in reflectance as we enter the near-infrared region beyond 700 nm. As these examples demonstrate, many varieties of colorants—including the red pigment *Bengala*, the yellow pigment *yellow ochre*, the blue pigment *smalt*, and the red dye *lac*—can be identified from the characteristic shapes of their reflection spectra.

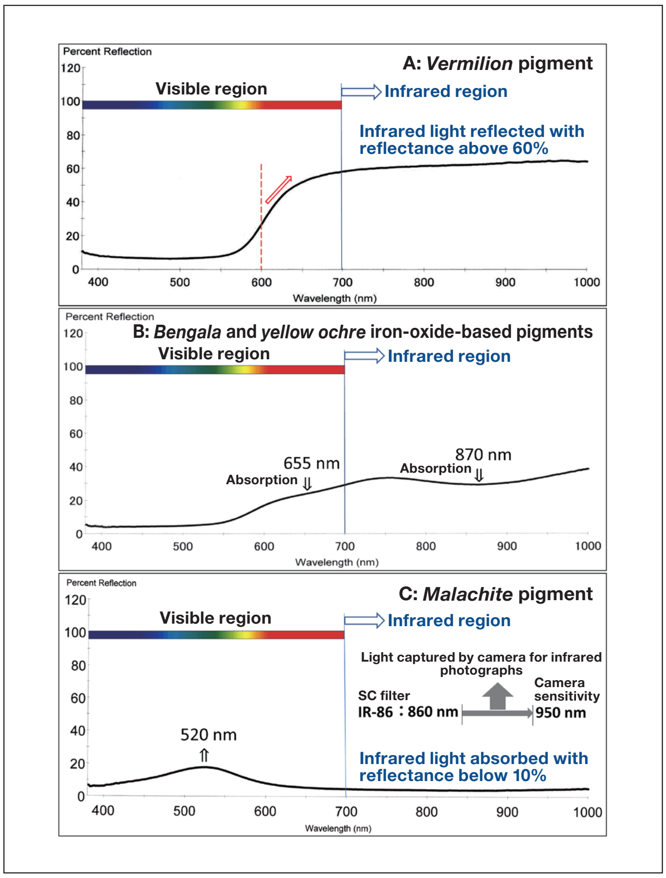

Fig. 9 Visible/near-infrared reflection spectra of *vermilion* (A), iron-oxide-based pigments *Bengala* and *yellow ochre* (B), and *malachite* (C).

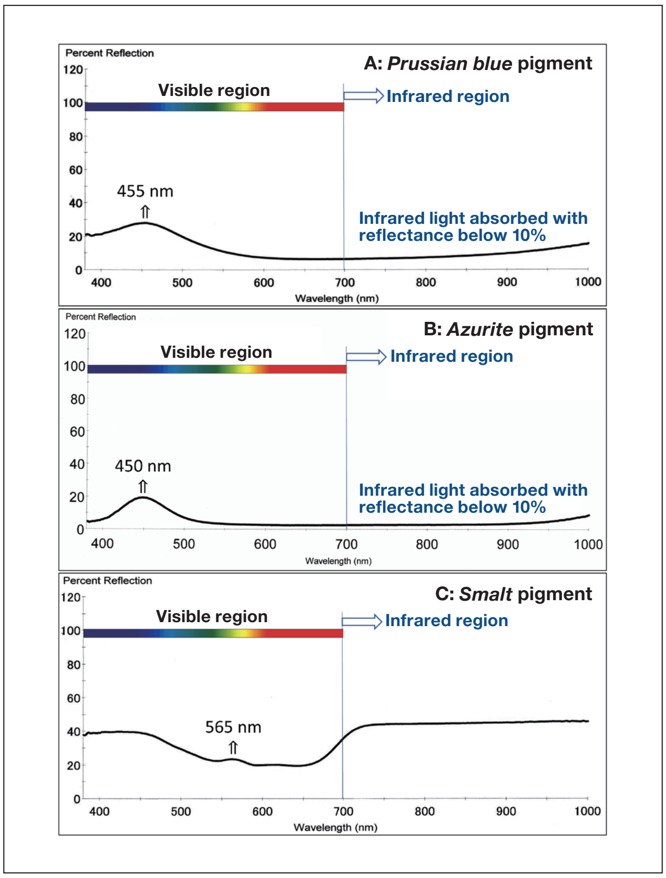

Fig. 10 Visible/near-infrared reflection spectra of *Prussian blue* (A), *azurite* (B), and *smalt* (C).

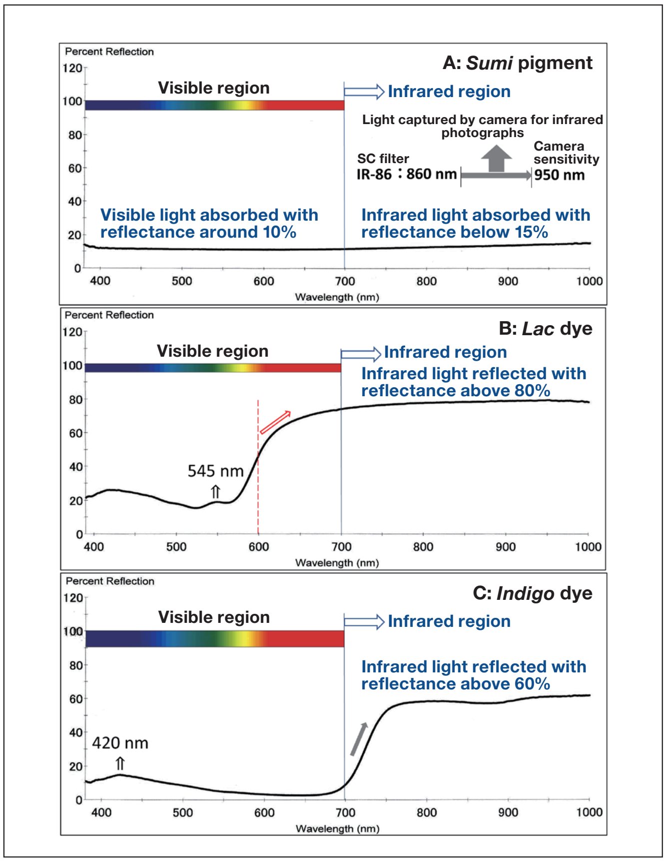

Fig. 11 Visible/near-infrared reflection spectra for *sumi* ink (A), *lac* (B), and *indigo* (C).

Identifying blue colorants used in ukiyo-e woodblock prints

The *ukiyo-e* woodblock prints produced during Japan's Edo period used a variety of substances to achieve blue coloration. *Commelinin* was the blue pigment of choice throughout the Meiwa and Kansei periods (1765-1800), but the years between the late Kansei period and the end of the Bunka period (1817) witnessed the discovery of *indigo*, which became increasingly popular after the start of the Bunsei period in 1818 and was the most common choice by the mid-Bunsei era, around the year 1824. The transition from *indigo* to *Prussian blue* began in 1830, the first year of the Tenpo era, and proceeded rapidly: by Tenpo 2 (1831) Prussian blue was used in fully 86% of all *ukiyo-e* prints, and by Tenpo 3 (1832) the figure was nearly 100%6,7). To investigate this historical evolution in the blue colorants of *ukiyo-e* prints, we analyzed a large set of *ukiyo-e* specimens, focusing in particular on *shibai-e* and *yakusha-e* prints[*3] made to promote *kabuki* dramas and actors. Where necessary, we combined visible/near-infrared reflection spectra with other types of analyses discussed below—including XRF spectra to assist in identifying *Prussian blue* and 3DF spectra to assist in identifying *indigo*—but in many cases we found that visible/near-infrared reflection spectra—which are quick and easy to measure in our non-destructive setup—*alone* sufficed to distinguish *commelinin*, *indigo*, and *Prussian blue*. This is illustrated by the visible/near-infrared reflection spectrum of *commelinin* shown in Figure 12, which we readily observe to differ sufficiently from both the *Prussian blue* spectrum in Figure 10A and the *indigo* spectrum in Figure 11C to allow rapid identification of the blue colorant used in a given *ukiyo-e* specimen from the shape of measured reflection spectra.

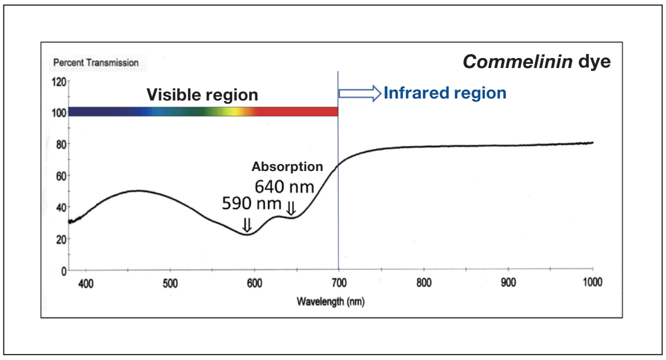

Fig. 12 Visible/near-infrared reflection spectrum of *commelinin*.

Emergence of landscape images as subgenre of ukiyo-e prints

In addition to the insights described above, our use of visible/near-infrared reflection spectra as a tool for non-destructive analysis also achieves an interesting feat of historical detective work: We have established that Katsushika Hokusai's famous woodblock-print series "Thirty-Six Views of Mount Fuji," published around the first year of the Tenpo era, marks the first appearance of landscape images as a particular subgenre of *ukiyo-e* prints. As shown in Figure 13, each of the 36 prints in this series, labeled "Front views of Mount Fuji", makes use of both dark and light shades of blue to depict the sky and the sea in ways that lend the viewer a sense of closeness—or of distance. This is achieved via the method of *bokash*i printing8), and by measuring visible/near-infrared reflection spectra for the sky and sea regions of each of the 36 prints we have confirmed that the spectrum of *Prussian blue* ($KFe[Fe(CN)_6]_3 \cdot nH_2O$), shown in Figure 10A, is present in all cases, while XRF spectral measurements, discussed below, confirm the presence of iron Fe5). The attractive *bokashi* appearance evoked by this genre of landscape images is impossible to achieve without the ultra-miniature particles and bright blue coloration of *Prussian blue*, and thus we may say that the use of *Prussian blue* was a key enabling factor allowing the genre of landscape images to be introduced into the world of *ukiyo-e* woodblocks.

In the production process for *ukiyo-e* prints, the first step was to use a printing block known as a "key-block" (*omohan*9)) to print the title of the work and the signature of the illustrator, as well as pictures consisting of line drawings, and a sequence of "color-blocks" (*irohan*)—sculpted separately for each color in the image—was applied, each superposed on top of the last, to yield multicolored prints. In typical *ukiyo-e* processes, the *omohan* was used with *sumi* ink, but the

---

[*3] *Shibai-e* and *yakusha-e* were the most frequently published types of *ukiyo-e* prints. These prints were rarely modified or reprinted after their initial publication, and the year of their publication can be determined from *kabuki* records or other historical resources. Indeed, as *kabuki* performances in this era occurred at two-*month* intervals, it is even possible to pinpoint the month of publication. As these prints were published as advertisements announcing upcoming performances, their production predates those performances.

"Thirty-Six Views" deviated from this pattern by using an *omohan* with blue *indigo*. Consequently, our measurements of visible/near-infrared reflection spectra for the title and signature regions and the outlines in the *Thirty-Six Views* series exhibit the characteristic shape of the *indigo* spectrum (Figure 11C)[6].

Fig. 13 Katsushika Hokusai's "Thirty-Six Views of Mount Fuji (Front Views of Mount Fuji)".

Relationship between visible/near-infrared reflection spectra and infrared photographs

In regions of specimens containing pigments with high infrared transmittance, line-drawing sketches and other features that lie beneath surface layers are easily detected in infrared photographs[1]. To this end, the *reflectance* values plotted in the visible/near-infrared reflection spectrum of a colorant may simply be reinterpreted in terms of *transmittance* values[*4]. This observation allows us to understand how a colorant appears in infrared photographs—specifically, the extent to which the colorant produces white regions or black regions in infrared photographs—based on reflectance data measured for the colorant in the near-infrared region. For example, if the *reflectance* of a colorant exceeds 60% in the infrared region, we may infer that the colorant will also exhibit high *transmittance* above 60%; consequently, most infrared radiation will pass through the colorant into the specimen, reflect from fiber surfaces or other features lying deeper within the specimen, then pass through the colorant a second time as it travels back out of the specimen to be captured by the camera, producing white regions in infrared photographs. In contrast, a colorant whose infrared *reflectance* is below 20% will also exhibit low *transmittance* below 20%; when capturing infrared photographs, such colorants will absorb most of the incident infrared light before it can travel deeper into the specimen and be reflected from fiber surfaces, and the absence of reflected light captured by the camera will produce black regions in infrared photographs. For intermediate colorants with near-infrared reflectance values around 40%, incident infrared radiation will be partially absorbed and partially transmitted; the transmitted portion will be reflected from fiber

---

[*4] The software package we use to measure visible/near-infrared reflection spectra, from Ocean Optics USA, uses the same formulas to determine reflectance and transmittance. This allows us to interpret *reflectance* and *transmittance* interchangeably.

surfaces or other features beneath the colorants and will travel back out of the material—passing through the colorant a second time—to be captured by the camera, but the relatively low intensity of this reflected light will produce grey regions in infrared photographs.

Applying these observations to the colorants considered above, *vermilion* (Figure 9A), *lac* (Figure 11B), and *indigo* (Figure 11C) all exhibit a near-infrared reflectance of more than 60%, and thus appear as white regions in infrared photographs. In contrast, *malachite* (Figure 9C), *Prussian blue* (Figure 10A), *azurite* (Figure 10B), and *sumi* ink (Figure 11A) all exhibit a near-infrared reflectance of less than 20%, and thus appear as black regions in infrared photographs. Finally, the iron-oxide-based pigments *Bengala* and *yellow ochre* (Figure 9B), together with *smalt* (Figure 10C), have near-infrared reflectance values around 40%, and thus appear as grey regions in infrared photographs. This indicates how correlations between these two types of data—infrared photographs and visible/near-infrared reflection spectra—may be used to check the accuracy of analytical results.

Using visible/near-infrared reflection spectra to confirm the use of lac as a red colorant in bingata garments

One of the dyes commonly used in *bingata* garments is the red colorant *lac* (laccaic acid). Figure 14 shows visible/near-infrared reflection spectra measured for red flower-petal regions in an iris pattern on a *bingata* specimen. In this spectrum we see a characteristic peak near 545 nm in the visible region, indicating a slight increase in reflectance, with the reflectance rising for wavelengths longer than 600 nm and remaining high into the near-infrared region. Note that the characteristic reflection peak near 545 nm matches the measured spectrum for *lac* shown in Figure 11B. However, the difference between the maximum and minimum measured reflectance values in Figure 14 is smaller than the corresponding gap in Figure 11B, suggesting that the colors for the specimen in Figure 14 are less intense (less brilliant) than those in the standard specimen[*5] whose principal ingredient was *lac* and whose spectrum is shown in Figure 11B. The reason of this discrepancy is explained below in our discussion of XRF spectral measurements.

The visible/near-infrared reflection spectra that we measured for the red flower petals in the iris pattern also revealed the presence of lead (Pb), indicating that *white lead* ($2PbCO_3 \cdot Pb(OH)_2$) was used as a white colorant together with *lac* as a red colorant. Blending with *white lead* has the effect of increasing the brightness of the *lac* —that is, making it appear whiter—while decreasing the color intensity (brilliance), thus reducing the gap between the maximum and minimum reflectance values in Figure 14. Nonetheless, the appearance in the measured reflection spectra of a weak peak near 545 nm clearly indicates that the substance in question is in fact *lac*. As discussed below, the fluorescence fingerprint for *lac* obtained from 3DF spectra confirm that that red flower-petal regions of the iris pattern contain a blend of *white lead* and *lac* that has the effect of modifying the observed shade of red.

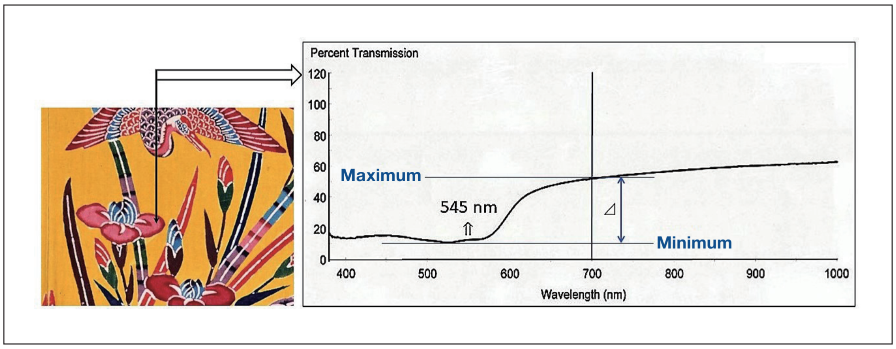

Fig. 14 Visible/near-infrared reflection spectrum measured for *red* region of *bingata* specimen.

[*5] The visible/near-infrared reflection spectrum for lac in Figure 11B was measured for a standard specimen of Edo-era rouge-dyed cotton provided by Kunisuke Ueda of Uematsu Japanese Art Supply (Shibuya, Tokyo, Japan).

4. X-ray Fluorescence Spectra

4-1. Instruments[10)]

Figure 15 shows the setup we use for on-site measurement of XRF spectra. This apparatus does not use a fluorescent X-ray tube as an X-ray source; instead, X-rays are generated by an X-ray-emitting radioactive isotope. More specifically, the X-ray source (made by AET Technologies) consists of pellets of ^{241}Am arranged in a ring and hermetically sealed in a ceramic container, yielding a fully enclosed annular source of X-rays with an activity of 1.85 MBq. To measure XRF spectra, as shown in Figure 15, we position this source (labeled A in the figure) at a distance of approximately 5 mm from a preselected measurement point on a specimen, thus irradiating the specimen with X-rays emitted by ^{241}Am. (These X-rays have energies of 13.95 keV, 17.74 keV, and 59.54 keV.) The source produces a circumferential pattern of X-ray irradiation that induces XRF from elements present within a 12-mm-diameter circular region of the specimen centered on the measurement point. The energies of these fluorescent X-rays are measured by a semiconductor detector (Amptek XR-100CR Si-PIN, Be window 0.3 mil=7.62 μm, energy resolution 180-205 eV, labeled C in Figure 15). The signal from this detector is amplified by a preamp (Amptek PX2T/CR-type, labeled D), separated by a miniature multichannel pulse-height analyzer (Amptek PMCA-8000A, labeled E), and converted into XRF spectral data by a software package installed on a PC (F). Because this is an energy-dispersive apparatus, it is capable of simultaneous multi-element analysis. Shielding material (lead, labeled B) enclosing the upper surface, the perimeter, and the inner cavity region of the X-ray source (A) prevents X-rays emitted by the source from entering the window of the detector (C). The tip of the detector is affixed to the upper surface of the source across the shielding material.

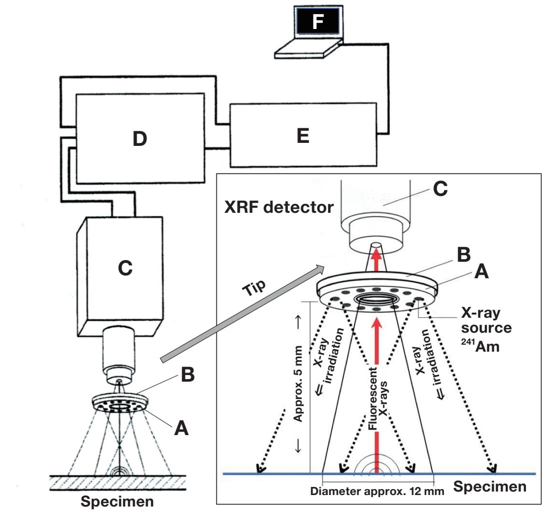

Fig. 15 Setup for X-ray fluorescence measurements.

Fig. 16 Measuring XRF spectra for *bingata* specimen.

Fig. 17 Measuring X-ray fluorescence spectra for cultural property deemed a Japanese national treasure: square-base candle stand with green *Ryoku-Yu* glaze.

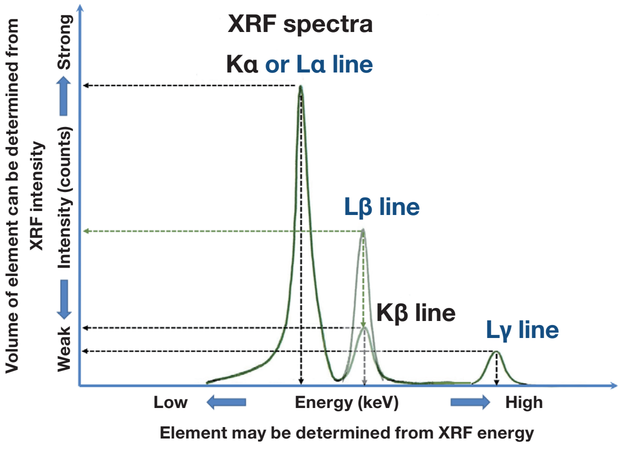

Fig. 18 Conceptual diagram illustrating typical X-ray fluorescence spectra.

To measure XRF spectra of *bingata* specimens using this apparatus, we begin by mounting the X-ray source A / detector C assembly on an adjustable arm designed for use as a stationary camera mount (Figure 16). We use the arm to position the source/detector assembly above the *bingata* specimen at a distance of approximately 5 mm from the preselected measurement point; the assembly will remain in this position throughout the non-contact measurement. The specimen is then irradiated by X-rays emitted from the ^{241}Am source, inducing elements in the vicinity of the preselected measurement point to emit fluorescent X-rays, whose energies are measured by the detector C.

Similarly, to measure XRF spectra for a piece of pottery or similar specimen, we fix the position of the source/detector assembly at a distance of approximately 5 mm from a flat portion of the specimen, as shown in Figure 17; again, X-rays emitted by the ^{241}Am source irradiate the specimen and induce the emission of fluorescent X-rays whose energies are measured by the detector. As the X-ray irradiation time increases, the measured XRF spectra increasingly come to resemble the spectrum shown in the conceptual diagram in Figure 18. The length of time required to obtain accurate spectra for a given element depends on how much of the element is present in the specimen. The larger the volume of the element contained in the specimen, the more rapidly the measured spectral curve will take shape*[6], and thus the shorter the measurement time required to yield clear spectra. Typical measurement times [characterized by *Live Time* (LT), the time required to accumulate an effective number of X-ray counts] depend on the volume of the given element contained in the specimen, but are on the order of 180-600 s (3-10 min) if the element in question is abundant in the specimen, or 1200-1800 s (20-30 min) if the element is scarce in the specimen. For specimens containing particularly low volumes of a given element, the time required to measure clear XRF spectra may exceed 3600 s (1 h). These long measurement times are a consequence of the weak X-ray source in our apparatus: the ^{241}Am source has an activity of just 1.85 MBq. However, this source was purchased through the Japan Radioisotope Association, with certification from AET Technologies USA, in 1999, prior to the 2005 enactment of the "Act on the Regulation of Radioisotopes, etc." that is currently in effect in Japan. Because the activity of the source does not exceed the limit (3.7 MBq) set by the previous regulatory framework, at present the source can be used with no need to notify, or receive permission from, relevant oversight bodies—assuming, of course, that it is used and managed properly. Moreover, because the source is hermetically sealed and has an intensity below 3.7 MBq, there is no need to worry about exceeding the regulated maximum dose of external radioactivity (1.3 mSv over 3 months); consequently, we can use the source for non-destructive on-site analyses at museums and other facilities without needing to establish controlled X-ray areas. Also, although the activity of this source was 1.85 MBq in the year it was constructed (1998), this activity has decreased over the ensuing 25 years. Specifically, based on the 432-year half-life of ^{241}Am, we calculate that the activity of the source has declined by 5.8% since its construction, placing its current activity at 1.74 MBq. We consider this to be more than adequate for use in X-ray fluorescence analysis. However, if we ever purchase a new X-ray source, we will need to receive permission to use it in accordance with current laws and regulations.

4-2. Information derived from XRF spectra

As shown in the conceptual diagram in Figure 18, XRF spectra are obtained by plotting the intensity (counts) on the vertical axis against the energy (keV) on the horizontal axis. These curves describe the energy and intensity of fluorescent X-rays emitted by the constituent elements of the specimen. The XRF *energy* is indicated by the horizontal-axis position of peaks in the spectrum, while the *intensity* is indicated by the peak height.

XRF spectra form doublets and triplets

The X-rays emitted by the ^{241}Am source, which have energies of 13.95 keV, 17.74 keV, and 59.54 keV, induce different types of fluorescent X-ray emissions from different elements. Elements in column 4 of the periodic table—including calcium (Ca), titanium (Ti), chromium (Cr), manganese (Mn), iron (Fe), cobalt (Co), nickel (Ni), copper (Cu), zinc (Zn), and arsenic (As)—emit fluorescent X-rays with the characteristic energy of the Kα line. For column-5 elements such as silver (Ag), cadmium (Cd), and tin (Sn), fluorescent X-ray emissions have the characteristic energy of the Kβ line.

---

*[6] When an X-ray tube is used as an X-ray source, measurement times may be shortened by increasing the tube voltage (kV) to increase the energy of emitted X-rays or by increasing the beam current (μA) to increase the intensity (number) of emitted X-rays, although the details depend on the elemental composition of the measurement specimen.

Meanwhile, column-6 elements—such as barium (Ba), tungsten (W), platinum (Pt), gold (Au), mercury (Hg), and lead (Pb)—emit fluorescent X-rays with the energies of the Lα line, the Lβ line, and the Lγ line. Consequently, fluorescent X-ray emissions from a single element may be organized into groups: the Kα-line and Kβ-line spectra in Figure 18 form a *doublet*, while the Lα-line, Lβ-line, and Lγ-line spectra form a *triplet*. The energies of fluorescent X-ray emissions from a given element are characteristic of that element, and reference manuals for X-ray analysis contain detailed tables listing characteristic Kα-line and Kβ-line energies, or characteristic Lα-line, Lβ-line, and Lγ-line energies, for the various elements of the periodic table, ordered by atomic number[11)]. Using these tables, measured XRF spectra can be compared to tabulated data: if the horizontal-axis position of a peak in a measured spectrum matches the characteristic fluorescent X-ray energy tabulated for a given element, it can be concluded that this element is present in the sample. Table 2 lists the energies of various fluorescent X-ray emissions from the constituent elements of common pigments and metals. If the measured energy of a fluorescent X-ray emission from a specimen (that is, the energy read off from the horizontal-axis position in the XRF spectrum) matches the energy tabulated for a given element, the pigments or metals having that element as a constituent can be identified.

Also, for a specimen irradiated by X-rays of a given intensity, the intensity of fluorescent X-ray emissions from an element is proportional to the volume (number of atoms) of that element contained in the specimen. We can make use of this observation as follows: We prepare standard specimens containing different known concentrations of a particular element, measure the XRF intensity for each of these specimens, then plot the intensity for each specimen versus the concentration of the given element in that specimen. The resulting plot, known as a *calibration curve*, can then be used to quantify the concentration (volume) of the given element in an unknown specimen based on the XRF intensity for that specimen.

Table 2 Energies of fluorescent X-rays emitted by constituent elements of pigments and metals

Color	Name	Constituent element (chemical formula)	Energy of fluorescent X-ray emission from pigment or metal		
			α line	β line	γ line
White	Chalk	$CaCO_3$	Ca Kα 3.691 keV	Ca Kβ 4.013 keV	—
	White lead	$2PbCO_3 \cdot Pb(OH)_2$	Pb Lα 10.550 keV	Pb Lβ 12.612 keV	Pb Lγ 14.764 keV
Red	Vermilion	HgS	Hg Lα 9.987 keV	Hg Lβ 11.821 keV	Hg Lγ 13.830 keV
	Red lead	Pb_3O_4	Pb Lα 10.550 keV	Pb Lβ 12.612 keV	Pb Lγ 14.764 keV
	Bengala	Fe_2O_3	Fe Kα 6.400 keV	Fe Kβ 7.058 keV	—
Yellow	Orpiment	As_2S_3	As Kα 10.532 keV	As Kβ 11.726 keV	—
	Yellow ochre	$Fe_2O_3 \cdot nH_2O$	Fe Kα 6.400 keV	Fe Kβ 7.058 keV	—
Green	Malachite	$CuCO_3 \cdot Cu(OH)_2$	Cu Kα 8.041 keV	Cu Kβ 8.905 keV	—
	Emerald green	$Cu(C_2H_3O_2)_2 \cdot 3Cu(AsO_2)_2$	Cu Kα 8.041 keV	Cu Kβ 8.905 keV	—
			As Kα 10.532 keV	As Kβ 11.726 keV	—
Blue	Prussian blue	$KFe[Fe(CN)_6]_3 \cdot nH_2O$	Fe Kα 6.400 keV	Fe Kβ 7.058 keV	—
	Azurite	$Cu_3(CO_3)_2(OH)_2$	Cu Kα 8.041 keV	Cu Kβ 8.905 keV	—
	Smalt	$[Co,Ni]As_{3-2},Fe+SiO_2,K_2O,CaO$	Fe Kα 6.400 keV	Fe Kβ 7.058 keV	—
			Co Kα 6.925 keV	Co Kβ 7.649 keV	—
			Ni Kα 7.472 keV	Ni Kβ 8.265 keV	—
			As Kα 10.532 keV	As Kβ 11.726 keV	—
Black	Sumi	C	C Kα 0.277 keV	XRF is undetectable	
Gold	Gold (foil/slurry)	Au	Au Lα 9.712 keV	Au Lβ 11.440 keV	Au Lγ 13.382 keV
	Brass (foil/shavings)	Cu:Zn = 70-90:30-10 wt%	Cu Kα 8.041 keV	Cu Kβ 8.905 keV	—
			Zn Kα 8.631 keV	Zn Kβ 9.572 keV	—
Silver white	Silver (foil/slurry)	Ag	Ag Kα 22.105 keV	Ag Kβ 24.942 keV	—
	Tin	Sn	Sn Kα 25.295 keV	Sn Kβ 28.486 keV	—

(Intensity ratio) Kα/Kβ: approximately 10:1; Lα/Lβ: between 10:6 and 10:5; Lβ/Lγ: approximately 10:1

Intensity ratio: The relative intensity of Kα and Kβ lines—and of Lα, Lβ, and Lγ lines

Kα-line and Kβ-line emissions, which form a doublet, differ in intensity by roughly a factor of 10, i.e., the intensity ratio is approximately Kα:Kβ = 10:1. For Lα-line and Lβ-line emissions, which are part of a triplet, the intensity ratio is typically adjusted by varying the voltage of the X-ray tube used to generate X-rays to a value somewhere between Lα:Lβ = 10:10 and Lα:Lβ = 10:5$^{12)}$. However, this procedure is not available in our apparatus, which uses a ^{241}Am source (activity 1.85 MBq) in place of an X-ray tube. Consequently, while the Kα-line/Kβ-line intensity ratio in our experiments assumes its usual value of roughly 10:1, the Lα-line/Lβ-line intensity ratio is roughly 10:6 or 10:5. Also, if Lα-line and Lβ-line emissions are observed, then Lγ-line emissions are also observed, although with low intensity: the Lβ-line/Lγ-line intensity ratio is roughly 10:1.

As an example, Figures 19a and 19b show XRF spectra measured by our apparatus for the green pigment *emerald green* ($Cu(C_2H_3O_2)_2 \cdot 3Cu(AsO_2)_2$) and for the white pigment *white lead* ($2PbCO_3 \cdot Pb(OH)_2$). Because our apparatus is an energy-dispersive fluorescent X-ray analyzer based on a semiconductor detector, it can simultaneously detect fluorescent X-ray emissions from multiple elements. Emerald green contains Cu and As as constituent elements, and both elements emit fluorescent X-rays, whose energies we detect. As shown in Figure 19a, from Cu we obtain spectrum A, corresponding to the 8.04 keV Cu-Kα line, and spectrum B, corresponding to the 8.92 keV Cu-Kβ line. For As we obtain spectrum C, corresponding to the 10.54 keV As-Kα line, and spectrum D, corresponding to the 11.75 keV As-Kβ line. In both cases, the Kα-line/Kβ-line intensity ratios are approximately 10:1. On the other hand, white lead contains Pb as a constituent element; as shown in Figure 19b, we obtain spectrum A, corresponding to the 10.55 keV Pb-Lα line, spectrum B, corresponding to the 12.64 keV Pb-Lβ line, and spectrum C, corresponding to the 14.76 keV Pb-Lγ line. The Lα-line/Lβ-line intensity ratio is roughly 10:6 or 10:5, while the Lβ-line/Lγ-line intensity ratio is roughly 10:1.

From the above discussion, the intensity ratio for Kα-line and Kβ-line emissions, which form a doublet, differs from that for Lα-line and Lβ-line emissions, which form a triplet. This observation may be used to determine whether peaks in measured spectra correspond to Kα-line and Kβ-line emissions or to Lα-line and Lβ-line emissions*7. Note that, in XRF spectra, Kβ-line energies are higher than Kα-line energies, so that the horizontal-axis positions of Kβ-line peaks lie to the right of the positions of Kα-line peaks. Similarly, Lβ-line energies are higher than Lα-line energies (so Lβ-line peaks lie to the right of Lα-line peaks) and Lγ-line energies are higher than Lβ-line energies (so Lγ-line peaks lie to the right of Lβ-line peaks). This observation is useful for, e.g., deciphering whether features appearing in measured XRF spectra are attributed to Kα and Kβ lines for a given element or to Lα and Lβ lines for that element.

Overlapping features in XRF spectra

Our apparatus is an energy-dispersive X-ray fluorescence analyzer based on a semiconductor detector with an energy resolution of 180-205 eV; this means it is capable of simultaneously detecting the energies of fluorescent X-ray emissions from multiple elements. However, if the energies of X-rays emitted from distinct elements are nearly equal—specifically, if they differ by less than our detector resolution of 205 eV = 0.205 keV—then the two spectra overlap in our setup. For example, as noted above, the green pigment *emerald green* includes both Cu and As among its primary constituent elements, and thus fluorescent X-rays emitted simultaneously from both of these elements appear in measured XRF spectra. If *emerald green* was the only colorant used in a specimen, then, as shown in Figure 19a, the Kα-line and Kβ-line emissions from Cu and As are not close in energy, so there would be no overlap and we would have no difficulty measuring both spectra simultaneously. However, in practice emerald green is used together with other colorants; for example, the white pigment *white lead* is sometimes added to increase brightness and yield a brighter hue. For a specimen in which the white pigment *white lead* is combined with dark-green *emerald green* to yield a brighter shade of green, XRF measurements simultaneously detect the energies of X-ray emissions from *emerald green* (Figure 19a) and from *white lead* (Figure 19b), yielding the spectrum shown in Figure 19c, in which the As-Kα line emission from *emerald green* overlaps with the Pb-Lα line emission from *white lead*. Note that this phenomenon is not limited to

---

*7 The elemental analysis software installed on the PC attached to our X-ray fluorescence analyzer can automatically detect peaks in XRF spectra and determine the corresponding elements from their energies. Nonetheless, an understanding of how Kα/Kβ-line intensity ratios differ from Lα/Lβ-line intensity ratios is important not only for confirming the accuracy of results reported by this software but also for interpreting the results of XRF spectra published in the literature.

the specific case of *emerald green* mixed with *white lead*, but would arise for any specimen in which As and Pb are simultaneously present, due to the similar energies of the As-Kα line (10.532 keV) and the Pb-Lα line (10.550 keV).

Similarly, the yellow pigment *orpiment* (As_2S_3) is sometimes combined with the red pigment *vermilion* (HgS) to yield orange coloration. When these two colorants are simultaneously present, we have Kα-line (10.532 keV) and Kβ-line (11.726 keV) emissions from As, a primary constituent of orpiment, together with Lα-line (9.987 keV) and Lβ-line (11.821 keV) emissions from Hg, a primary constituent of vermilion; this results in an overlap between the As-Kβ line (11.726 keV) and the Hg-Lβ line (11.821 keV). The same difficulty would arise even if *orpiment* and *vermilion* were present in separate but neighboring regions of a specimen.

As an example, consider the *bingata* garment pattern shown in Figure 20. For this specimen, XRF spectra measured in yellow regions of the garment contained three spectral peaks: peak A, near 9.98 keV; peak B, near 10.54 keV; and peak C, near 11.73 keV. A first observation is that the intensities for peaks B and C differ by a factor of approximately 10, i.e., the B:C intensity ratio is 10:1. This suggests that the higher-intensity peak B is a Kα-line peak, while the lower-intensity peak C is a Kβ-line peak forming a doublet with peak B. Next, referring to Table 2, we ask: What pigment would emit both a Kα line corresponding to an energy of 10.54 keV and a Kβ line corresponding to an energy of 11.73 keV? As the measured specimen region is primarily yellow in color, we deduce that peak B corresponds to the Kα line (10.532 keV) for As—a principal constituent of *orpiment*—while peak C corresponds to the Kβ line (11.726 keV) for As. Based on these findings, we conclude that the yellow pigment here is *orpiment*.

The only remaining mystery is the origin of peak A at 9.98 keV. Again referring to Table 2, we ask: Which element emits fluorescent X-rays corresponding to this energy? A quick search reveals the answer: Hg, whose Lα line energy is 9.987 keV, and whose Lβ line—which forms a doublet with the Lα line—lies at 11.821 keV, and thus overlaps in our measured spectrum with peak C, i.e., with the As-Kβ line at 11.726 keV.

As this example demonstrates, a thorough understanding of the phenomenon of overlapping spectra is essential for correctly interpreting spectral measurements—and for deciphering the mystery of "Where did this peak come from?!"

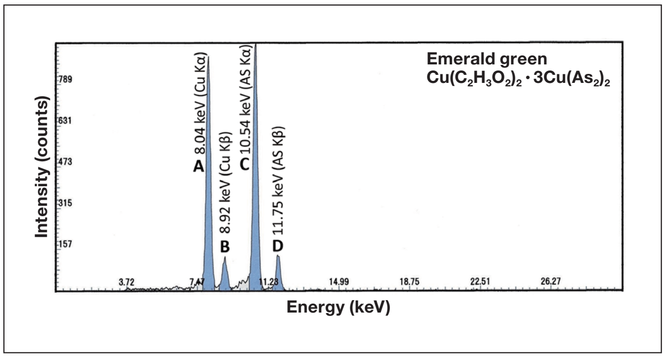

Fig. 19a XRF spectrum of *emerald green.*

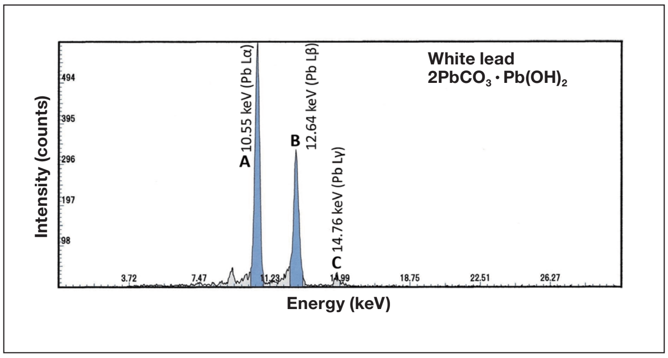

Fig. 19b XRF spectrum of *white lead.*

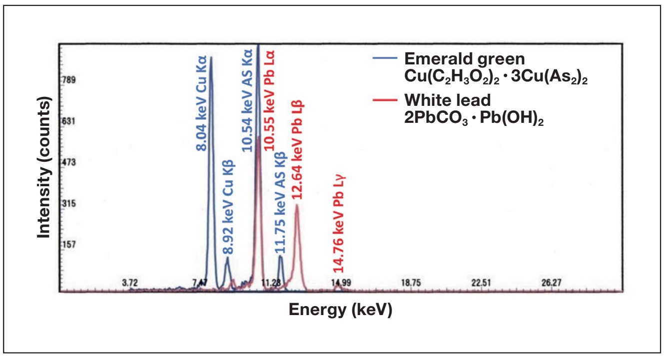

Fig. 19c Measured XRF spectrum for a specimen containing both *emerald green* and *white lead*, illustrating overlapping spectral features.

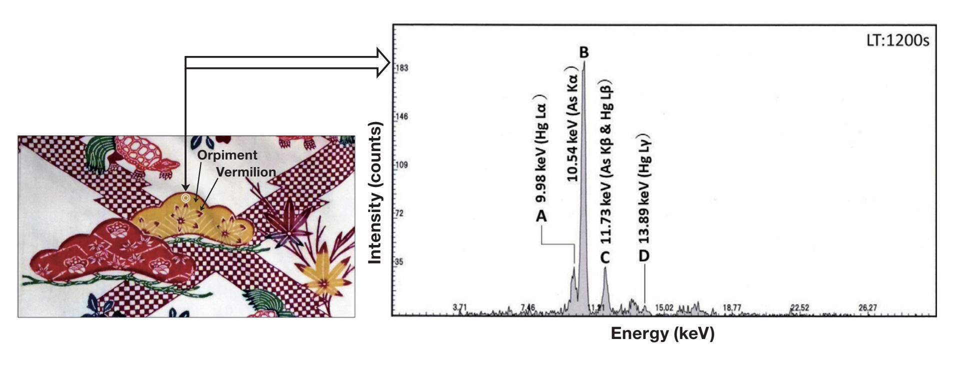

Fig. 20 XRF spectrum (right) measured for the yellow-colored region of the specimen shown on the left, which contains the yellow pigment *orpiment* and lies adjacent to a red-colored specimen region containing the red pigment *vermilion*.

Analyzing measured XRF spectra for the pigment smalt[10)]

In some cases, an understanding of the historical trajectory that led to the introduction of a new pigment can serve to facilitate the challenge of simultaneously analyzing multiple constituent elements in specimens. As one example, Figure 21 shows a cultural-property specimen for which our measured XRF spectrum successfully identified the presence of the classical blue pigment *smalt*. The specimen in this case is an artwork entitled *Images of Rashomon* (dimensions: 134.4 cm tall × 102.3 cm wide) that was painted on a wooden prayer board and left as an offering to the Asakura Shrine in Fukui Prefecture in Japan in the second year of the Tenna era (1682). The painting depicts the samurai warrior Watanabe no Tsuna, and we measured XRF spectra for a blue region painted on the dome of the warrior's helmet.

Smalt, the oldest man-made Co-based pigment, is made by adding Co ore ($[Co,Ni]As_{3-2},Fe$) to molten silicate glass (SiO_2,K_2O,CaO) to yield a blue-colored glass, which is then ground into a powder[13,14)]. The Co content of the ore is the source of the blue coloration, but the ore also contains Fe, Ni, and As. Armed with this knowledge, we can determine the origins of various elements whose presence is indicated by the XRF spectrum in Figure 21. Ca originates from silicate glass, while Fe, Co, Ni, and As originate from Co ore. Although there is a paint named *smalt* that is commercially available today, it is made with Co as the sole source of blue coloration and is distinct from the classical pigment known as *smalt*. The spectral features marked “scatter” in Figure 21 are due to X-rays emitted from the ^{241}Am source (with energies of 13.95 keV and 17.74 keV) that undergo scattering processes and are erroneously captured by the detector; they represent an instrumental artifact and do not indicate peaks associated with elements present in the sample.

Analyzing XRF spectra is a technique that works well for inorganic substances such as pigments and metals, but cannot be used for organic substances such as dyes. The reason for this is that the fluorescent X-rays emitted from C, a component of *sumi* ink, have extremely low energies—just 0.277 keV—and cannot be detected by any X-ray fluorescence analyzer currently available. This also means that XRF analysis cannot be used to study dyes or other organic substances structured primarily around C bonds.

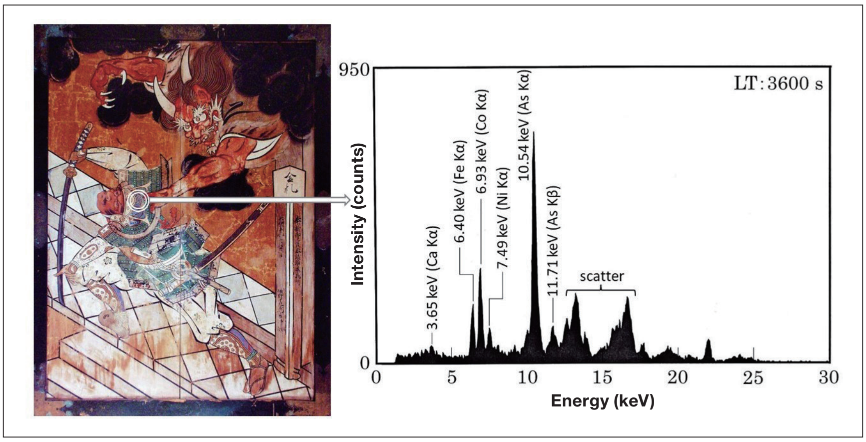

Fig. 21 Left: *Images of Rashomon*, an artwork presented as an offering to a shrine in Japan's Edo period [Tenna 2 (1682)]. Right: XRF spectrum measured for a blue-pigment-filled subregion of the dome of the warrior's helmet.

Combining XRF spectra and visible/near-infrared reflection spectra to unravel the mystery of green tsuikin[15)]

Tsuikin is a method for transferring pictorial patterns onto lacquerware. In this technique, a pigment is uniformly blended with lacquer to yield a paste known as *tsuikin-mochi*, which is stretched into a thin sheet, cut into shapes appropriate for the pattern, and affixed to lacquerware items. The cultural property shown in the lower left panel of Figure 22—a tray made from black-lacquered wood that is recognized as a Japanese national treasure—was decorated by *tsuikin*. The other panels in Figure 22 show the results of various non-destructive analyses of this specimen: an XRF spectrum measured for a yellow-colored region of the *tsuikin* decoration (upper left), an XRF spectrum measured for a green-colored *tsuikin* region (upper right), and a visible/near-infrared reflection spectrum measured for the same green-colored *tsuikin* region (lower right).

Looking first at the XRF spectrum for the yellow *tsuikin* region (upper left), we see two peaks—peaks A and B—at energies of 10.54 keV and 11.77 keV, respectively, with the intensity of peak A being approximately ten times greater than that of peak B (intensity ratio A:B = 10:1). This suggests that peaks A and B respectively indicate Kα and Kβ lines for some element. Consulting Table 2, we find that this element is As, whose Kα and Kβ lines have energies of 10.532 keV and 11.726 keV, respectively. Hence we conclude that *orpiment* (As_2S_3) was used to produce the yellow color of this specimen region. In other words, the yellow-colored pictorial pattern on the tray was produced by blending *orpiment* uniformly with lacquer to yield a *tsuikin-mochi* paste.

Looking next at the XRF spectrum for the green *tsuikin* region (upper right), we see two peaks (peaks B and C) with intensities differing by roughly a factor of ten (intensity ratio B:C = 10:1), again suggesting Kα and Kβ lines for some element. Matching the positions of the peaks to data in Table 2, we conclude that peaks B and C are the Kα and Kβ lines for the yellow pigment *orpiment*, respectively. This spectrum also exhibits a peak (peak A) at 6.39 keV, which we identify as the Fe-Kα line (energy: 6.400 keV). We attribute the presence of Fe in this region to the black lacquer[16)] used to coat the tray, which was prepared by adding Fe powder or pellets to liquid lacquer; the Fe-Kα line seen here is not due to Fe present in the yellow *tsuikin* region. This interpretation is also supported by the fact that the Fe-Kα and Fe-Kβ lines both appear prominently in the XRF spectrum measured for a region of the specimen containing only black lacquer, with no *tsuikin* colorations.

Thus, we now face this question: Which blue colorant was used in combination with yellow-colored *orpiment* to yield the green coloration? It has been suggested that *malachite* may have been used in some cases to yield green lacquer[16)]. However, we see here neither the Cu-Kα (8.041 keV) or Cu-Kβ (8.905 keV) lines that we would expect to find for copper-containing malachite ($CuCO_3 \cdot Cu(OH)_2$). According to Ref. 16, "Looking at historical records from long-past eras, we find statements indicating that the *indigo* used was the same *indigo* used to make *indigo* dye". But Ref. 17 says that "although *indigo* existed at that time, it is unclear whether or not it was used in mixtures with orpiment." To clarify this murky situation, we switch to a different method of analysis: we measure visible/near-infrared reflection spectra for the same green *tsuikin* region, yielding the reflection spectrum shown at the lower right in Figure 22. Because this spectrum is measured for a *green*-colored region, it exhibits no peaks in the 400-500 nm wavelength interval corresponding to blue and violet. On the other hand, the shape of the spectral curve—with the reflectance increasing in the near-infrared region beyond 700 nm—resembles the spectrum of *indigo* in Figure 11C. The *indigo* in *indigo* dye, when stored in the clay or ceramic jars commonly used as storage containers, tends to produce water-soluble leuco salts (green-colored), which are oxidized in air to yield a non-soluble crystalline blue substance used as a pigment[18)]. Based on these findings, we conclude that green *tsuikin* regions are produced by blending the yellow colorant *orpiment* with the blue colorant *indigo* to yield a green colorant.

A cultural property that does not involve *tsuikin* but is nonetheless relevant here is a *Gold-inlaid green-lacquered wood tray* held by the Okinawa Churashima Foundation. A *green* colorant has been applied to the four corners of this tray, and the XRF spectra and visible/near-infrared reflection spectra measured for these green regions are similar to those in Figure 22. Thus we conclude that, for this specimen as well, *orpiment* was blended with *indigo* to yield a *green lacquer* that was applied to the specimen[19)].

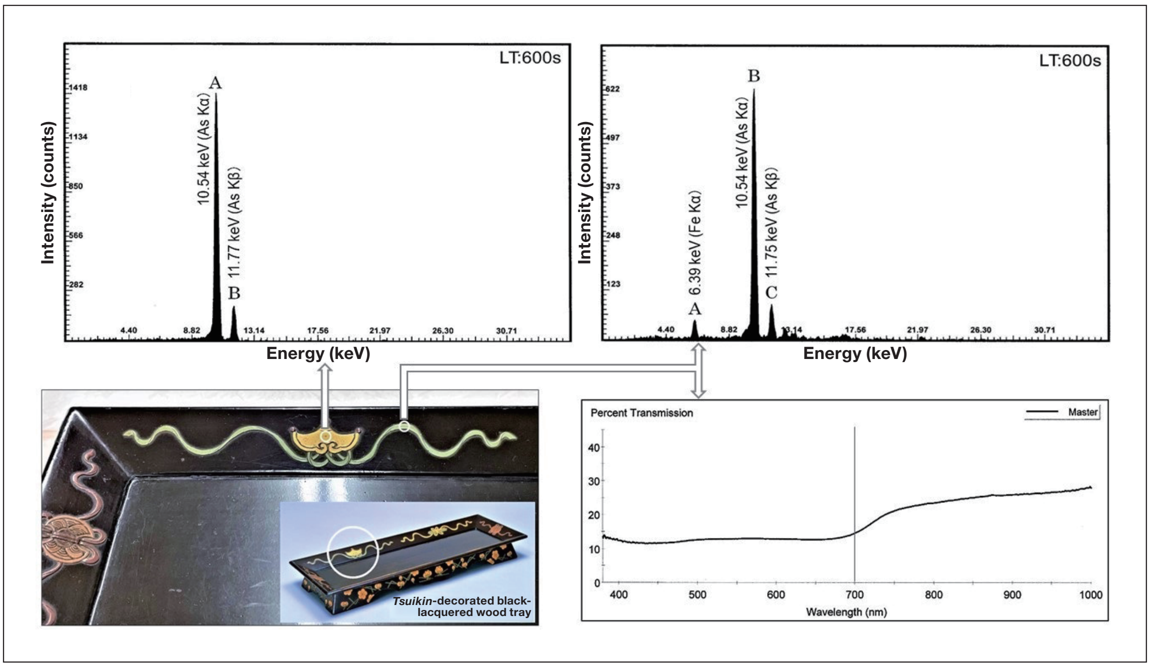

Fig. 22 Lower left: A tray recognized as a Japanese national treasure made from black-lacquered wood and decorated by *tsuikin*,. Upper left: XRF spectrum measured for a *yellow* region of the *tsuikin* decoration. Upper right: XRF spectrum measured for a *green* region of the *tsuikin* decoration. Lower right: Visible/near-infrared reflection spectrum measured for the same *green* region of the *tsuikin* decoration.

X-ray fluorescence analysis of (glazed) earthenware pottery[20)]

The Japanese national treasure in Figure 17, a square-base candle stand with green *Ryoku-Yu* glaze, is one example of *Ryoku-Yu* glazed pottery. According to Ref. 21, *Ryoku-Yu* glaze—also known as *Ao-Oribe-Yu* ("green glaze")—is prepared by "adding copper oxide (Cu_2O) to transparent wood-ash glaze or lime glaze, then firing; in some cases, impurities such as chalcanthite (copper sulfate $CuSO_4 \cdot 5H_2O$), shavings of brass [an alloy of copper (Cu) and zinc (Zn)], or shavings of copper may be added to the copper component to add color". Figure 23 shows the XRF spectrum measured for the skin layer of the *Ryoku-Yu* glazed candle stand. We identify six peaks in this spectrum: peak A (3.69 keV), peak B (6.41 keV), peak C (8.00 keV), peak D (8.67 keV), peak E (8.88 keV), and peak F (9.54 keV). The highest-intensity peak is peak C, which corresponds to the Cu-Kα line (8.041 keV) and reflects the presence of Cu as the principal colorant in the fired glaze. Peak E corresponds to the Cu-Kβ line (8.905 keV). The next highest-intensity peak is peak D, at an energy of 8.67 keV, which is roughly ten times more intense than peak F (9.54 keV) (intensity ratio D:F = 10:1). This suggests that peaks D and F correspond to the Zn-Kα (8.631 keV) and Zn-Kβ (9.572 keV) lines. Thus we conclude that Cu and Zn coexist in the portions of this green glaze that add coloring upon firing, and that the glaze consists of brass shavings. Finally, peaks A (3.69 keV) and B (6.41 keV) correspond to the Ca-Kα line (3.691 keV) and the Fe-Kα line (6.400 keV); Ca and Fe are present in the clay materials and lime-ash glazes (calcium carbonate $CaCO_3$) used as raw materials.

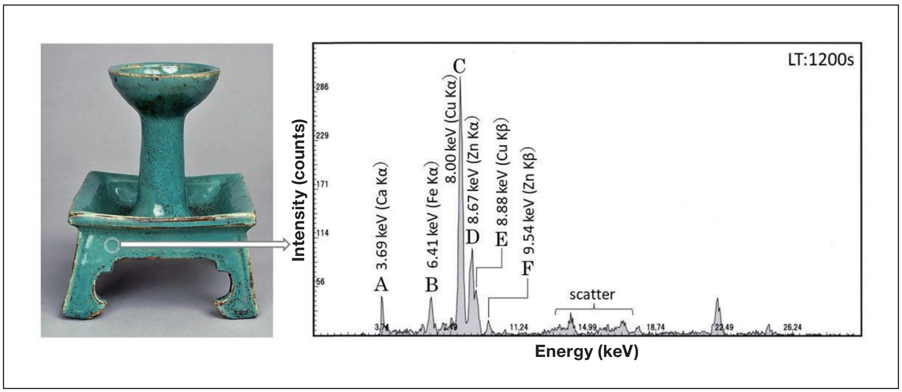

Fig. 23 XRF spectrum measured for the *Ryoku-Yu* glaze used in the Japanese national treasure in Figure 17.

5. Three-dimensional Fluorescence (3DF) Spectra

5-1. Instruments

At present, we use two similar analytical instruments to measure 3DF spectra: For on-site analyses at museums or other remote locations, we use a Hitachi F-2500 fluorescence spectrophotometer (weight: 35 kg) equipped with an optical fiber, while for analyses in our home laboratory we use a Hitachi F-7000 fluorescence spectrophotometer (weight: 41 kg) permanently installed in a fixed location and similarly equipped with an optical fiber. In some cases, the cultural property we wish to analyze cannot be moved, and in some cases we must analyze not only the cultural property but also various aspects of the environment in which it is housed, such as the vessels in which it is stored. In such cases, we transport our F-2500 system to the remote site—either by hiring a shipping company capable of handling delicate instruments, or by hand-delivering the system ourselves in a private vehicle. In the latter case the spectrophotometer and the optical fiber are packaged in a custom-designed protective metal carrying case. Needless to say, among the accessory items transported with the system for use at remote sites are samples of rhodamine B and other reagents, as well as secondary standard light sources, to facilitate the steps required to prepare the instrument for use at the remote site, including measuring instrument response functions (and applying spectral corrections) and measuring instrument properties in the long-wavelength fluorescence region. Figure 24 shows a simplified schematic diagram of the optical fibers we use for the F-2500 and F-7000; thick lines in this diagram represent the shapes of fibers. Initially, we adopted a fiber configuration in which the excitation side used 48 fiber cores bundled into a single cable, while the fluorescence side used 32 fiber cores arranged in a double-bundle configuration designed to wrap around the perimeter of the excitation cable. However, we now use a different configuration in which both the excitation-side fibers (total of 48 cores) and the fluorescence-side fibers (total of 48 cores) are dispersed and randomly bundled. To evaluate the performance of these two fiber configurations, we measured 3DF spectra (as shown in the center of Figure 26) under identical measurement conditions and compared the two fluorescent intensity values; the results demonstrated that the measured intensity was approximately 2.5 times greater for the random-bundle configuration than for the double-bundle configuration—even with an L39 filter installed on the fluorescence side to eliminate secondary light producing scattering artifacts in 3DF spectra—thereby allowing the detector to capture more of the fluorescent light emitted by measurement specimens[22)]. However, with the tip of the optical fiber positioned at a distance of approximately 5 mm from the specimen, the spot size—that is, the diameter of the region irradiated by the fiber—is approximately 3 mm for the double-bundled configuration, but expands to approximately 5 mm for the random configuration.

To measure 3DF spectra at remote sites using the F-2500 with this randomly-bundled optical fiber, we use a setup like that shown in Figure 25. We begin by covering the measurement sample (a *bingata* garment in the case of Figure 25) with a protective sheet from which we have cut out a circular hole approximately 30 mm in diameter. The sheet is positioned such that the center of this hole lies at a preselected measurement point on the specimen. Then we place the light-blocking box, into which the tip of the optical fiber is inserted, on top of the protective sheet (the mass of the box is 390 g), open its view portal, and look through this portal while adjusting the positioning to ensure that the tip of the optical fiber lies above the measurement point at a distance of approximately 5 mm from the specimen surface. Upon completing this preparation we begin the measurement. When adjusting the position of the light-blocking box after inserting the optical-fiber tip, it is desirable to pass visible light (e.g., 550 nm) through the fiber.

When we first began to pursue the research program described in this article, our analytical instrument was a Hitachi F-4010 fluorescence spectrophotometer. Natural dyes derived from animal or plant matter, whose molecular structure involves a significant prevalence of covalent double bonds[23)], exhibit characteristic excitation and fluorescence wavelengths, and thus it should be possible to use *fluorescence fingerprints*—contour-plots of 3D fluorescent spectra—to directly identify the dyes responsible for lending coloration to dyed fabrics. This was the reasoning that motivated the launch of our research program in the early 1990s[24)]. Later, we replaced the F-4010 with our current F-4500 system, developed the optical-fiber approach described above, and expanded the focus of our research from dyed fabrics to *ukiyo-e* prints[25,26)]. It was at this juncture that we began developing our procedure for making on-site measurements with the F-2500, and since then we have performed non-destructive analyses of *ukiyo-e* prints at museums throughout Japan and at the Museum of Fine Arts, Boston, USA[27)]. At present, our research is focused on using Hitachi's F-7000 system for non-destructive analysis of lacquers used to make lacquerware.

From the moment we began this research program in the 1990s, and continuing through to the present day, there has been a continual expansion of the capabilities of fluorescence spectrophotometers. Among the advances that we find most valuable are the dramatic reduction in measurement times (facilitated by higher scan speeds), the significantly longer lifetimes of xenon-lamp light sources, and the proliferation of data-analysis functionality. We are also considering Hitachi's F-2700 compact fluorescence spectrophotometer (weight: 41 kg) as a possible replacement for the F-2500 system we currently use for on-site measurements.

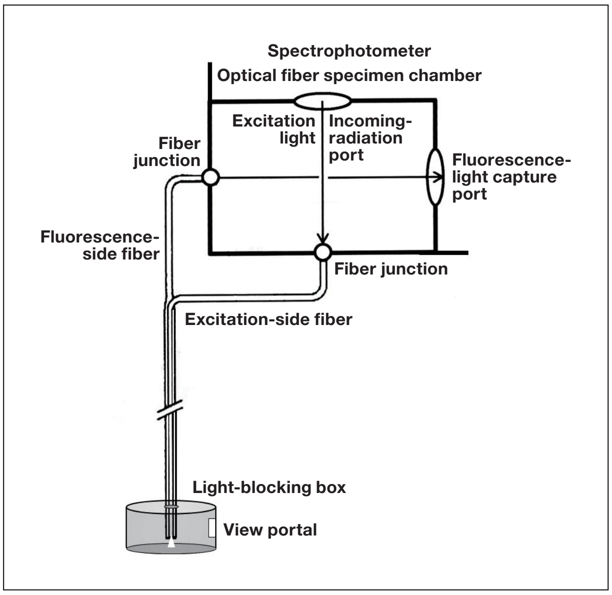

Fig. 24 Optical fiber configuration.

Fig. 25 Measuring 3DF spectra of *bingata* specimen.

5-2. Information derived from 3DF spectra

For a specimen of the dye *safflower* (coloring matter: carthamin), Figure 26 shows the measured 3DF spectrum and its contour-plot representation or *fluorescence fingerprint*. 3DF spectra are measured by successively irradiating the specimen at a sequence of excitation wavelengths and measuring the fluorescence spectrum at each excitation wavelength. To perform such a measurement, we specify values for various parameters—the excitation wavelength range (typically 250-600 nm), the wavelength interval between successive excitation wavelengths (typically 5 nm), and the wavelength range over which to measure fluorescence spectra for each excitation wavelength (typically 300-700 nm)—then simply initiate the measurement. If we watch in real time as the measurement proceeds, we see a gradual sequence of variations in the fluorescence spectra measured for each excitation wavelength. For typical values of the scan parameters—excitation wavelength ranging from 250 to 600 nm in 5 nm steps—a total of 71 separate fluorescence spectra are measured (Figure 26, left). After the full measurement is complete, these 71 spectral curves are combined to yield a three-dimensional plot (Figure 26, center) depicting the variation of fluorescence intensity with respect to both excitation wavelength (Ex) and fluorescence wavelength (Em). This plot is known as a *three-dimensional fluorescence (3DF) spectrum*[28). Note that this plot is reminiscent of bird's-eye view of a topological map depicting a mountain range; in the same way that a three-dimensional topological map can be converted into a two-dimensional contour map—with the altitude information conveyed by three-dimensional features in the former now encoded by contour lines in the latter—we can convert the 3DF spectral plot (Figure 26, center) into a contour-plot (Figure 26, right). The result, known as a *fluorescence fingerprint*, furnishes a unique signature to the measured specimen, which may be used, for example, to identify the dyes used to color cloth fibers or to color *ukiyo-e* prints. The contour-plot shown at the right in Figure 26 is a fluorescence fingerprint measured for the pigment *carthamin* in the dye *safflower*, whose molecular structure is shown in the lower central portions of the figure. Because this fluorescence fingerprint is derived from the particular molecular structure of this dye, any other dye—or any other molecular structure—would have a distinct fingerprint.

In forensic science, human fingerprints are used to identify specific individuals. For example, in Japan, fingerprints left at crime scenes (latent fingerprints) are compared against two databases maintained by the Fingerprint Center of

Japan's National Police Agency: one database stores the fingerprints of more than 8 million convicted criminals, and a second database contains billions of latent fingerprints left at past crime scenes. Fingerprint comparisons are automated by the Automated Fingerprint Identification System (FAIS), with the final determination as to whether or not a given fingerprint matches a fingerprint in the database being made by an expert forensic analyst[29,30].

The use of human fingerprints to identify crime suspects furnishes a partial analog to the use of fluorescence fingerprints to identify dyes in cultural properties. The fluorescence fingerprints measured for a cultural property, which correspond to latent fingerprints left at a crime scene, are compared against fluorescence fingerprints measured for laboratory-prepared standard specimens; if a match is found, we may conclude that the dye used in the cultural property is identical to the dye used to prepare the standard specimen. To construct a reference database of fluorescence fingerprints for known substances, we perform measurements of silk fabric specimens dyed with common natural dyes and of *washi* paper specimens colorized by pressing natural coloring matters into the paper.

Figure 27 shows fluorescence fingerprints measured for specimens of silk fabric colorized by single dyes and for *washi* paper colorized by single dyes. When a desired colorization effect cannot be achieved using any one single dye, multiple dyes may be combined; for example, in ancient Japan the colors *scarlet* and *green* were each realized by over-dying using two different dyes[31]. Figure 28 shows a fluorescence fingerprint measured for a standard silk-fabric specimen dyed scarlet by the yellow dye *Amur cork (berberine)*, and then over-dyed with the red dye *safflower*. Figure 29 shows a fluorescence fingerprint measured for a standard silk-fabric specimen dyed green by the blue dye *indigo*, and then over-dyed with the yellow dye *Amur cork*. Figures 28 and 29 also show enlarged subregions of the full fluorescent-footprint images. The low measured values of the fluorescence intensity in these cases have the effect of obscuring contour-line peaks in the full fluorescence fingerprint plots, so we present these enlargements with lower intensities to ensure that contour-line peaks are readily discernible.

As is clear from a comparison of these fluorescence fingerprints, the fluorescence fingerprint measured for a given dye has a unique shape that is characteristic of the dye, with a unique contour-line peak defined by the maximum excitation wavelength (λEx) and the maximum fluorescence wavelength (λEm), which are also characteristic of the dye. In fluorescence fingerprints for specimens dyed scarlet or green by over-dying using two different dyes, we see two distinct contour-line peaks, one produced by each of the dyes. The dyed silk fabrics measured to yield fluorescence fingerprints for our reference database of known colorants were provided by our research collaborator Yasuko Shimoyama, an expert in the field of dyes, while the colorized *washi* prints measured to yield fluorescence fingerprints for our database were provided by the late Shinya Katsuhara (Painter name: Inuki Tachihara). Note that fluorescence fingerprints (contour-line patterns) measured for fabrics dyed with a given dye should be independent of the type of fabric—which may be silk, hemp, or another fiber—and should be identical to fluorescence fingerprints measured for *washi* specimens colorized by the same dye.

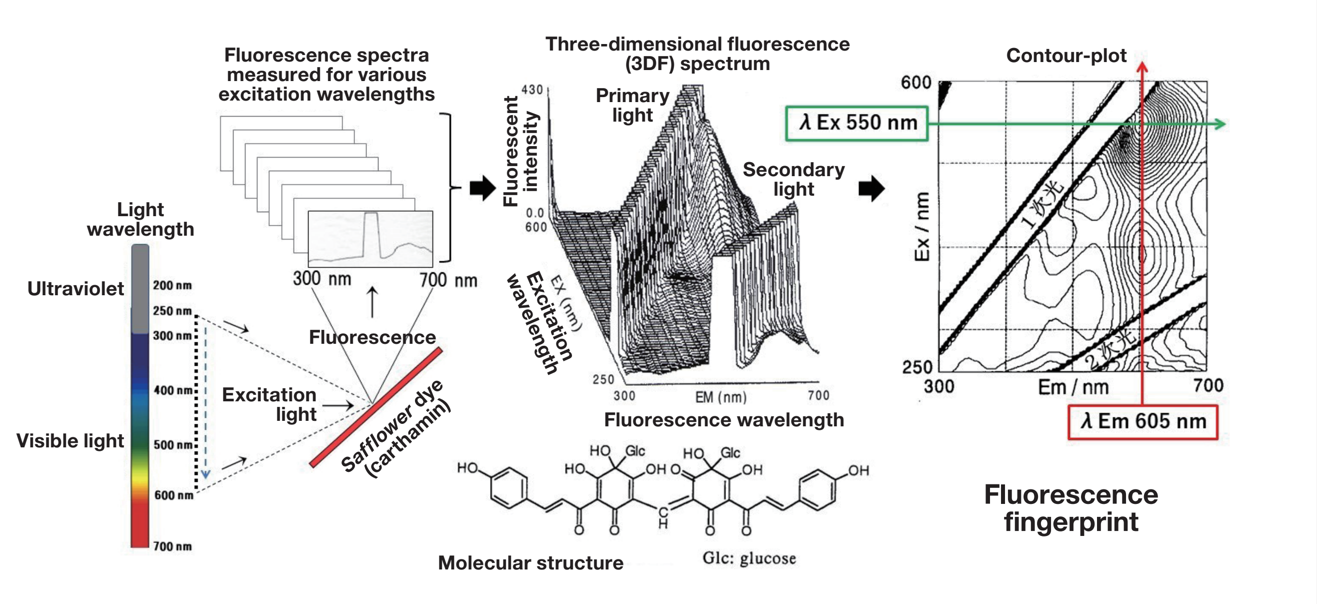

Fig. 26 Measured 3DF spectrum for *safflower* dye (carthamin) and corresponding contour-plot (or *fluorescence fingerprint*).

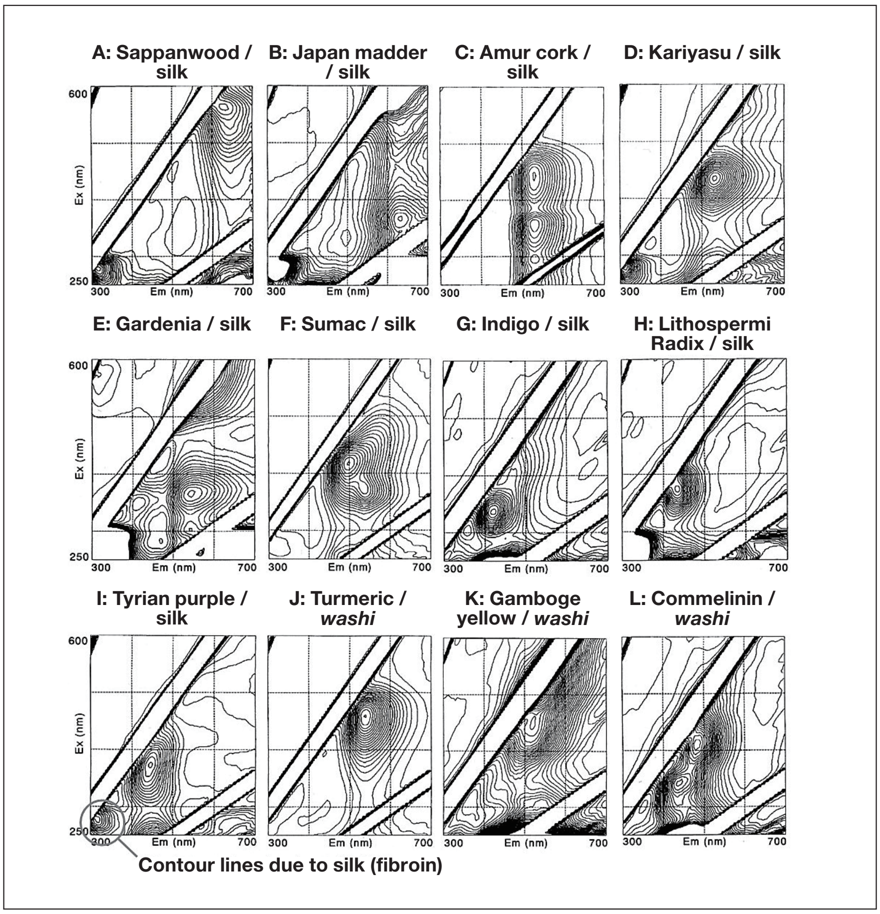

Fig. 27 Fluorescence fingerprints for standard specimens consisting of silk fabrics colorized by single dyes or *washi* paper colorized by single dyes.

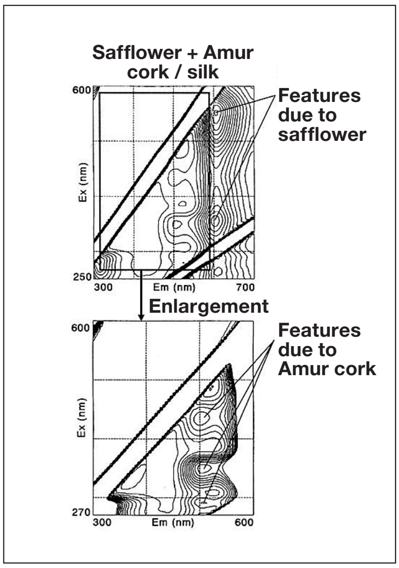

Fig. 28 Fluorescence fingerprints for standard specimens of silk fabrics dyed scarlet by *Amur cork*, and over-dyed with *safflower*.

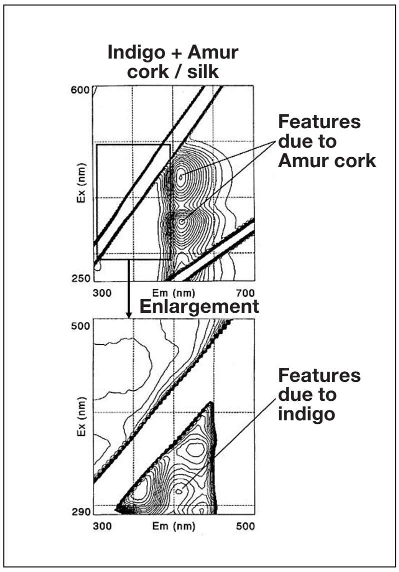

Fig. 29 Fluorescence fingerprints for standard specimens of silk fabrics dyed green by *indigo*, and over-dyed with *Amur cork*.

Identifying the colorants used to dye fabrics in past eras

Figure 30 shows a brocade, discovered in 1994 in Lhasa, Tibet, that dates from the 16th or 17th century (from the late Muromachi era to the Azuchi-Momoyama era of Japanese history) and is created from fabric made in China. The decorative motifs woven into this brocade include: a dragon, which was thought to symbolize the Emperor of China, woven from gold thread and incorporating five talons; a cloud, woven from blue and green thread; and a flame woven from scarlet thread. Susumu Shirai, then the chief engineer of Tatsumura Textile Co., Ltd., named this object the "brocade with dragon and cloud patterns on light-brown ground". With dimensions of 290 mm (tall) by 280 mm (wide), the brocade is too large to fit into the specimen chamber of our spectrophotometer; instead, we used our optical-fiber probe setup to make measurements of specific subregions. First, Figure 32 shows the fluorescence fingerprint obtained from measurements (at point X) of the blue thread used to weave the cloud motif shown on the left in Figure 31. This fluorescence fingerprint matches that obtained for the *indigo*-dyed silk fabric in Figure 27G. Next, Figure 33 shows the fluorescence fingerprint obtained from measurements (at point Y) of the green fabric used to weave the cloud motif. This fluorescence fingerprint matches that obtained for the silk fabric dyed with both *indigo* and Amur cork in Figure

29. Y1 and Y2 indicate contour-map peaks due to Amur cork dye, while Y3 indicates a contour-map peak due to *indigo* dye. Finally, Figure 34 shows the fluorescence fingerprint obtained from measurements (at point Z) of the scarlet thread used to weave the flame motif. This fluorescence fingerprint and the peak contour line match the measured data shown in Figure 28 for silk fabric dyed with both safflower and Amur cork. Contour-line peaks Z1 and Z2 are due to safflower dye, while peaks Z3, Z4, and Z5 are due to Amur cork dye. Based on these findings, we conclude that the blue thread woven into the brocade is colored by *indigo* alone, the green thread is colored by both *indigo* and Amur cork, and the scarlet thread is colored by both safflower and Amur cork[32-34].

Fig. 30 A brocade dating from the 16th or 17th century and known as the "brocade with dragon and cloud patterns on light-brown ground". The measurement positions are indicated on the back side of the brocade (right).

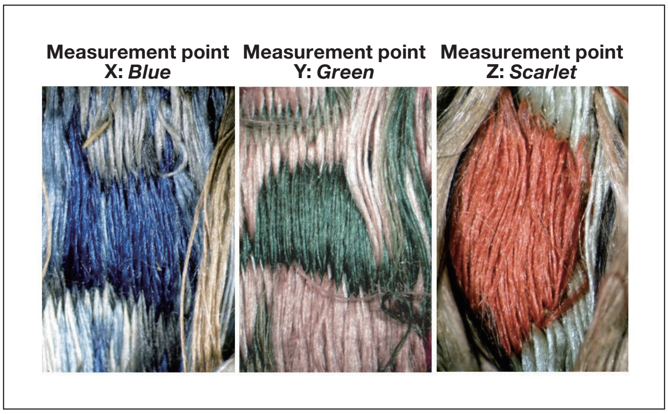

Fig. 31 Measurement points for brocade specimen in Figure 30.

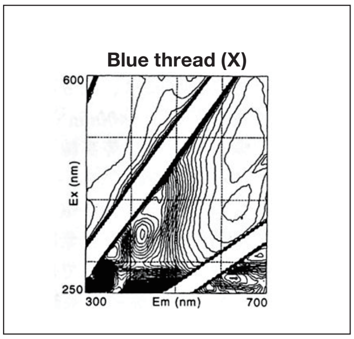

Fig. 32 Fluorescence fingerprint obtained from measurements of blue thread in brocade (measurement point X).

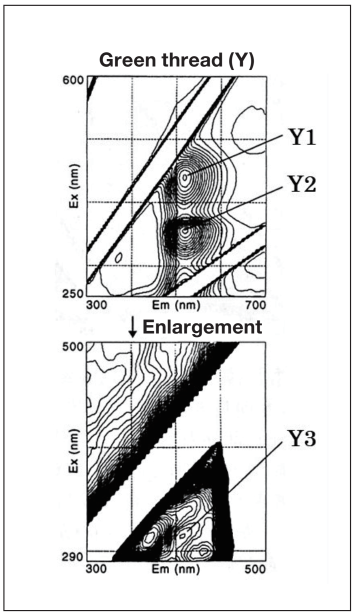

Fig. 33 Fluorescence fingerprint obtained from measurements of green thread in brocade (measurement point Y).

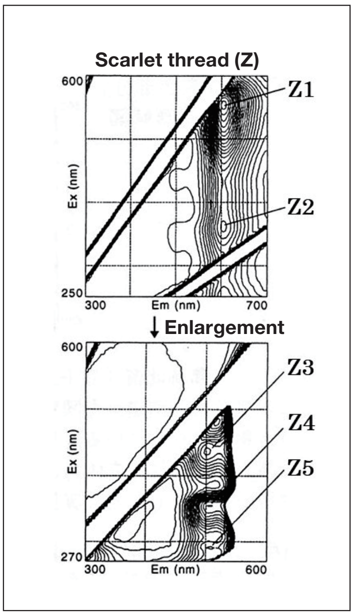

Fig. 34 Fluorescence fingerprint obtained from measurements of scarlet thread in brocade (measurement point Z).

Analyzing green colorants used in ukiyo-e prints

By analyzing measured 3DF spectra and XRF spectra, we showed that a mixture of *indigo* dye and orpiment (As_2O_3) pigment was used as a green colorant in a *ukiyo-e* print[35]. The *ukiyo-e* print in question was published around 1821 (Bunsei 4, in the late Edo period) as part of a three-print series by Gototei Kunisada titled "Eight views of Edo: Evening Snow at Mokuboji". Figure 35 shows the fluorescence fingerprint and XRF spectra obtained for a measurement point lying within a green region of the print.

We first note that the fluorescence fingerprint obtained for this green region resembles the fluorescence fingerprint for *indigo* shown in Figure 27G. However, the maximum-excitation wavelength (λEx), indicated by the peak contour line, is shifted slightly in the long-wavelength direction compared to that for *indigo*. The presence of elemental As is also detected in this green-colored region, from which we conclude that the yellow pigment *orpiment* was used. To proceed, we prepared a standard specimen consisting of a mixture of blue-colored *indigo* and yellow-colored orpiment applied to *washi* paper, then measured 3DF and XRF spectra for this specimen. As expected, the XRF spectrum for the standard specimen reveals the presence of As, and we obtained the fluorescence fingerprint shown in Figure 36. This fluorescence fingerprint matches that obtained for the green region of the *ukiyo-e* specimen in Figure 35, and the positions of the peak contour lines (λEx/λEm) match as well. Based on this experimental confirmation, we conclude that the green colorant used at that time, not only in this *ukiyo-e* print but more generally, was a mixture of *indigo* and orpiment.

As a side note, this example raises two points of general interest. First, as we see from the fluorescence fingerprint for the green colorant produced by blending *indigo* and orpiment, features in fluorescence fingerprints due to dyes may appear distorted for specimens that also contain pigments. Second, the presence of paramagnetic ions such as Fe, Ni, Cr, Cu, or Co can dramatically reduce the fluorescence intensity emitted by fluorescent molecules (due to extinction effects), and thus extra care is required in such cases[22,36].

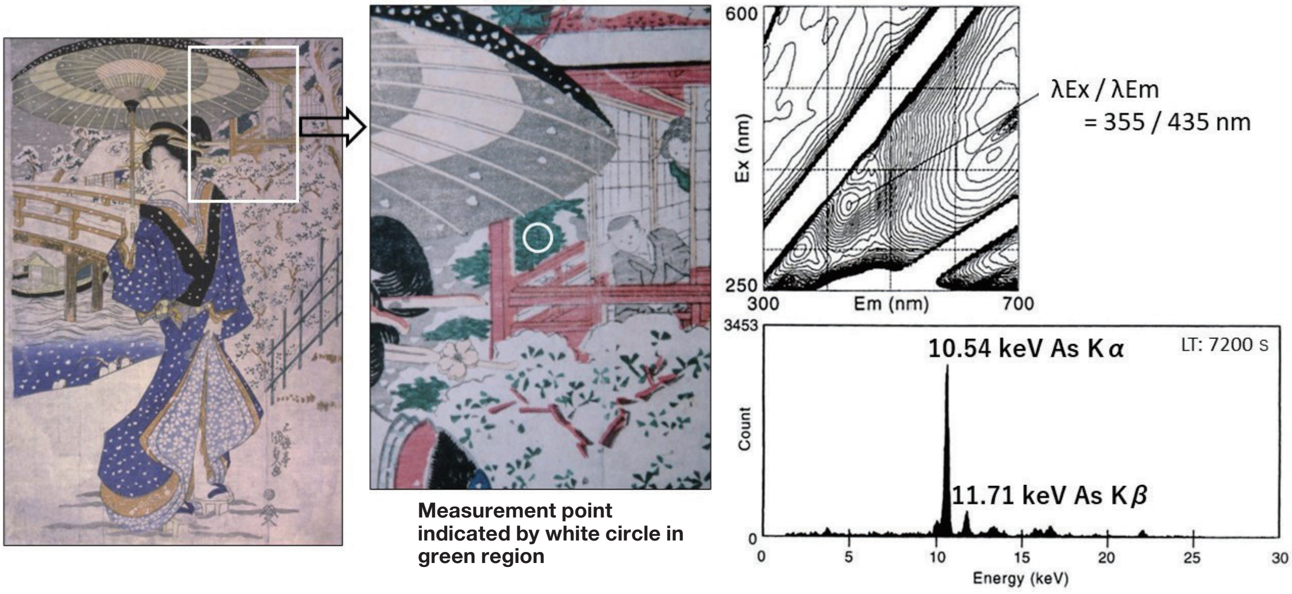

Fig. 35 3DF and XRF spectra measured for *ukiyo-e* print in series "Eight views of Edo: Evening Snow at Mokuboji".

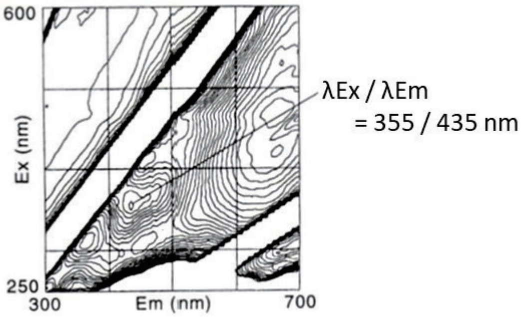

Fig. 36 3DF spectrum measured for standard specimen of green colorant produced by blending orpiment with *indigo*.

Fluorescence fingerprints for washi paper used in ukiyo-e prints

The production of *ukiyo-e* prints is a multi-stage collaboration between an artist, a sculptor, and a printer. The process begins when the artist gives the sculptor a rough draft of the image to be depicted by the print. The sculptor then prepares several items: a master printing key-block (or *omohan*) with lettering for the title of the image and the name of the artist, a schematic diagram (an outline sketch) of the image based on the artist's rough draft), and a colorization template (*kyougouzuri*) used to communicate color information between artist and sculptor. More specifically, the *kyougouzuri* is a version of the schematic diagram on which the artist adds instructions specifying the colors to be used in various subregions of the image. Based on these instructions, the sculptor then sculpts a set of *color blocks*—one for each color in the image—that will be used to print the colorized image, one color at a time. Next, the color blocks and the master key-block are delivered to the printer, who first uses the latter to form an outline image on *washi* paper before proceeding to production with the former. Consequently, the colorants used to produce the various colors in the image are stamped onto the uppermost layer of the *washi*. If *dyes* are stamped onto the *washi* then we can measure their 3DF spectra, while if *pigments* are stamped onto the *washi* then we can measure fluorescence emissions from the base layer of the *washi* (cellulose) itself and use this data as a fluorescence fingerprint.

Figure 37 shows XRF spectra and fluorescence fingerprints measured for a *ukiyo-e* print by Gototei Kunisada, renamed Utagawa Toyokuni the 3rd, entitled "Eight Views of Floating World: Night Rain at Kioroshi River". This *ukiyo-e* print was published in 1855 (Ansei 2), *after* Katsushika Hokusai first used Prussian blue to establish landscape images as a subgenre of *ukiyo-e*. Thus, by the time this print was published the use of Prussian blue in *ukiyo-e* prints had become standard.

The upper and lower sets of data plots in Figure 37 respectively indicate results for measurement point A—at which no colorants were stamped—and for measurement point B, at which blue colorant was stamped. Comparing the two datasets, we see that the fluorescence fingerprint for measurement point B—which lies in a blue-colored region of the specimen—matches the fluorescence fingerprint for measurement point A, which lies in an uncolored region. This demonstrates that the fluorescence fingerprint for measurement point B is in fact a fluorescence fingerprint for the *washi* (cellulose) itself, and that the blue colorant present at point B is a pigment that does not emit fluorescence at ultraviolet or visible wavelengths. Thus, based on the presence of Fe revealed by the measured XRF spectrum for measurement point B, we conclude that the blue pigment used here is Prussian blue. This example demonstrates that it cannot be immediately concluded that dyes were used simply because the fluorescence fingerprint was obtained from that region; one must also consider the fluorescence fingerprint for the background (empty regions or regions at which no colorant is present), and if the fingerprints match one must assume that a pigment has been stamped into the specimen and proceed to XRF analysis.

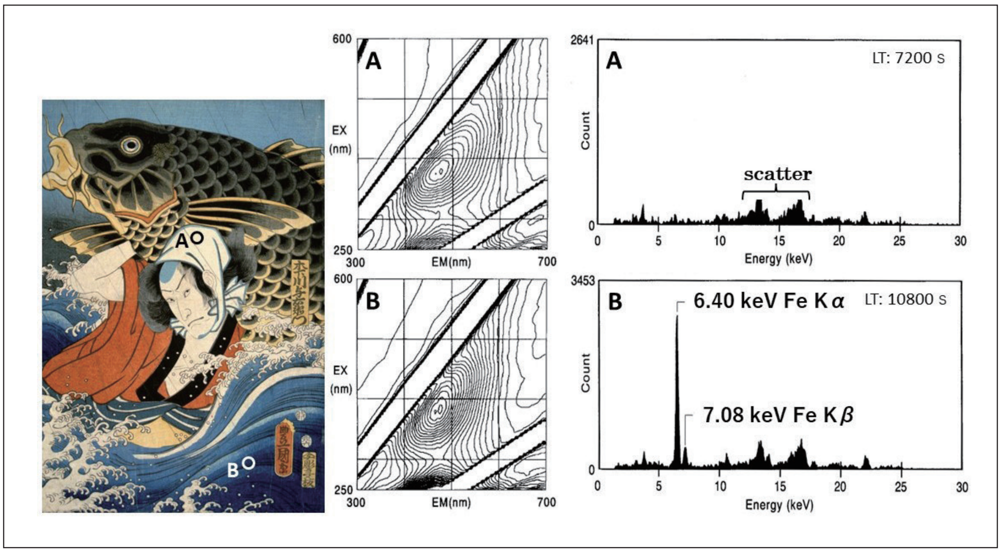

Fig. 37 Fluorescence fingerprints and XRF spectra measured for *white* (*washi*) and *blue* regions of *ukiyo-e* print "Eight Views of Floating World: Night Rain at Kioroshi River".

Learning new functional capabilities from fluorescence fingerprints

The study of bygone eras can yield valuable new insights and perspectives. Here we discuss a novel twist on this idea of *learning from the past*. Through our studies of colorants used for cultural properties in previous eras, we discovered a new type of optical functionality, which was successfully exploited to develop new commercial products of use in the modern world^37).

The fluorescence fingerprint for safflower shown in Figure 26 indicates absorption and excitation of 550 nm light with emission of 605 nm light. 550 nm light is seen by humans as green, while 605 nm light is seen as yellowish-red (or reddish orange). Interpreting this phenomenon as a demonstration of the functional optical capabilities of safflower, we investigated the possibility of exploiting this phenomenon to productive ends in the modern world. In contrast to LED light sources, which are now starting to become ubiquitous, the light sources used most often in previous eras included daylight fluorescent lamps and white fluorescent lamps. As any makeup artist can attest, even the most beautifully accentuated face can appear sallow under a fluorescent lamp. The reason for this, as shown in Figure 38, is that these fluorescent lamps emit blue-tinted and green-tinted light with high intensity, but emit almost no red-tinted light. This is the origin of the disappointing appearance of cosmetics when viewed under fluorescent lamps. But this diagnosis suggests a potential remedy: If one could find a substance with a particular optical functionality—specifically, the ability to absorb and eliminate blue-tinted and green-tinted light while generating red-tinted light—then this substance could be added to cosmetic products to mitigate the undesirable phenomenon described above. To test this idea we dyed cellulose with safflower, ground the cellulose into a fine powder, and added it to foundation and other cosmetic powders. This led to the emergence of new commercial products released in 1994 by the Japanese cosmetic firms Shiseido and Chifure[38,39].

On a separate but related note, in Europe, the red colorant cochineal (carminic acid) has been one of the most widely used colorants ever since the birth of lipstick. Cochineal does not fluoresce even when irradiated by ultraviolet light. However, blending cochineal with safflower has the effect of shifting the maximum fluorescence wavelength of safflower from 605 nm to longer wavelengths, and values in the range 625-635 nm (λEm/λEx ranging from 625/545 to 635/400 nm) were found to produce red-tinted light. Based on this discovery, in 2005 the French cosmetic firm Chanel introduced a lipstick named "AKA" for sale exclusively in Japan (Figure 39).

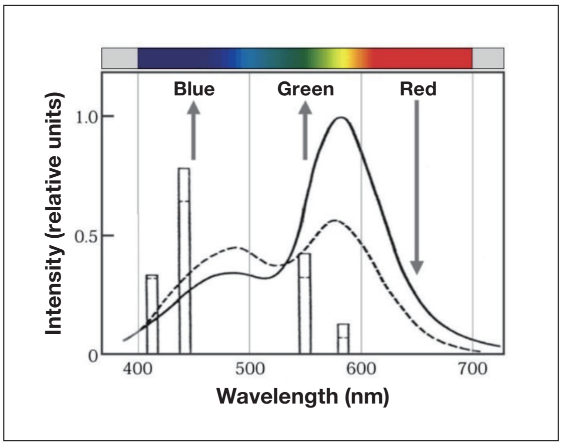

Fig. 38 Coloration of light emitted from fluorescent light sources. Solid curve: Daylight fluorescent lamp. Dashed curve: White fluorescent lamp.

Fig. 39 Chanel's *AKA* lipstick.

6. Conclusions

In this article we presented a collection of measurement techniques we have developed for non-destructive analysis of the colorants used in cultural properties. Our approach, which we have deployed and are continuing to deploy in a wide range of practical scenarios, involves collecting and analyzing five mutually complementary sets of experimental data: infrared photographs, microscopy images, visible/near-infrared reflection spectra, X-ray fluorescence spectra, and three-dimensional fluorescence spectra. For each type of data, we described the experimental procedures and analytical instruments used to perform the measurements, discussed the interpretation of the data and the information that may be derived from it, and presented practical case studies involving pigments and dyes used in cultural properties. Colorants may be pigments, dyes, or mixtures of both, and no single experimental approach could possibly suffice to lend full insight into both possibilities. At the very least, one requires a minimum of two types of analysis: X-ray spectroscopy, to investigate the elemental composition of pigments, and fluorescence spectroscopy (three-dimensional fluorescence spectra), to analyze dyes; moreover, the procedures and instruments used for these analyses must be amenable to on-site measurements at museums or other remote sites at which cultural properties are curated. As we demonstrated, the insights delivered by these two types of spectroscopy are richly complemented by other types of data, which—despite being somewhat classical in nature—furnish valuable insights and lend comprehensive understanding: infrared photographs, microscopy images depicting enlarged views of fine-grained structures, and visible/near-infrared reflection spectra.

Finally, in analyzing colorants in cultural properties our discussion emphasized the importance of combining experimental data with other types of knowledge—including awareness of the physical and chemical properties of colorants, understanding of the historical factors responsible for the introduction of various types of colorants, and an appreciation of the techniques by which cultural properties were created—to foster the broad multidisciplinary mindset required for a proper interpretation of measured data.

An on-site analysis in progress at the Museum of Fine Arts, Boston.

Acknowledgements

Our research has been made possible by the generous assistance of many individuals who have provided opportunities to work closely with precious cultural properties. It is thanks to these individuals that we have been able to perform non-destructive analyses to study pigments, dyes, and other materials used to colorize famous works of art, and we are grateful for their assistance. In particular, we acknowledge the following institutions for offering access to the cultural properties discussed in the text.

- Hiroshima Museum of Art
  - “Daubigny’s Garden”, oil painting (Figures 2,4)
- Naha City Museum of History
  - Japanese National Treasure: Naha-15-, Bingata-07-07, Bingata garment (Figures 5,7,16)
  - Japanese National Treasure: Naha-20-, Bingata-12-12, Bingata garment (Figures 8,14)
  - Japanese National Treasure: Naha-26-, Bingata-18-18, Bingata garment (Figure 20)
  - Japanese National Treasure: Naha-80-, Earthenware-01, Square-base candle stand with green Ryoku-Yu glaze (Figures 17,23)
  - Japanese National Treasure: Naha-77-, Lacquerware-09, Tsuikin-decorated black-lacquered wood tray (Figure 22)
- Hagi Uragami Museum
  - Katsushika Hokusai, "Thirty-Six Views of Mount Fuji" (Front views of Mount Fuji) (Figure 13)
- Asakura Shrine, Fukui Prefecture
  - Images of Rashomon (Figure 21)

References

1) Nobuyuki Kamba: Technical note on ultraviolet photography, ultraviolet fluorescent photography, and infrared photography. *Sokei Art Academy Restoration Laboratory Report*, Vol. 5, pp. 56-62 (1987) (in Japanese).

2) Susumu Shimoyama: Part 1, Scientific investigation. In: All about van Gogh's "Daubigny's Garden": An illustrated guide. Hiroshima Museum of Art and Kibi International University, pp. 16-26 (2008) (in Japanese).

3) Susumu Shimoyama: Discovering the black cat hidden beneath van Gogh's "Daubigny's Garden." *ISOTOPE NEWS*, Apr. No. 660, pp. 11-16 (Japan Radioisotope Association, 2008) (in Japanese).

4) Hiroshi Yoshida: Essay 3, "Daubigny's Garden": Partial reproduction and van Gogh's oil-painting technique. In: All about van Gogh's "Daubigny's Garden": An illustrated guide. Hiroshima Museum of Art and Kibi International University, pp. 37-41 (2008) (in Japanese).

5) Susumu Shimoyama and Hideo Matsui: Studying the historical trajectory leading to the use of Prussian blue in *ukiyo-e* prints via non-destructive analysis based on fluorescent X-rays from radio isotopes, Reports of the Reimei Research Report Meeting, Japan Atomic Energy Research Institute, pp. 440-454 (2004) (in Japanese).

6) Susumu Shimoyama, Hideo Matsui, Yasuko Shimoyama: Non-Destructive Identification of Blue Colorants in Ukiyo-e Prints by Visible-Near Infrared Reflection Spectrum Obtained with a Portable Spectrophotometer Using Fiber Optics, *Bunseki Kagaku*, **55**, pp. 121-126 (2006) (in Japanese).

7) Hideo Matsui, Susumu Shimoyama, Yasuko Shimoyama: Studying the historical trajectory leading to the use of Berlin blue and the *Thirty-Six Views of Mount Fuji* as a pioneering work establishing the genre of landscape images in *ukiyo-e* prints via non-destructive methods for identifying blue colorants in *Nishiki-e*. *Hokusai Kenkyu*, No. 37, pp. v-liv/pp. 5-54 (Tokyo Bijutsu, 2005) (in Japanese).

8) Bokashi, in Ukiyo-e Daijiten (Ukiyo-e Encyclopedia), edited by the International Ukiyo-e Society p. 445 (Tokyodo Shuppan, 2008) (in Japanese).

9) Omohan, in Ukiyo-e Daijiten (Ukiyo-e Encyclopedia), edited by the International Ukiyo-e Society p. 110 (Tokyodo Shuppan, 2008) (in Japanese).

10) Susumu Shimoyama and Yasuko Noda: Simple portable X-ray fluorescence analyzer using a low-level radioactive isotope (^{241}Am) as an X-ray source: Applications to non-destructive analysis of inorganic colorants in traditional Japanese *ema* artworks. *Bunseki Kagaku*, **49**, pp. 1015-1021 (2000) (in Japanese).

11) Izumi Nakai, editor, the Japan Society for Analytical Chemistry X-Ray Analysis Discussion Group, supervisor: X-ray fluorescence analysis in practice, 2nd edition, pp. 257-260, Appendix D: Table of characteristic X-ray energies and absorption edges, etc. (Asakura Shoten, 2016) (in Japanese).

12) Izumi Nakai, editor, the Japan Society for Analytical Chemistry X-Ray Analysis Discussion Group, supervisor: X-ray fluorescence analysis in practice, 2nd edition, Chapter 1: Foundations of fluorescent X-rays, Section 1.5.6, Fluorescent X-ray Spectra, pp. 7-9 (Asakura Shoten, 2016) (in Japanese).

13) R. J. Gettens and G. L. Stout, Painting Materials: A Short Encyclopedia, Revised Edition, translated into Japanese by Tsuneyuki Morita, pp. 153-156 (Bijutsu Shuppan-Sha, 1999).

14) B. Muhlethaler, J. Thissen: ‘Smalt’, Artists’ Pigments, A Handbook of Their History and Characteristics, Vol. 2, pp. 113-130 (© 1993 National Gallery of Art).

15) Susumu Shimoyama and Yasuko Shimoyama: Japanese National Treasures: Materials related to the Ryukyu Kingdom Sho Dynasty, Report on Non-destructive analytical investigations of craft works (including dyed fabrics), "Lacquerware-09: Tsuikin-decorated black-lacquered wood tray", *Naha City Museum of History Bulletin*, No. 1, pp. 31 (Naha City Museum of History, 2009) (in Japanese).

16) Kazumi Murose, Lacquer Culture: Inheriting a Tradition of Japanese Beauty, <Creating Lacquer Colors>, Kadokawa Selections 343, pp. 33-37 (Kadokawa Shoten, 2002) (in Japanese).

17) Noboru Terada, Kadoaki Oda, Yasushi Oyabu, Tetsu Asami, editors: Lacquer: Science and practical techniques, History of Colored Lacquer Pigments, pp. 200-211 (Riko Shuppansha, 2002) (in Japanese).

18) Holbein Industrial Technology Division, editors: Handbook of Painting Materials: Indigo-shaded Blue, pp. 59-60 (Chuokouronbijyutsu, 1991) (in Japanese).

19) Susumu Shimoyama, Koji Oshita, Yasuko Shimoyama: 2010/2011 Report on non-destructive investigation of colorants in dyed fabric artifacts related to Uzagaku costumes, Gold-inlaid green-lacquered wood tray, *Shurijo Koen Kanri Center Annual Report on Investigative Research and Programs to Promote Outreach and Awareness*, No. 3, p. 84 (Okinawa Churashima Foundation, 2013) (in Japanese).

20) Susumu Shimoyama, Koji Oshita, Yasuko Shimoyama: 2015 Report on investigation of colorants in Sho-dynasty artifacts, Square-base candle stand with green Ryoku-Yu glaze, *Shurijo Koen Kanri Center Annual Report on Investigative Research and Programs to Promote Outreach and Awareness*, No. 7, pp. 66-68 (Okinawa Churashima Foundation, 2015) (in Japanese).

21) Masataro Onishi, Pottery Glazes: Theory and Practical Recipes (Revised Edition), pp. 180-183 (Rikogakusha, 2007) (in Japanese).

22) Susumu Shimoyama and Yasuko Noda: Extinction effects of iron (II) and copper (II) ions on measured fluorescent intensities in three-dimensional fluorescence spectra of dyed fabric specimens, *Bunseki Kagaku*, **47**, pp. 295-301 (1998) (in Japanese).

23) Juuji Yoshimura, editor: Kagaku Jiten (Chemical Dictionary), Second Edition, Susumu Shimoyama, author: Natural dyes: Primary natural dyes used in traditional Japanese crafts, pp. 936-937 (Morikita Shuppan, 2009) (in Japanese).

24) Susumu Shimoyama and Yasuko Noda: Non-destructive identification of dyes used in ancient dyed-fabric artifacts from three-dimensional fluorescence spectra, *Bunseki Kagaku*, **41**, pp. 243-249 (1992) (in Japanese).

25) Susumu Simoyama and Yasuko Noda: NON-DESTRUCTIVE ANALYSIS OF UKIYO-E PRINTS Determination of Plant Dyestuffs used for Traditional Japanese Woodblock Prints, Employing a Three-Dimensional Fluorescence Spectrum Technique and Quartz Fiber Optics, *Dyes in History and Archaeology*, **15**, pp. 27-42 (1997).

26) Susumu Shimoyama, Yasuko Noda, Shinya Katsuhara: Using optical fibers to measure three-dimensional fluorescence spectra for non-destructive identification of colorants used in ancient Japanese *ukiyo-e* prints, *Bunseki Kagaku*, **47**, pp. 93-100 (1998) (in Japanese). Winner of the 1998 Analytical Chemistry Research Article award from the Japan Society for Analytical Chemistry.

27) Susumu Shimoyama: Spaulding Collection, Museum of Fine Arts, Boston, Collaborative investigation of colorants in *ukiyo-e* woodblock prints, Colorants used in works by Torii Kiyonaga (Initial Report), *Research on Information Science for Cultural Properties*, **5**, pp. 43-53 (Kibi International University Research Advancement Center for Cultural Property, 2008) (in Japanese).

28) Juuji Yoshimura, editor: Kagaku Jiten (Chemical Dictionary), Second Edition, Susumu Shimoyama, author: Three-dimensional fluorescence spectra, pp. 553-554 (Morikita Shuppan, 2009) (in Japanese).

29) Seiji Hasegawa, author, Japan Forensic Science Appraisal Center, supervisor: Scientific Forensics, pp. 24-33 (Natsume-sha, 2004) (in Japanese).

30) Analysis Laboratory of Forensic Science, supervisor: Scientific Forensics, pp. 31-46 (Shufunotomosha, 2010) (in Japanese).

31) Katsumi Kurosaka, editor: Newly revised and expanded supplement, Kokushi Taikei (Annals of Japanese History), Popular Edition, Engishiki, Volume 2, Engishiki, Scroll 14, Nuidonoryou, Zassenyoudo, pp. 400-405 (Yoshikawa Koubunkan, 1990) (in Japanese).

32) Susumu Shimoyama and Yasuko Noda: Using optical fibers to measure three-dimensional fluorescence spectra to identify dyes used to colorize fabrics for brocades in ancient China, *Bunseki Kagaku*, **46**, pp. 571-578(1997) (in Japanese).

33) Susumu Shimoyama, Yasuko Noda: Using optical fibers to measure three-dimensional fluorescence spectra to identify dyes used for ancient green dyed fabrics, *Bunseki Kagaku*, **46**, pp. 791-799 (1997) (in Japanese).

34) Susumu Simoyama and Yasuko Noda: NON-DESTRUCTIVE ANALYSIS OF DYES IN A CHINESE BROCADE: Determination of Plant Dyes in a 16th/17th-Century Textile by a Three-Dimensional Fluorescence Spectrum Technique with Fibre Optics, *Dyes in History and Archaeology*, **15**, pp. 70-84 (1997).

35) Yasuko Noda and Susumu Shimoyama: Non-Destructive Analysis Ukiyo-e, Traditional Japanese Woodblock Prints, Using a Portable X-ray Fluorescence Spectrometer, *Dyes in History and Archaeology*, **18**, pp. 73-86 (1999).

36) Yasuharu Nishikawa and Keizou Hiraki: Practical instrumental analysis series: Fluorescence and phosphorescence methods: Extinction due to paramagnetic ions, pp. 37-38 (Kyoritsu Shuppan, 1987) (in Japanese).

37) Susumu Shimoyama: Natural colorants: A new trend in coloring agents for developing makeup cosmetics. *COSMETIC STAGE*, Vol. 2, No. 4, pp. 1-7 (Technical Information Institute, 2008) (in Japanese).

38) Kazuhisa Ono, Naoko Watanabe, Shigenori Kumagai, Susumu Shimoyama, Yasuko Noda: Cosmetic ingredient, Open patent, Public application number 8-059427 (Shiseido, Den Material, 1996) (in Japanese).

39) Naoki Moritaka, Masao Oinuma, Susumu Shimoyama: Natural colorant-processed powder and cosmetic ingredient based thereon, Open patent, Public application number 2000-044828 (Den Material, Chifure, 2000) (in Japanese).

Visualization of the Photodegradation of a Therapeutic Drug by EEM-PARAFAC

Shinichiro Kamino
PhD
Professor
Laboratory of Bioorganic Chemistry
School of Pharmacy
Aichi Gakuin University

1. Introduction

Because therapeutic drugs incorporate organic compounds with many different structures, they are often susceptible to transformations induced by light or other external factors. In addition to promoting discoloration that can degrade drug effectiveness or quality of life, these transformations may create decomposition products that cause side effects or otherwise prevent drugs from delivering appropriate therapeutic benefits.

The photostability of drug substances and formulations is characterized by conducting experimental tests in accordance with Stability Testing: Photostability Testing of New Drug Substances and Products ratified by the International Council for Harmonisation of Technical Requirements for Pharmaceuticals for Human Use (ICH), a collaboration between the U.S., the E.U., and Japan. The data required for these tests may be acquired via a wide variety of analytical methods, including high-performance liquid chromatography (HPLC) and gas chromatography-mass spectrometry (GC-MS); although these methods play important roles, they cannot be easily used to visualize the temporal evolution of degradation processes.

Fluorescent fingerprints, also known as *excitation-emission matrices* (EEMs), are three-dimensional contour maps in which fluorescent intensity is plotted vs. excitation wavelength and fluorescent wavelength, yielding graphical signatures—resembling human fingerprints—that are characteristic of specific substances. Combining this measurement strategy with the method of multivariate analysis known as *parallel factor analysis* (PARAFAC) yields EEM-PARAFAC, a chemometric technique capable of analyzing EEMs—which are superpositions of spectral contributions from multiple component substances—to separate and identify the signatures of each individual component.1) Despite impressive progress in applications of this technique for purposes such as water-quality monitoring and quality control for agricultural products and foodstuffs,2-7) to date there have been almost no attempts to use EEM-PARAFAC for assessing pharmaceutical stability.8) In this paper, motivated by the goal of visualizing the photodegradation of pharmaceutical substances, we develop a new technique for characterizing photostability via EEM-PARAFAC analysis.9)

2. Absorption and Fluorescence Spectra of a Phenothiazine-based Antipsychotic

We began by using EEM-PARAFAC analysis to study the photodegradation of chlorpromazine hydrochloride (CPZHCl), a phenothiazine-based antipsychotic known to exhibit poor photostability. As a first step, we assessed the linearity of the relationship between the fluorescence intensity and the CPZHCl concentration in a methanol solution; our results indicated that this relationship was indeed highly linear over the concentration range 5-25 µM. We next prepared a 10 µM solution of CPZHCl in methanol, irradiated this solution with 365 nm light from an LED source, and measured the temporal evolution of the absorption and fluorescence spectra at 25°C under an oxygen environment (Figure 1). CPZHCl exhibits absorption bands in the ultraviolet region, with density functional theory calculations indicating that the absorption band near 260 nm is due to π-π* transitions in phenothiazine rings, while the weak absorption band near 310 nm is due to n-π* transitions in sulfur atoms. A blue fluorescence peak is also observed near 450 nm. Under irradiation by LED light, the shape of the absorption band changes—with a long-wavelength tail emerging—and the visual appearance of the solution changes from colorless to orange-colored. The fluorescence spectrum is also significantly blueshifted, with the peak wavelength decreasing to around 375 nm. Repeating the experiment for solutions prepared with different solvents (dichloromethane, acetonitrile, dimethylformamide, water) yielded nearly identical shifts in the absorption and fluorescence spectra under photoirradiation.

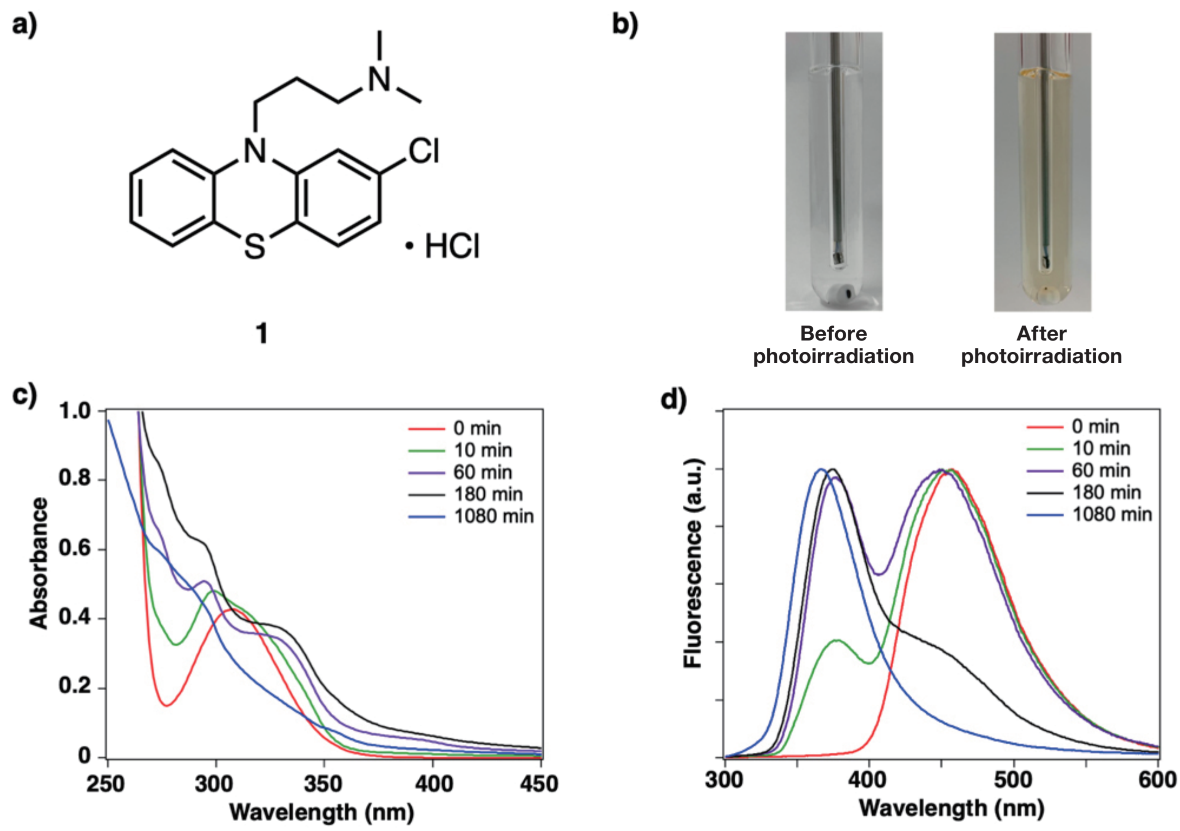

Fig. 1
a) Structure of chlorpromazine hydrochloride (CPZHCl).
b) Under photoirradiation, CPZHCl solution changes from colorless, transparent liquid to orange-colored liquid.
c,d) Temporal variation in absorption (c) and fluorescence (d) spectra of CPZHCl methanol solution. Time is measured from the start of photoirradiation.

3. EEM-PARAFAC Analysis

We next used EEMs to monitor the temporal progression of CPZHCl photodegradation in a methanol solution. Under sustained photoirradiation, the contour map of fluorescence intensity for CPZHCl—which is originally concentrated near a wavelength of em≈450 nm and excitation wavelengths of ex≈{260,310} nm—transforms into a new contour map concentrated in the ranges em≈300-450 nm and ex≈200-350 nm. Applying PARAFAC analysis to separate the spectrum into three components (C1, C2, C3) as shown in Figure 2, we find that the C1 spectrum initially exhibits peaks at (em,ex)≈(450,{260,310}) nm, but after 30 min of photoirradiation, these peaks have weakened, while new peaks have emerged in the C2 spectrum near (em,ex)≈(375,{250,275,335}) nm and in the C3 spectrum near (em,ex)≈(355,{240,290}) nm. Note that the C3 spectrum emerges more slowly than the C2 spectrum. For this EEM-PARAFAC model, the core consistency (a benchmark indicating whether or not the number of components was chosen correctly) was 91%.

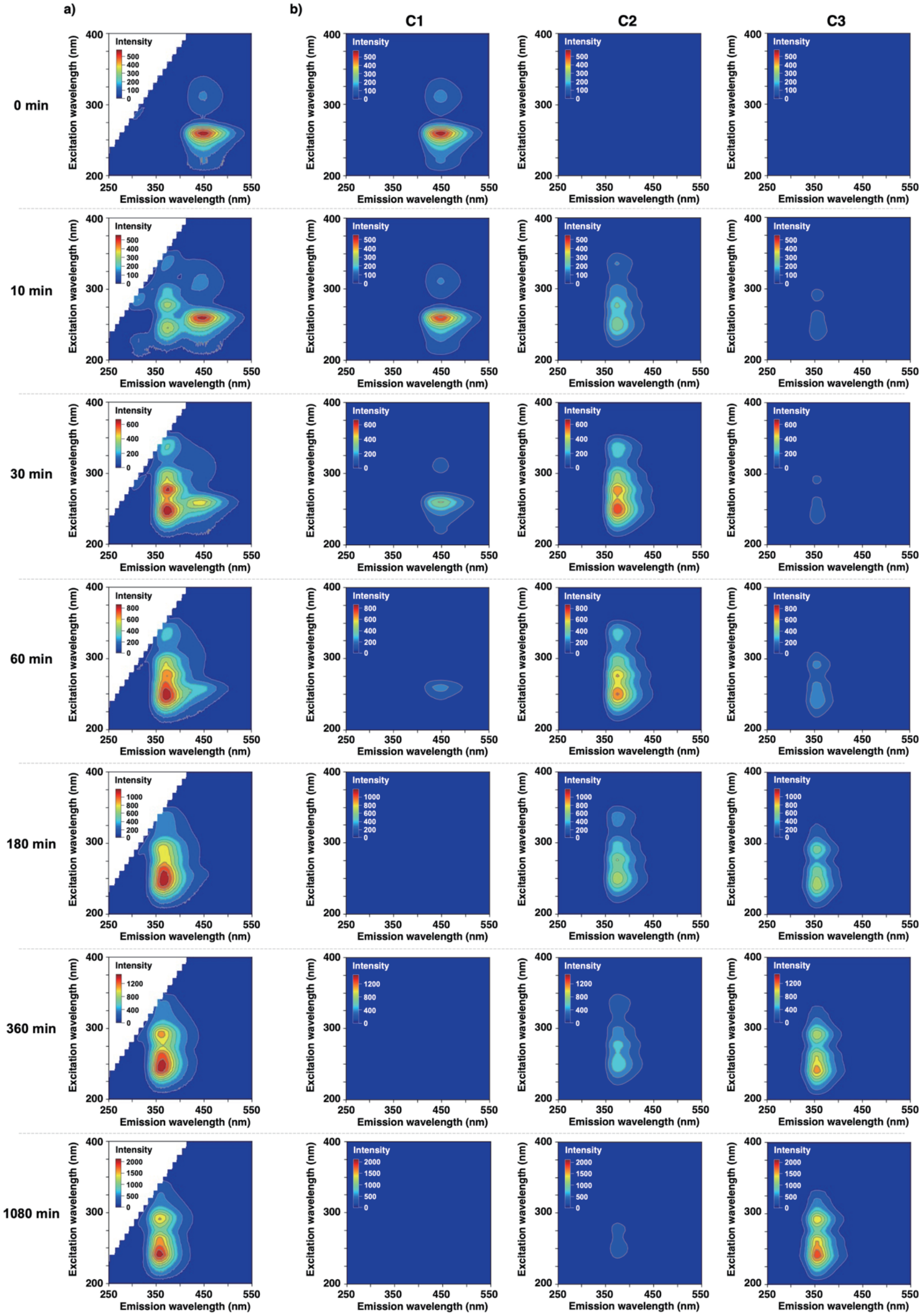

Fig. 2
a) Temporal variation in EEM spectrum of CPZHCl methanol solution under photoirradiation. Time is measured from the start of photoirradiation.
b) Results of PARAFAC analysis. For this model, the assumption of three independent components yielded a successful separation result.

4. Identification of Photodegradation Products and Kinetic-theory Analysis of Photodegradation Reactions

As a further validation of the correctness of the number of components chosen for our EEM-PARAFAC separation analysis, we next identified the reaction products generated by CPZHCl photodegradation and studied the chemical structures and EEM spectra of these substances. We first exposed a 10 mM ethanol solution of CPZHCl to 365 nm light from an LED source for 18 h under an oxygen environment, and then used silica-gel chromatography to separate and refine the resulting mixture of reaction products. This analysis shows that the primary reaction product is phenothiazine hydrochloride sulfoxide (PHS) produced by oxidation of CPZHCl, and single-crystal X-ray structure analysis successfully determined the crystal structure of this PHS. Next, we used nuclear magnetic resonance spectroscopy to determine the structure of the secondary reaction product 2-chloro-*N*,*N*-dimethylcarbazole (2CNND). Our analysis found trace quantities of oxide reaction products corresponding to the molecular formulas $C_{17}H_{19}ClN_2SO$ and $C_{17}H_{19}ClN_2SO_3$.

Our next step was to prepare methanol solutions of the photodegradation products PHS and 2CNND, measure their EEM spectra, and compare the results to the C2 and C3 spectra obtained via PARAFAC component-separation analysis. The results, shown in Figure 3, indicate that the contour map for PHS exhibits peaks near (em,ex)≈(375,{275,335}) nm—matching the C2 spectrum in Figure 2—while the contour map for 2CNND exhibits peaks near (em,ex)≈(355,{240,265,290}) nm, matching the C3 spectrum in Figure 3. These results confirm the success of our EEM-PARAFAC analysis based on a three-component model.

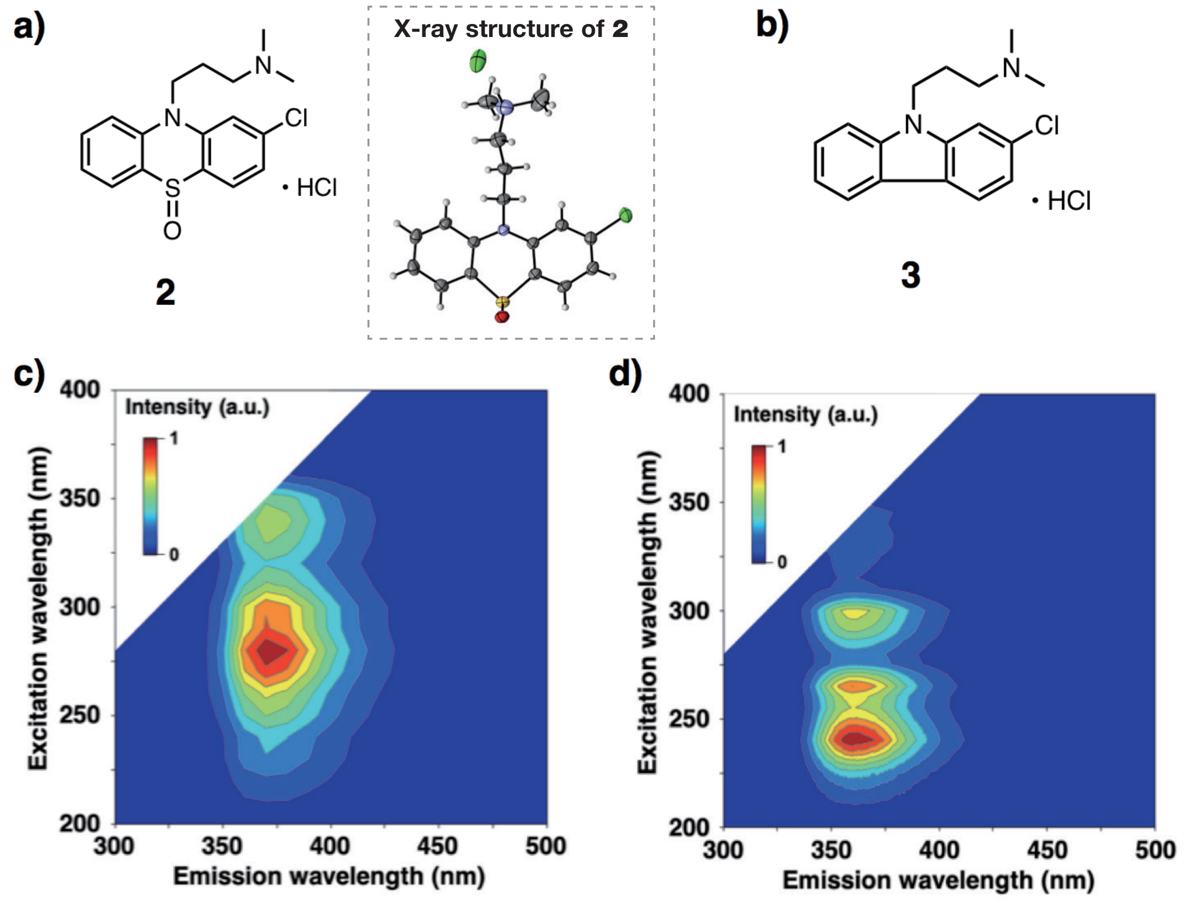

Fig. 3
a) Chemical structure of phenothiazine hydrochloride sulfoxide (PHS).
b) Chemical structure of 2-chloro-*N*,*N*-dimethylcarbazole (2CNND).
c) EEM spectrum of methanol solution of PHS.
d) EEM spectrum of methanol solution of 2CNND.

Finally, we conducted a kinetic-theory based analysis to yield quantitative insight into the photodegradation reaction of CPZHCl. We use the notation $[\mathrm{CPZHCl}]_0$ to denote the initial concentration of CPZHCl, the symbol t to denote the light-irradiation time in minutes, and the symbol I to denote the fluorescence intensity for the C1 spectrum at (em,ex)=(450,260) nm. We also denote by $Q_{\mathrm{em}}(t)$ the fractional decrease in this intensity after time t; $Q_{\mathrm{em}}(t)$ is computed from the initial intensity (I_0) and the intensity after time $t(I_t)$ via Equation (1). Multiplying $[\mathrm{CPZHCl}]_0$ by $Q_{\mathrm{em}}(t)$ then gives the concentration of CPZHCl remaining after t min of photoirradiation.

$$\mathrm{Q_{em}} = \frac{\mathrm{I_0} - \mathrm{I_t}}{\mathrm{I_0}} \quad (1)$$

Figure 4 plots the decrease in CPZHCl concentration vs. the light-irradiation time; from this profile, we conclude that the degradation of CPZHCl proceeds via a first-order reaction. Using a Matplotlib implementation of the Levenberg-Marquardt method of nonlinear fitting, we fit the data in Figure 4 using the function in Equation (2); this yields a value of $k_1 = 8.7\times10^{-3}$ min^{-1} for the reaction-rate constant, corresponding to a half-life ($t_{1/2}$) of 80 min for the photodegradation reaction.

$$[\mathbf{1}] = [\mathbf{1}]_0 e^{-k_1 t} \quad (2)$$

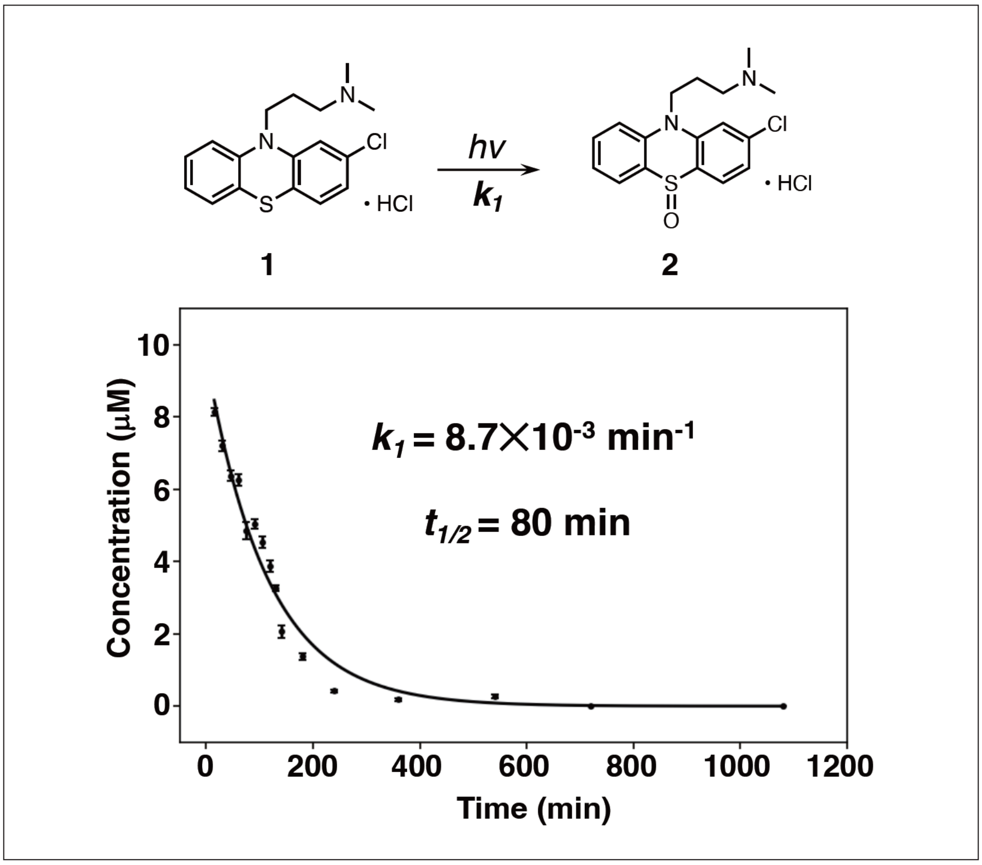

Fig. 4 Kinetic-theory based analysis of photodegradation of CPZHCl.

5. Characterizing Photostability of Phenothiazine-based Antipsychotics

As a final demonstration of the efficacy of the methods described in this paper, we performed an EEM-PARAFAC analysis to characterize the photostability of two phenothiazine-based antipsychotics with differing side chains: levomepromazine maleate (LM) and prochlorperazine maleate (PM). We observed no significant differences between these compounds in the progress of photodegradation; in both cases, the peaks in the spectrum of the drug substance (C1) vanished quickly after the onset of photoirradiation, with new peaks gradually emerging in the spectra for sulfoxide (C2) and carbazole (C3)—thus demonstrating successful visualization of the temporal evolution of photodegradation. By determining the relative concentrations of the three components and observing the temporal evolution of the concentration distribution, we found that over 50% of the drug substance had decomposed after 10 min of photoirradiation. Our analysis also shows that the carbazole reaction product emerged more slowly than the sulfoxide reaction product; however, after 180 min of irradiation, carbazole accounted for 55% of the concentration distribution (Figure 5).

These results demonstrate the efficacy of EEM-PARAFAC analysis for characterizing the photostability of phenothiazine-based antipsychotics. Our approach allows the photodegradation of drug substances to be visualized in the form of contour maps. Compared to methods such as HPLC or GC-MS, it has the advantage of providing quantitative insights into drug substance photodegradation with no need for component separation via column chromatography—and requires significantly smaller quantities of drug substance samples, solvents, and other consumables.

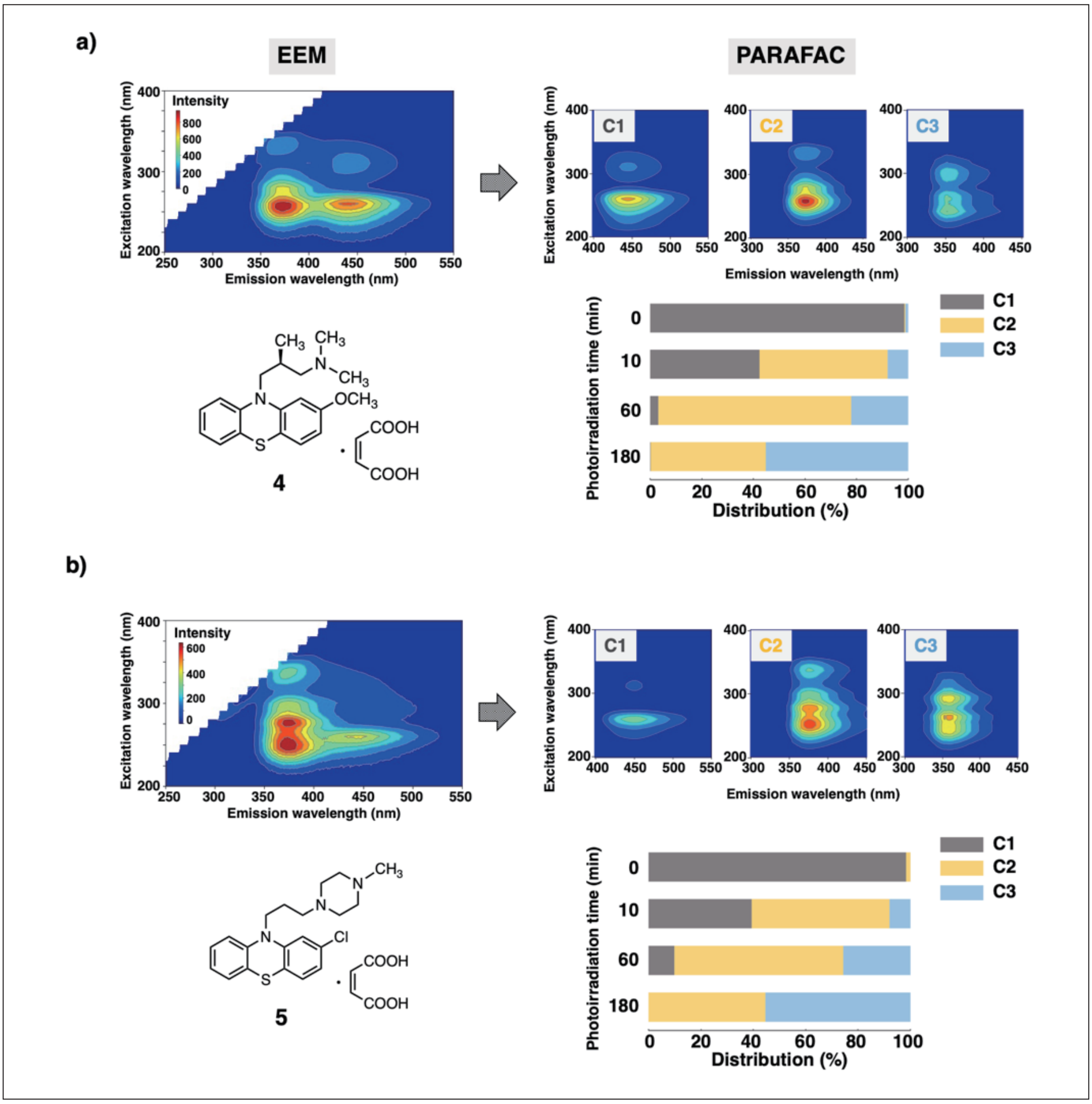

Fig. 5
a) Photostability of levomepromazine maleate (LM)
b) Photostability of prochlorperazine maleate (PM)

6. Conclusions

The data required to characterize the photostability of drug substances and formulations may be acquired via a wide variety of analytical methods. Although these methods play important roles, they cannot be easily used to visualize the temporal evolution of degradation processes. In this paper we presented a new method we have developed for analyzing the photostability of pharmaceuticals via EEM-PARAFAC analysis. Our method allows visualization, via mapping, of the temporal progression of photodegradation of drug substances, and can also compute relative concentrations of individual components based on intensity values and a kinetic-theory based analysis of photodegradation reactions, thus yielding quantitative information on degradation processes.

Pharmacists and other health-care professionals often work with drugs that may be unstable under light exposure. These professionals should have information beforehand to appropriately handle light-sensitive drug substances to ensure that quality is preserved at all stages of the therapeutic process, from drug storage, the preparation of drug formulations, through to the administration of drug therapies. For example, the phenothiazine-based antipsychotic studied in this work is packaged with a package insert specifying appropriate usage guidelines and precautions, such as: **After opening the package, store this drug in a dark place to avoid degradation and discoloration due to light exposure. Do not use this drug if it appears to have changed color.** Our EEM-PARAFAC analysis also revealed that the primary reaction product resulting from the photodegradation of this drug was a transparent, colorless oxide.

The external appearance of pharmaceuticals—their color and shape—is easily judged by visual inspection and thus constitutes a useful benchmark for checking drug stability; nonetheless, proper administration of drug therapies requires accurate identification of degradation pathways and degradation products. The ability of EEM-PARAFAC to furnish such insights quickly and easily will make this technique a powerful tool—and a promising platform for practical implementations of regulatory science for quality control of pharmaceuticals and other products.

References

1) K. R. Murphy, C. A. Stedmon, D. Graebera and R. Bro, *Anal. Methods* 2013, **5**, 6557-6566.

2) X. Wang and F. Zhang, *Sci. Rep.* 2018, **8**, 1-13.

3) I. Duran Meras, J. Dominguez Manzano, D. Airado Rodriguez and A. Munoz de la Pena, *Talanta* 2018, **178**, 751-762.

3) M. Sgroi, P. Roccaro, G. V. Korshin and F. G. A.Vagliasindi, Environ. *Sci. Technol*. 2017, **51**, 4306-4316.

5) L. Lenhardt, I. Zekovic, T. Dramicanin, B. Milicevic, J. Burojevic and M. D. Dram-icanin, *Food Chem*. 2017, **229**, 165-171.

6) V. Trivittayasil, M. Tsuta, Y. Imamura, T. Sato, Y. Otagiri, A. Obata, H. Otomo, M. Kokawa, J. Sugiyama, K. Fujita and M.Yoshimura, *J. Sci. Food Agric*. 2016, **96**, 1167-1174.

7) C. Coelho, A. Aron, C. Roullier-Gall, M. Gonsior, P. Schmitt-Kopplin and R. D. Gougeon, *Anal. Chem*. (Washington, DC, U. S.) 2015, **87**, 8132-8137.

8) I. Sciscenko, H. Thi My Hang, C. Escudero-Onate, I. Oller and A. Arques, *ACS Omega* 2021, **6**, 4663-4671.

9) M. Tanioka, T. Ebihana, M. Uraguchi, H. Shoji, Y. Nakamura, R. Ueda, S. Ogura, Y. Wakiya, T. Obata, T. Ida, J. Horigome and S. Kamino, *RSC Advances* 2022, **12**, 20714-20720.

SCIENTIFIC INSTRUMENT NEWS 2024 Vol. 21 MARCH
Technical magazine of Electron Microscope and Analytical Instruments. Article

Effect of Alcohol Content on the Ionomer Adsorption of Polymer Electrolyte Membrane Fuel Cell Catalysts

Tsuyohiko Fujigaya
PhD
Professor
Department of Applied Chemistry
Kyushu University

1. Introduction

Polymer electrolyte membrane fuel cells (PEMFCs), which use hydrogen as a source of energy, are widely expected to furnish crucial power sources for future sustainable low-carbon societies.[1,2] Reducing the cost of PEMFCs is a key prerequisite for ensuring their growth, and one particularly urgent challenge—with particularly significant cost-reducing potential—is to establish techniques for minimizing the platinum content of catalyst layers in these devices. One natural first step in this direction is to increase platinum utilization efficiency, and this approach has been pursued in many previous studies.[2-5] Catalyst layers typically have 3-dimensional porous structures comprising carbon-supported platinum nanoparticles (Pt/C) and proton-conductive polymers (*ionomers*).[6] The rate-limiting step in the basic battery reaction is the *oxygen-reduction reaction* (ORR) occurring at the cathode catalyst layer, in which protons and electrons generated at the anode react at platinum nanoparticle sites with oxygen gas supplied from the exterior to produce water. The diffusion of protons and of oxygen is governed by the structure of the catalyst layer—specifically, by the connectivity of the pores (or *voids*) and the ionomer distribution—and can give rise to ORR overvoltages; for this reason, careful control of the structure of catalyst layers, and cathode catalyst layers in particular, is essential.[7] Achieving catalyst structures that effectively exploit proton and oxygen diffusion requires careful fine-tuning[8] of various details—including optimizing the composition of the catalyst solution (known as *ink* and containing Pt/C, ionomers, and dispersing agents) and perfecting the battery assembly process—and, although there do exist certain protocols that have been recommended for standardization, one suspects that each individual research group and manufacturer has developed its own idiosyncratic and zealously-guarded set of procedures.

The ease of controlling the relative abundance of ionomers in the ink (measured by the ratio of ionomers to carbon, I/C) has made this parameter a common target of optimization efforts.[9-18] The basic tradeoff is that reducing I/C tends to increase oxygen diffusivity, but reduces proton conductivity by closing off proton-conduction pathways.[10] The solvent used for the ink is also known to affect PEMFC performance and has been extensively studied, with most research focusing on two-component solvents combining water with alcohols such as methanol, ethanol, or 2-propanol.[19-31]

The blend ratio of alcohol and water in such solvents has been the focus of several studies. Van Cleve *et al.* reported that water-rich ink (83 wt% water) decreased ORR activity due to strong interactions between Pt and the sulfonic acid in ionomers, while water-poor ink (24 wt% water) led to the formation of large ionomer aggregates that obstructed oxygen diffusion in catalyst layers; these authors concluded that PEMFC performance was optimized by ink made with a solvent of intermediate water content (62 wt% water).[30] This finding was contradicted by Orfanidi *et al.*, who reported higher performance for a water-poor (16 wt%) ink than for a relatively water-rich (65 wt%) ink, and interpreted this result as follows: whereas ionomer aggregates formed in water-rich inks obstruct voids in catalyst layers thereby obstructing oxygen diffusion, water-poor (i.e. alcohol-rich) inks yield greater uniformity in the distribution of ionomers, resulting in the formation of contiguous proton-conduction pathways on Pt surfaces that ensure good performance.[29] These studies demonstrate that interactions between carbon surfaces and ionomers and solvent molecules in ink solutions are key factors governing the distribution of ionomers and the contiguity of void regions in catalyst layers.

However, to date there has been no systematic quantitative analysis of the impact of solvent composition on adsorption between ionomers and catalysts.

In this study, we measure adsorption isotherms to characterize ionomer adsorption behavior—both on carbon carriers and on Pt/C—in inks made with two aqueous ethanol solutions: one with high water content (80 wt% water, which we term the *water-rich* solvent) and one with low water content (13 wt% water, which we term the *alcohol-rich* solvent). We then assemble fuel cells with catalyst layers made from these two inks and compare their battery performance.

2. Results and Discussion

The ionomer we use is Nafion, the most widely-used PFSA (perfluorosulfonic acid, a polymer based on fluorinated polyethylene) offering excellent proton conductivity.[32)] The carbon source we use is Vulcan (CB), also a common choice. Figure 1 shows adsorption isotherms quantifying the adsorption of Nafion on CB for both water-rich (blue curves) and alcohol-rich (black curves) solvents. Adsorption of Nafion was characterized by ^{19}F-NMR, which offers higher quantitative accuracy than mass-based methods[33)] or density measurements.[34)] Although in this study we consider alcohol/water blended solvents, 19F-NMR measurements of Nafion adsorption isotherms have also been reported for ink made with water alone as a solvent.[35-37)] Plots of adsorption vs. equilibrium Nafion concentration (Ce) show a 2-step profile for both water-rich and alcohol-rich solvents; this indicates multilayer adsorption, as is also seen with pure-water solvents.[35-38)] The chemical structure of the CB surface is non-uniform, and theory suggests that adsorption on such non-uniform surfaces should not be well described by the Langmuir model; nonetheless, fitting to a Langmuir profile yields R^2 values above 0.95, suggesting good statistical significance. Using these Langmuir fits to compute equilibrium adsorption constants (K_L) for first-layer adsorption of Nafion on CB yields a higher value for the water-rich solvent (K_L=89) than for the alcohol-rich solvent (K_L=32), indicating stronger interactions in the water-rich case. The maximum adsorption capacity (Γ_{max}) for first-layer adsorption is also larger for the water-rich solvent (Γ_{max}=0.043 mg/mg) than for the alcohol-rich solvent (Γ_{max}=0.024 mg/mg), indicating that the water-rich solvent not only yields stronger interactions but is also beneficial for adsorption (Table 1). We interpret this result as follows: In the water-rich solvent, hydrophobic CF_2 primary chains are preferentially adsorbed on CB surfaces due to hydrophobic interactions; in the alcohol-rich solvent, by contrast, Nafion is solvated by alcohol molecules, preventing adsorption from proceeding effectively. One interesting observation is that first-layer adsorption begins at a concentration near Ce≈0.04 mg/mL in the water-rich solvent, but at a lower concentration near Ce≈0.02 mg/mL in the alcohol-rich solvent. It is known[39-40)] that, in water-rich solvents, Nafion forms bundles due to strong hydrophobic interactions between CF_2 primary chains, while in alcohol-rich solvents the behavior more closely resembles individual dissolution due to solvation on CF_2 primary chains caused by alcohol molecules; the decrease in apparent concentration we observe for the water-rich solvent suggests that such a reversal phenomenon may be occurring here as well. It is remarkable that adsorption-isotherm measurements alone suffice to illuminate such a wide variety of curious phenomena. These observations suggest that the large value of Γ_{max} observed for the water-rich solvent reflects not only strong adsorption forces but also the formation of Nafion bundles.

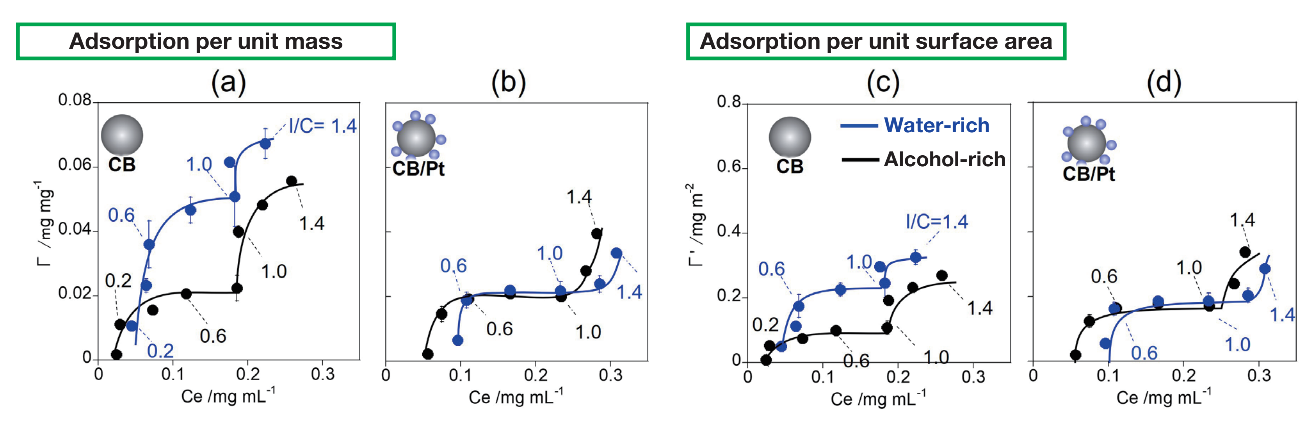

Fig. 1 Adsorption isotherms for Nafion on CB (a,c) and for Nafion on CB/Pt (b,d). Plots (a) and (b) show adsorption per unit mass, while plots (c) and (d) show adsorption per unit surface area. Blue and black curves respectively denote results for water-rich and alcohol-rich solvents.

Table 1 Plots of K_L, Γ_{max}, and Γ'_{max} for Nafion absorption on CB and CB/Pt.

	CB		CB/Pt	
	Water-rich	Alcohol-rich	Water-rich	Alcohol-rich
K_L	89	32	29	25
Γ_{max} [mg/mg]	0.043	0.024	0.022	0.021
Γ'_{max} [mg/m^2]	0.209	0.116	0.188	0.179

We also analyzed Nafion adsorption behavior for CB-supported Pt (CB/Pt, platinum/support ratio 46 wt%), and the results are shown in Figure 1(b). For this case we obtained values of K_L=29 and K_L=25 respectively for the water-rich and alcohol-rich solvents, considerably lower than the values for CB (Table 1). This demonstrates that, irrespective of solvent alcohol content, interactions between Nafion and Pt surfaces are weaker than interactions between Nafion and CB surfaces.[38)] Similarly, Γ_{max} values for CB/Pt are lower than those for CB, with the decrease being particularly prominent for the water-rich solvent (Figure 1(b)).

When working with Pt, a heavy atom, one must account for the possibility that adsorption may be underestimated. To address this possibility, we augment our comparison of Γ (adsorption per unit mass) by additionally comparing adsorption per unit surface area, which we denote Γ'. The quantity Γ' has units of mg/m^2 and is normalized by the BET surface area (m^2/g) as determined from nitrogen adsorption measurements. Comparing Γ' values for the water-rich solvent, we find Γ'_{max}=0.209 mg/m^2 for CB and Γ'_{max}=0.188 mg/m^2 for CB/Pt, a trend similar to that observed for Γ values. This suggests that, in the water-rich solvent, Nafion is preferentially adsorbed on CB surfaces rather than Pt surfaces. In contrast, for the alcohol-rich solvent we find values of Γ'_{max}=0.179 mg/m^2 for CB/Pt and Γ'_{max}=0.116 mg/m^2 for CB, indicating that, under alcohol-rich conditions, Nafion is preferentially adsorbed on Pt surfaces.

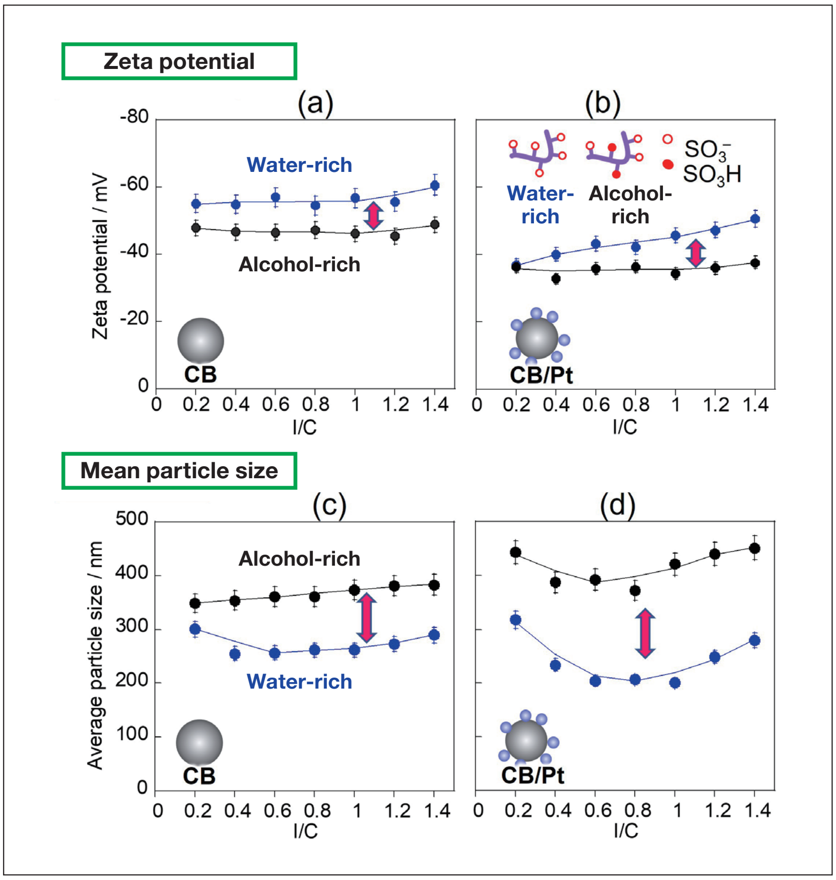

Fig. 2 *Upper graphs*: Zeta potentials for CB (a) and for CB/Pt (b) in water-rich (blue curves) and alcohol-rich (black curves) solvents.
Lower graphs: Mean particle size for CB (c) and for CB/Pt (d) in water-rich (blue curves) and alcohol-rich (black curves) solvents.

As noted above, measurements of adsorption isotherms demonstrate that Nafion adsorption increases as I/C increases. To investigate how these variations affect the diffusivity of CB and CB/Pt, we used the same inks prepared for adsorption measurements to investigate zeta potentials, particle-size distributions, and diffusion stability. In the absence of Nafion (I/C=0), the aggregation and sedimentation of particles proceeds instantaneously, complicating the measurement of the zeta potential and particle size; this clearly demonstrates the key role played by Nafion in governing diffusion phenomena. On the other hand, as shown in Figure 2(a,b), for I/C > 0.2 the zeta potential is negative, indicating the onset of stable colloidal diffusion due to the impact of sulfonic-acid groups, which acquire a negative charge through ionization. Zeta-potential values are roughly constant independent of I/C, a finding we interpret as follows: At CB and CB/Pt surfaces, there exists not only a surface-adsorbed Nafion layer, but also an additional weakly-bound Nafion layer encompassing the surface-adsorption layer. Whereas adsorption isotherm measurements assume only the presence of the surface-adsorption layer, zeta-potential measurements also reflect the impact of the weakly-adsorbed Nafion surface layer surrounding it. The larger absolute value of the zeta potential observed for the water-rich solvent reflects greater ionization of sulfonic-acid groups due to higher dielectric permittivity.21) Meanwhile, for both solvents, the absolute value of the zeta potential for CB/Pt is lower than that for CB (Figure 2(b)); we explain this by noting that, in the presence of Pt, the net negative charge of sulfonic-acid groups decreases due to interaction with Pt surfaces.

We next use dynamic scattered-light intensity analysis to measure mean particle sizes for CB (Figure 2(c)) and CB/Pt (Figure 2(d)) in the water-rich (blue curves) and alcohol-rich (black curves) solvents. For both CB and CB/Pt, the mean particle size is smaller and the particle-size distribution is narrower for the water-rich solvent than for the alcohol-rich solvent. This is due to the high particle diffusivity for the water-rich solvent, which in turn results from strong Nafion adsorption and high charge produced by the ionization of sulfonic-acid groups. On the other hand, for the alcohol-rich solvent, and particularly for CB/Pt, the diffusivity is lower, and there exist large particles with sizes above 1.0 μm.

To observe the stability of diffusion behavior, we conducted ink sedimentation experiments over a 14-day period. For CB/Pt ink, the diffusion state remained stable for the water-rich solvent (Figure 3, left), but for the alcohol-rich solvent we observed significant aggregation and sedimentation (Figure 3, right). For the water-rich solvent, Nafion adsorption and the ionization of sulfonic-acid groups give rise to a zeta potential whose absolute value approaches 50 mV, the value considered a benchmark indicator of stable diffusion.41) For the alcohol-rich solvent, by contrast, the effects of ionomer adsorption and sulfonic-acid-group ionization are insufficient to raise the absolute zeta-potential above a relatively small value, resulting in significant aggregation (Figure 4).

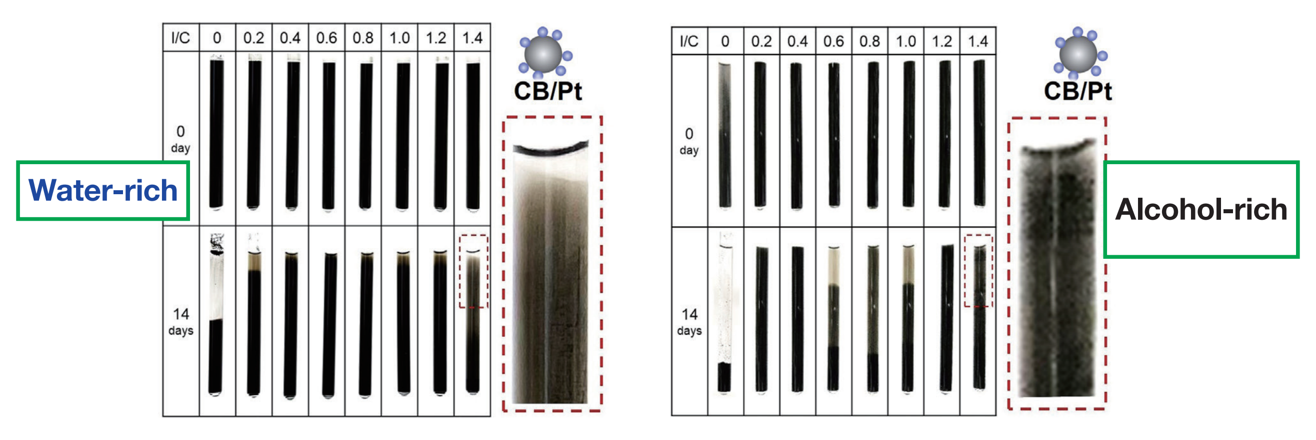

Fig. 3 CB/Pt ink sedimentation tests for water-rich (left) and alcohol-rich (right) solvents.

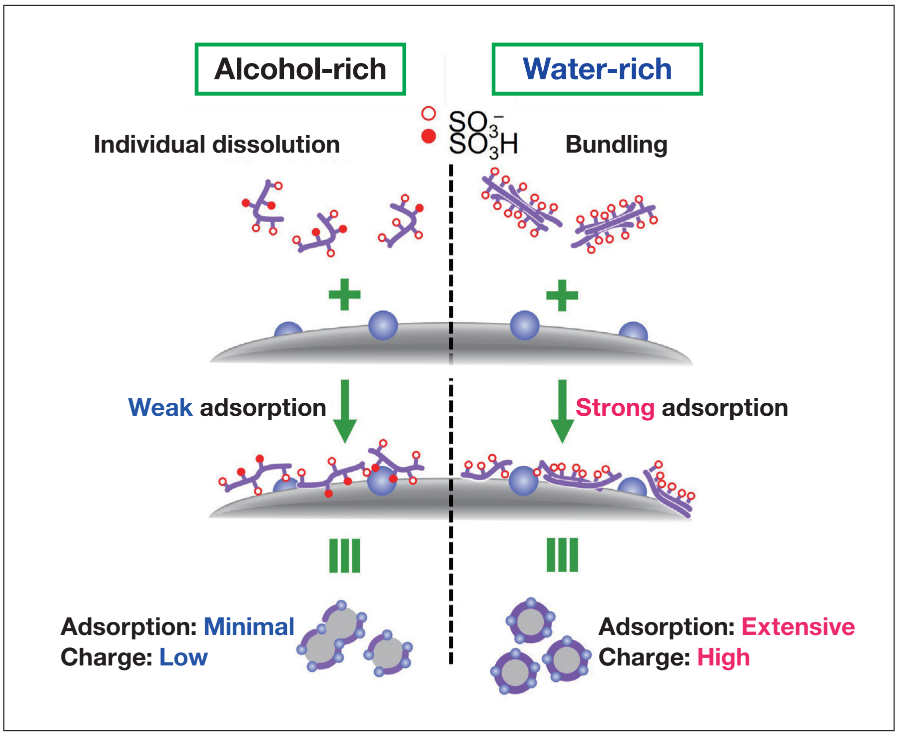

Fig. 4 Conceptual illustration of Nafion adsorption on CB/Pt in alcohol-rich (left) and water-rich (right) solvents.

Table 2 Zeta potentials for catalyst-layer surfaces.

I/C	Water-rich	Alcohol-rich
0.6	-8.3 ± 0.9	-3.3 ± 1.2
1.0	-10.7 ± 0.3	-4.5 ± 0.3

To investigate how the quantity and ionization state of sulfonic-acid groups on catalyst surfaces in inks are reflected in actual catalyst layers, we coated PET substrates with inks made using water-rich and alcohol-rich solvents (with I/C values of 0.6 and 1.0) and measured the zeta potential for the catalyst-layer surfaces. For I/C values of 0.6 and 1.0, the surface zeta potential for the ink-sprayed catalyst layers was –8.3 and –10.7 mV, respectively, for the water-rich solvent and –3.3 and –4.5 mV, respectively, for the alcohol-rich solvent (Table 2). As these zeta-potential measurements were all conducted in a water medium, the ionization state of sulfonic-acid groups was identical in all cases, and thus differences in measured values reflect the quantity of sulfonic-acid groups present at catalyst-layer surfaces. Thus we conclude that ionomer volumes are greater at catalyst-layer surfaces prepared from water-rich solvents. We explain this as follows: In water-rich solvents, ionomers adhere strongly to catalyst surfaces and remain adsorbed on these surfaces even after drying, whereas ionomer adsorption is weaker in alcohol-rich solvents, resulting in fewer residual sulfonic-acid groups. But where do ionomers *go* in alcohol-rich solvents? We suggest that that capillary forces cause ionomers to remain at deeper positions, where they serve to obstruct void regions between CB/Pt aggregates after drying.

To investigate how the different Nafion-adsorption behavior observed for water-rich and alcohol-rich solvents affects PEMFC performance, we prepared membrane electrode assemblies (MEAs) containing electrode catalyst layers (Pt content: 0.3 mg/cm^2) coated with inks (solid proportion 6 wt%) made with the two types of solvents. In preparing these inks we chose a value of I/C=0.72, in the concentration range corresponding to first-layer adsorption of Nafion.42) We respectively refer to the MEAs made with the water-rich and the alcohol-rich solvents as the w-MEA and the a-MEA. Fig. 5(a-f) shows scanning-electron microscopy images (acquired using an SU9000 SEM system) of catalyst-layer surfaces. We first note that, for both solvents, the catalyst-layer surfaces exhibit uniform structures with no major cracks. Interestingly, low-magnification observations of the w-MEA reveal a uniform distribution of voids with diameters on the order of 1-2 µm (Figures 5(a,b)). The template for the formation of this micron-scale void structure was most likely furnished by water droplets.26) In contrast, no similar structure is observed for the a-MEA.

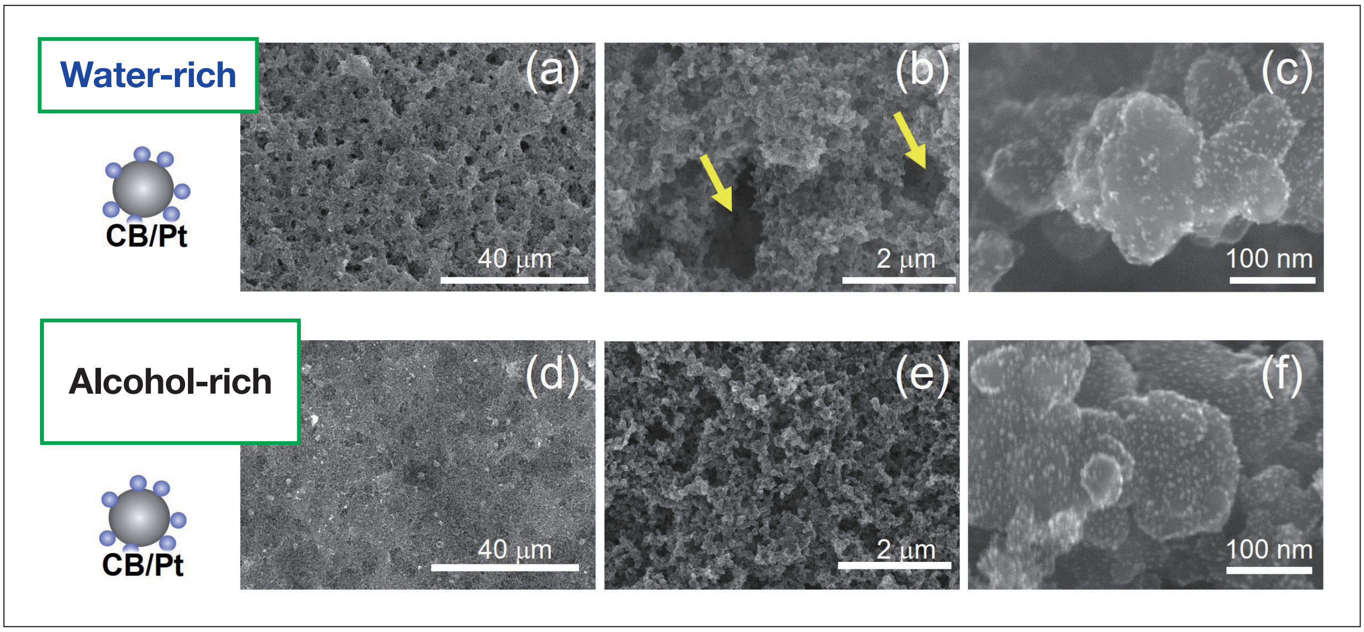

Fig. 5 SEM images of catalyst-layer surfaces in w-MEA (a-c) and a-MEA (d-f). Magnification: 1,300× (a,d); 20,000× (b,e); 300,000× (c,f).

Figure 6(a) shows polarization (*I-V*) curves for the w-MEA and a-MEA with hydrogen supplied to the anode and air supplied to the cathode (measured at 80°C and relative humidity 100%). The voltage is higher for the w-MEA (blue) than for the a-MEA (black) across the entire range of current densities, with maximum output densities of 750 mW/cm^2 for the w-MEA and 580 mW/cm^2 for the a-MEA. From AC impedance analysis of these MEAs we find that the proton resistivity of the w-MEA (0.35 Ω /cm) is lower than that for the a-MEA (1.26 Ω /cm); thus the catalyst-layer structure of the w-MEA is more conducive to proton diffusion, offering one reason for its greater activity. Figure 6(b) shows cyclic voltammograms measured for the w-MEA and a-MEA with the cathode and anode respectively subjected to flows of N_2 and H_2. Based on electrochemically-active surface-area (ECSA) analysis of the hydrogen adsorption/desorption peaks clearly visible in the range 0.1-0.3 V, we determine that the electrochemically accessible Pt surface area is 75.1 m^2/g Pt for the w-MEA and 49.3 m^2/g Pt for the a-MEA. We attribute the favorable proton-diffusion behavior and larger ECSA observed for the w-MEA to the formation of well-developed ionomer networks stimulating proton transport to the Pt surface. Our adsorption-isotherm measurements clearly showed that Nafion is preferentially adsorbed on CB/Pt surfaces in water-rich solvents, a fact that is surely relevant for the formation of proton-conduction pathways (Figure 7, left). In alcohol-rich solvents, by contrast, Nafion resists adsorption on CB/Pt, and, when catalyst layers are coated in ink, the formation of aggregates in secondary pore regions results in a non-uniform ionomer network, ultimately increasing the resistance to proton diffusion and reducing the ECSA (Figure 7, right).[20-21,43]

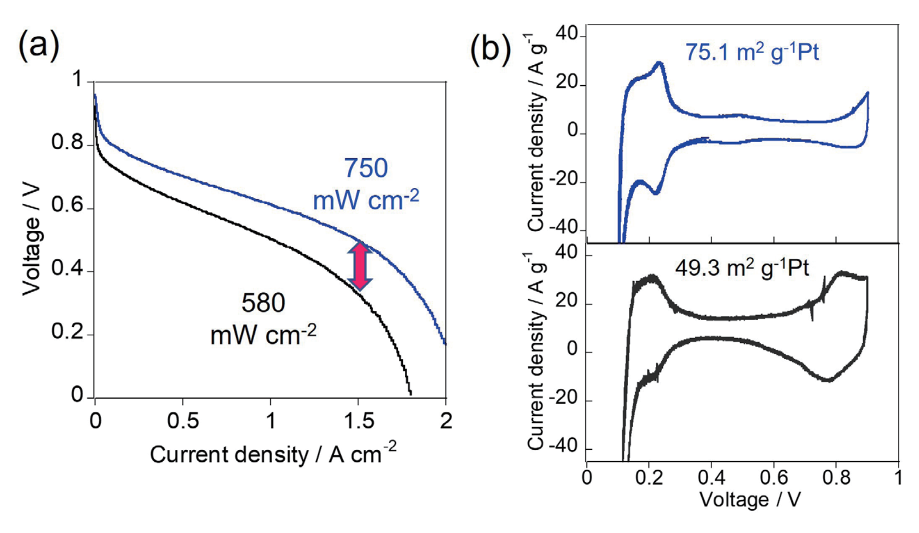

Fig. 6 Polarization curves (a) and in-situ cyclic voltammograms (b) for w-MEA (blue) and a-MEA (black).

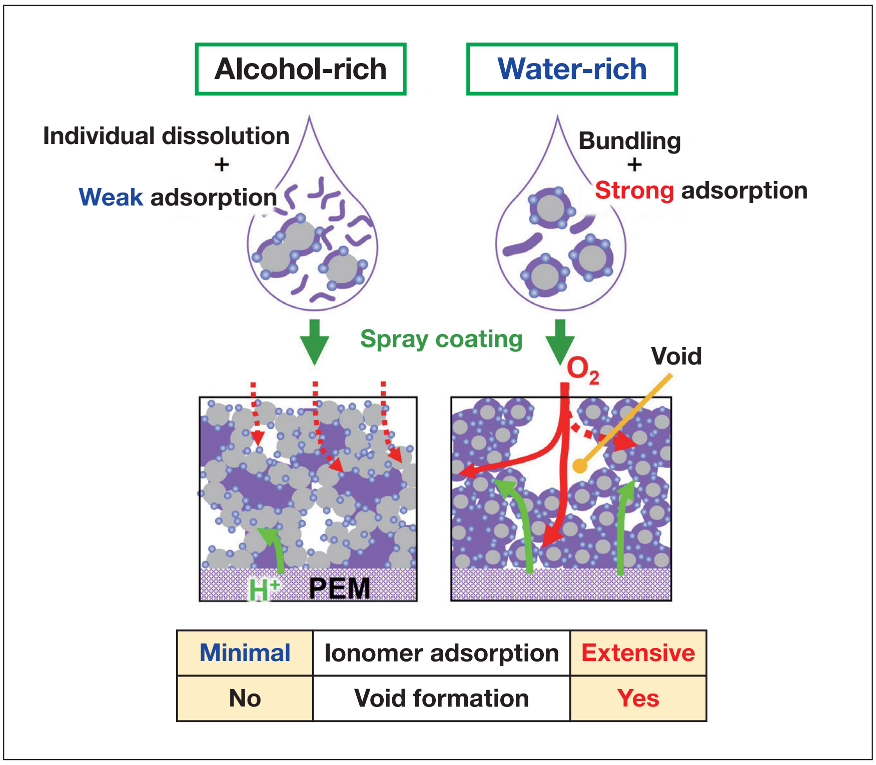

Fig. 7 Conceptual diagram illustrating formation of catalyst layers for alcohol-rich (left) and water-rich (right) solvents.

Oxygen-reduction reactions at cathodes are affected not only by proton diffusion, but also by resistance to oxygen diffusion—which, in turn, is known to depend both on diffusion through ionomers adsorbed on Pt surfaces and on bulk diffusion through catalyst layers. The results of our AC impedance analysis show that resistance to oxygen diffusion is lower for the w-MEA than for the a-MEA. In the alcohol-rich solvent, the adsorption forces binding ionomers to catalyst surfaces are weak, leaving many unadsorbed ionomers that remain in bulk regions of the catalyst layers and obstruct oxygen diffusion through these regions (Figure 7, left). In the water-rich solvent, by contrast, ionomers adhere strongly to catalyst surfaces, leaving void regions unobstructed; moreover, these void regions are interconnected by micropores, forming a structure that is conducive to oxygen diffusion through the bulk (Figure 7, right). Because ionomers adsorbed on Pt surfaces are known to obstruct ORRs by preventing oxygen molecules from being adsorbed on these surfaces, this is a key factor.[26,44,45] The results of adsorption isotherm measurements confirm that, in the water-rich solvent, ionomers tend to be adsorbed on carbon surfaces more than on Pt surfaces; in the alcohol-rich solvent, by contrast, ionomers tend to be adsorbed on Pt surfaces. However, at present this observation is based solely on studies of adsorption in ink; in future work we hope to conduct more detailed studies, via electrochemical analysis of catalyst layers and other techniques, to clarify how these mechanisms are reflected in actual adsorption behavior during nonequilibrium states—such as drying processes—or in the presence of overabundant ionomers.

3. Conclusions

In this study we used adsorption isotherm measurements to demonstrate that differences in the catalyst composition of fuel-cell inks give rise to differences in ionomer adsorption states. We showed that inks based on water-rich solvents are conducive to ionomer adsorption, and that this mechanism not only leads to the formation of proton-conduction pathways but also the preservation of oxygen-diffusion pathways. The ability to regulate ionomer adsorption in catalyst-layer surfaces offers direct control over fuel-cell behavior, and our work thus constitutes a new methodology for controlling the performance of fuel cells.[46]

References

1) Shao, M.; Chang, Q.; Dodelet, J.-P.; Chenitz, R., *Chem. Rev.* **2016**, *116* (6), 3594-3657.

2) Ma, Z.; Cano, Z. P.; Yu, A.; Chen, Z.; Jiang, G.; Fu, X.; Yang, L.; Wu, T.; Bai, Z.; Lu, J., *Angew. Chem., Int. Ed.* **2020**, *59* (42), 18334-18348.

3) Deng, X.; Zhang, J.; Fan, Z.; Tan, W.; Yang, G.; Wang, W.; Zhou, W.; Shao, Z., *Energy Fuels* **2020**, *34* (8), 9175-9188.

4) Kongkanand, A.; Mathias, M. F., *J. Phys. Chem. Lett.* **2016**, *7* (7), 1127-1137.

5) Chung, D. Y.; Yoo, J. M.; Sung, Y.-E., *Adv. Mater.* **2018**, *30* (42), 1870316.

6) Shahgaldi, S.; Hamelin, J., *Carbon* **2015**, *94*, 705-728.

7) Iden, H.; Mashio, T.; Ohma, A., *J. Electroanal. Chem.* **2013**, *708*, 87-94.

8) Suter, T. A. M.; Smith, K.; Hack, J.; Rasha, L.; Rana, Z.; Angel, G. M. A.; Shearing, P. R.; Miller, T. S.; Brett, D. J. L., *Adv. Energy Mater.* **2021**, *11* (37).

9) Qi, Z.; Kaufman, A., *J. Power Sources* **2003**, *113* (1), 37-43.

10) Sasikumar, G.; Ihm, J. W.; Ryu, H., *J. Power Sources* **2004**, *132* (1), 11-17.

11) Antolini, E.; Giorgi, L.; Pozio, A.; Passalacqua, E., *J. Power Sources* **1999**, *77* (2), 136-142.

12) Jeon, S.; Lee, J.; Rios, G. M.; Kim, H.; Lee, S.; Cho, E.; Lim, T.; Jang, J. H., *Int. J. Hydrogen Energy* **2010**, *35*, 9678.

13) Liu, Y.; Ji, C.; Gu, W.; Jorne, J.; Gasteiger, H. A., *J. Electrochem. Soc.* **2011**, *158* B614.

14) Alink, R.; Schüßler, M.; Pospischil, M.; Erath, D.; Gerteisen, D., *J. Power Sources* **2016**, *327*, 526.

15) Uchida, M.; Aoyama, Y.; Eda, N.; Ohta, A., *J. Electrochem. Soc.* **1995**, *142* (12), 4143-4149.

16) Passalacqua, E.; Lufrano, F.; Squadrito, G.; Patti, A.; Giorgi, L., *Electrochim. Acta* **2001**, *46* (6), 799-805.

17) Suzuki, T.; Tsushima, S.; Hirai, S., *Int. J. Hydrogen Energy* **2011**, *36* (19), 12361-12369.

18) Lee, M.-R.; Lee, H.-Y.; Yim, S.-D.; Kim, C.-S.; Shul, Y.-G.; Kucernak, A.; Shin, D., *Fuel Cells* **2018**, *18* (2), 129-136.

19) Kumano, N.; Kudo, K.; Suda, A.; Akimoto, Y.; Ishii, M.; Nakamura, H., *J. Power Sources* **2019**, *419*, 219-228.

20) Kishi, M.; Tanaka, M.; Mori, T., *J. Ceram. Soc. Jpn.* **2019**, *127* (12), 942-951.

21) Ngo, T. T.; Yu, T. L.; Lin, H.-L., *J. Power Sources* **2013**, *225*, 293-303.

22) Shin, S. J.; Lee, J. K.; Ha, H. Y.; Hong, S. A.; Chun, H. S.; Oh, I. H., *J. Power Sources* **2002**, *106* (1), 146-152.

23) Zamel, N., *J. Power Sources* **2016**, *309*, 141-159.

24) Fernández, R.; Ferreira-Aparicio, P.; Daza, L., *J. Power Sources* **2005**, *151*, 18-24.

25) Doo, G.; Lee, J. H.; Yuk, S.; Choi, S.; Lee, D.-H.; Lee, D. W.; Kim, H. G.; Kwon, S. H.; Lee, S. G.; Kim, H.-T., *ACS Appl. Mater. Interfaces* **2018**, *10* (21), 17835-17841.

26) Takahashi, S.; Mashio, T.; Horibe, N.; Akizuki, K.; Ohma, A., *ChemElectroChem* **2015**, *2* (10), 1560-1567.

27) Shukla, S.; Bhattacharjee, S.; Weber, A. Z.; Secanell, M., *J. Electrochem. Soc.* **2017**, *164* (6), F600-F609.

28) Huang, D. C.; Yu, P. J.; Liu, F. J.; Huang, S. L.; Hsueh, K. L.; Chen, Y. C.; Wu, C. H.; Chang, W. C.; Tsau, F. H., *Int. J. Electrochem. Sci.* **2011**, *6* (7), 2551-2565.

29) Orfanidi, A.; Rheinländer, P. J.; Schulte, N.; Gasteiger, H. A., *J. Electrochem. Soc.* **2018**, *165* (14), F1254-F1263.

30) Van Cleve, T.; Khandavalli, S.; Chowdhury, A.; Medina, S.; Pylypenko, S.; Wang, M.; More, K. L.; Kariuki, N.; Myers, D. J.; Weber, A. Z.; Mauger, S. A.; Ulsh, M.; Neyerlin, K. C., *ACS Appl. Mater. Interfaces* **2019**, *11* (50), 46953-46964.

31) Van Cleve, T.; Wang, G.; Mooney, M.; Cetinbas, C. F.; Kariuki, N.; Park, J.; Far-ghaly, A.; Myers, D.; Neyerlin, K. C., *J. Power Sources* **2021**, *482*, 228889.

32) Kusoglu, A.; Weber, A. Z., *Chem. Rev.* **2017**, *117* (3), 987-1104.

33) Mizukawa, H.; Kawaguchi, M., *Langmuir* **2009**, *25* (20), 11984-11987.

34) Thoma, M.; Lin, W.; Hoffmann, E.; Sattes, M.-M.; Segets, D.; Damm, C.; Peukert, W., *Langmuir* **2018**, *34* (41), 12324-12334.

35) Andersen, S. M.; Borghei, M.; Dhiman, R.; Jiang, H.; Ruiz, V.; Kauppinen, E.; Skou, E., *Carbon* **2014**, *71*, 218-228.

36) Andersen, S. M.; Borghei, M.; Dhiman, R.; Ruiz, V.; Kauppinen, E.; Skou, E., *J. Phys. Chem. C* **2014**, *118* (20), 10814-10823.

37) Andersen, S. M., *Appl. Catal., B* **2016**, *181*, 146-155.

38) Ma, S.; Chen, Q.; Jøgensen, F. H.; Stein, P. C.; Skou, E. M., *Solid State Ionics* **2007**, *178* (29), 1568-1575.

39) Berlinger, S. A.; McCloskey, B. D.; Weber, A. Z., *J. Phys. Chem. B* **2018**, *122* (31), 7790-7796.

40) Yamaguchi, M.; Matsunaga, T.; Amemiya, K.; Ohira, A.; Hasegawa, N.; Shinoha-ra, K.; Ando, M.; Yoshida, T., *J. Phys. Chem. B* **2014**, *118* (51), 14922-14928.

41) Salou, M.; Siffert, B.; Jada, A., *Fuel* **1998**, *77* (4), 339-341.

42) Jayawickrama, S. M.; Wu, D.; Nakayama, R.; Ishikawa, S.; Liu, X.; Inoue, G.; Fujigaya, T., *J. Power Sources* **2021**, *496*, 229855.

43) Kishi, M.; Moriyama, S.; Mori, T., *Journal of the Society of Powder Technology, Japan* **2018**, *55* (7), 366-374.

44) Ohma, A.; Fushinobu, K.; Okazaki, K., *Electrochim. Acta* **2010**, *55* (28), 8829-8838.

45) Kodama, K.; Shinohara, A.; Hasegawa, N.; Shinozaki, K.; Jinnouchi, R.; Suzuki, T.; Hatanaka, T.; Morimoto, Y., *J. Electrochem. Soc.* **2014**, *161* (5), F649-F652.

46) Wu, D.; Kayo, N.; Jayawickrama, S. M.; Phua, Y. K.; Tanaka, N.; Fujigaya, T., *Int. J. Hydrogen Energy* **2023**, *48* (15), 5915-5928.

SCIENTIFIC INSTRUMENT NEWS
2024 Vol. 21 MARCH
Technical magazine of Electron Microscope and Analytical Instruments.
Article
2024 Vol.21

Perspectives on Therapeutic Drug Monitoring for Antimicrobials in Infection Care in Emergency and Intensive Care Medicine

Kazutaka Oda
Department of Pharmacy and Department of Infection Control
Kumamoto University Hospital

1. Introduction

Therapeutic drug monitoring (TDM) is an approach for optimizing drug treatment regimens for individual patients based on the measurement of blood drug concentrations. Under the classical concept, TDM was done to avoid adverse events caused by drugs with narrow therapeutic windows that caused toxicities when given at even slightly elevated doses. TDM is applied in Japan for the immunosuppressants tacrolimus and cyclosporine, antiepileptics, and antiarrhythmics, and antimicrobials (e.g., aminoglycosides, glycopeptides, and the antifungal voriconazole). Ample evidence supports TDM for vancomycin used as first-line treatment for methicillin-resistant *Staphylococcus aureus*, which is a notable example of antimicrobial resistance. The concept of TDM has been evolving in recent years.

The International Association of Therapeutic Drug Monitoring and Toxicology (IATDMCT) offers the following definition of TDM: *"TDM is a multi-disciplinary clinical specialty aimed at improving patient care by individually adjusting the dose of drugs for which clinical experience or clinical trials have shown it improved outcome in the general or special populations"*1). The Japanese Society of Therapeutic Drug Monitoring defines TDM as "Pharmacotherapy individualized for patients while monitoring for factors related to therapeutic efficacy and adverse reactions"2). Notably, these definitions show that TDM is no longer done solely to avoid adverse reactions in individual patients and not necessarily limited to drugs with narrow therapeutic windows. This paper discusses the perspectives on antimicrobial TDM for infection treatment in emergency and intensive care settings. It focuses primarily on beta-lactam drugs, which were not considered in conventional TDM.

2. The Significance and Uptake of TDM for Beta-lactam Drugs in Europe

Beta-lactam drugs are widely used for their excellent safety profile and powerful bactericidal effects. Research is progressing on TDM of beta-lactam drugs with the goal of increasing survival in patients with infections. The defining antibiotic levels in intensive care unit patients (DALI) study by Roberts and colleagues showed that 16% of emergency/intensive care patients did not achieve adequate antibiotic exposure and may have benefited from higher doses3). The study also showed that blood concentrations of antibiotics varied markedly (Figure 1)3).

These findings mean that, if a fixed dose of an antimicrobial is to be increased as a strategy for reliably bringing the blood concentration of the drug within the therapeutic range, a high dose will have to be given to allow for patients who achieve the lowest concentrations. Figure 1 shows that, for the instance with the highest concentration, this would involve achieving a high concentration more than 60-fold that of the necessary concentration. Beta-lactam drugs, although safe, still pose risks to the central nervous system at extremely high doses. Beumier and colleagues defined a beta-lactam drug concentration exceeding 4 times the trough concentration / minimum inhibitory concentration (MIC) as a risk factor for neurotoxicity4). Encephalopathy is occasionally reported in association with cefepime and ceftriaxone5-7). Thus, though a certain number of patients in emergency and intensive care settings require high-dose beta-lactam treatment to survive, there was no clear way to safely increase the dose. TDM has emerged as a solution.

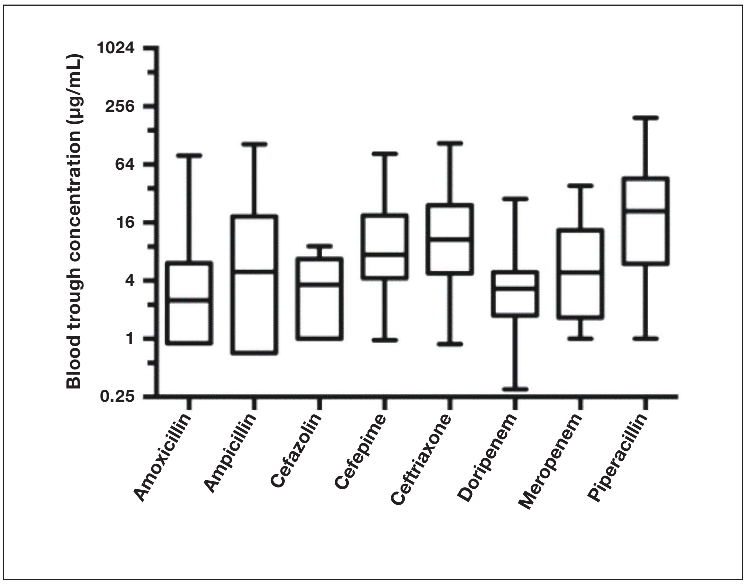

Fig. 1 Variation in blood trough concentrations of beta-lactam drugs in emergency/intensive care patients
The vertical axis in log scale shows the extent of the variation in trough values
Source : Roberts JA, et al. Clin Infect Dis. 2014 Apr;58(8):1072-83.

European medical institutions are actively engaged in TDM for beta-lactam drugs. In 2019, The French Society of Pharmacology and Therapeutics and the French Society of Anaesthesia and Intensive Care Medicine released the world's first guidelines on TDM for beta-lactam drugs[8]. The guidelines recommend TDM based on trough blood samples from 24 to 48 hours after the start of beta-lactam treatment. They also contain a flowchart showing a treatment design strategy based on concentration measurements (Figure 2). In the flowchart, the target concentration is from 4 to less than 8 times MIC, but it should be remembered that, as previously stated, concentrations exceeding 4 times MIC pose a risk of central nervous system adverse reactions. (Under these criteria, lower MIC values pose a lower risk of such adverse reactions.) The extent of the uptake of TDM for beta-lactam drugs in Europe was investigated in a 2016 study. In intensive care units in France, TDM was done for 30% of patients treated with ceftazidime, 21% of patients treated with piperacillin, and 19% of patients treated with meropenem[9]. In 2022, TDM for beta-lactam drugs given to patients on continuous renal replacement therapy was used in 45% of patients in university hospitals and 41% of patients in other types of hospitals, showing steady expansion of TDM[10]. Use of TDM in the Netherlands and Germany ranges from 15% to 30% for meropenem[11,12].

As stated, TDM has been proposed as a strategy for reliably bringing antimicrobial drug concentrations into the therapeutic range to better save lives. TDM for beta-lactam drugs in Europe is now beyond its infancy and has entered a phase of broader adoption.

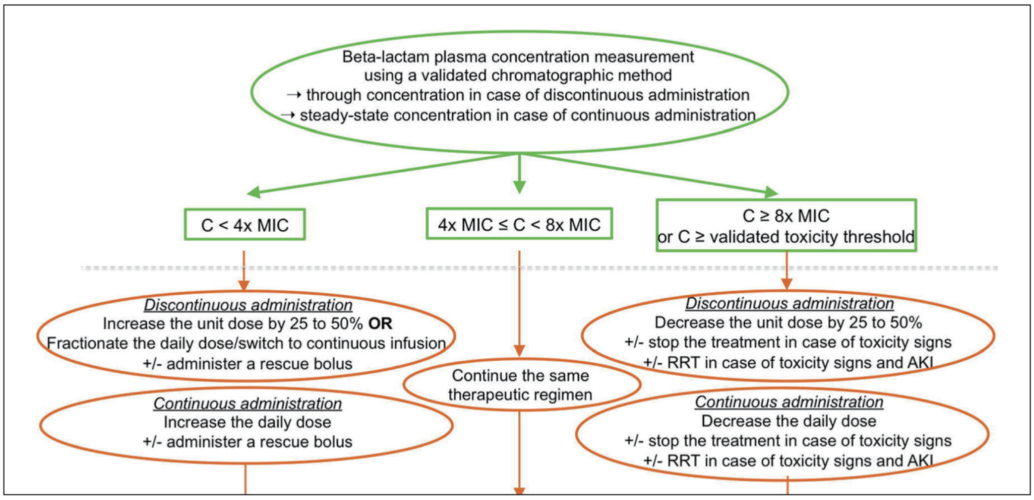

Fig. 2 Flowchart for adjusting dosages of beta-lactam drugs based on blood concentrations in TDM
The target concentration is from 4 to less than 8 times MIC, but the risk of neurotoxicity must be kept in mind.
Source : Guilhaumou R, et al. Crit Care. 2019 Mar 29;23(1):104.

3. Evidence Supporting TDM for Beta-lactam Drugs

No randomized, controlled trial (RCT) has shown that TDM enhances the therapeutic efficacy of beta-lactam drugs. The Dutch investigator Ewoldt and colleagues performed an RCT that included 388 intensive care patients administered beta-lactam drugs and ciprofloxacin who were assigned to treatment with or without TDM. TDM, however, failed to shorten ICU length of stay[13]. Blood concentrations in the non-TDM group (called the “standard dosing group” in the paper) showed a profile comparable to that of the TDM group (called the “MIPD group” in the paper). The investigators concluded that the study did not provide evidence to support TDM in patients with severe disease. Even so, given the nature of this study in general intensive care patients, it would be appropriate to find that beta-lactam TDM should not be recommended for all intensive care patients, and that investigations should proceed in a more limited group of patients.

Observational studies have investigated the effects on therapeutic efficacy of keeping the time the free antibiotic concentration is maintained above the minimum inhibitory concentration (%fT>MIC) at 50% or 100%[3,14].

In summary, although there are no consensus target values for %fT>MIC for beta-lactam TDM, keeping values near these figures reportedly does affect therapeutic efficacy. To better demonstrate the effects of TDM on therapeutic efficacy, robust clinical studies limited to patients on TDM or with infections or in certain situations must be conducted. On this point, I believe that such RCTs are feasible because TDM for beta-lactam drugs is now used fairly widely in Europe. Such RCTs, however, are not feasible in Japan because beta-lactam TDM is not in use. Japan therefore lags Europe in beta-lactam TDM both in clinical practice and in studies. A solution is needed.

4. Uptake of Blood Concentration Analyzers in Japan

Blood concentration analyzers are key to beta-lactam TDM uptake. A 2022 survey of the status of hospital pharmacies by the Japanese Society of Hospital Pharmacists showed that drug concentration analysis was performed by pharmacies at 12.5% and by internal laboratories at 59.1% of the institutions surveyed[15]. These figures indicate that institutions have a substantial appreciation of TDM. However, with tests for beta-lactam drugs not covered under Japan’s national health insurance program, there is likely next to no assimilation of instruments capable of analyzing these drugs into clinical use. I contributed to joint research performed in the development of Hitachi High-Tech Science Corporation’s LM1010 drug concentration analyzer and have already clinically evaluated drugs including carbamazepine[16], phenytoin[16], lamotrigine, voriconazole[17], meropenem, and vancomycin (Figure 3). The LM1010 is capable of measuring meropenem and other beta-lactam drug concentrations, in addition to those of many other drugs, and the drugs it can measure are being expanded.

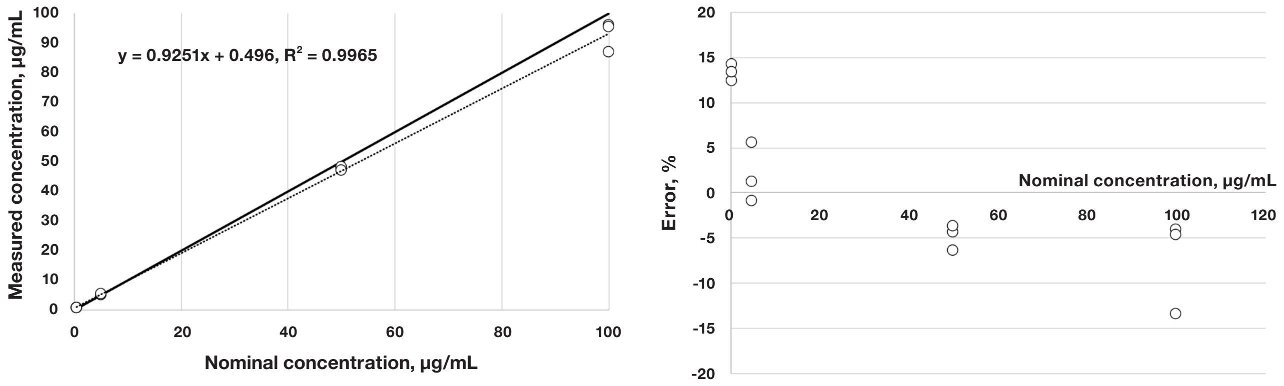

Fig. 3 Evaluation of meropenem concentration analysis
n=3 at the nominal concentrations of 0.5, 5, 50, and 100 μg/mL.
Left: Solid line is y=x, dotted line is regression line.
Right: Systematic error in Bland-Altman analysis. At the low concentration end, measured concentrations tended to deviate from nominal concentrations in the positive direction, but by no more than 15%. Accuracy is not an issue.

Indeed, the 2022 Guidelines for the Clinical Practice of Antimicrobial TDM propose using the area under the concentration time curve (AUC) on day 2 of treatment as a measure for treatment with vancomycin, which is a drug widely known to require TDM[18]. This proposal not only requires rapid action on day 2 of treatment, but also expertise regarding the AUC. These requirements essentially call for active involvement in TDM by pharmacy units. This addition to the Guidelines is prompting more medical institutions to work to do blood vancomycin concentration analyses internally rather than through contract laboratories. Institutions that purchase an LM1010 as they internalize analyses would gain a blood drug analyzer that is also able to measure beta-lactam drug concentrations.

5. Clinical Practice of Beta-lactam Drug TDM and Effects on Pharmacotherapy

TDM for beta-lactam drugs, whose blood concentrations vary substantially, most notably allows efficient dose adjustment to better save lives, as mentioned before. These efficiency gains will help caregivers not only reduce the risk of adverse events as they increase therapeutic efficacy, but also design special dosage regimens and reduce costs. Through journal articles and conference presentations, I am informing others about the patients who have benefited in my clinical practice of beta-lactam TDM in various forms.

5-1. TDM saves a patient with severe pneumonia caused by *Pseudomonas aeruginosa*

A common cause of infections, *P. aeruginosa*, can defy treatment when it becomes drug-resistant, as it often does. Some of the drugs used to treat drug-resistant *P. aeruginosa* are highly toxic (e.g., colistin). When possible, safe beta-lactam drugs are a better option. We have treated patients with *P. aeruginosa* that was resistant to doripenem (a beta-lactam carbapenem), which has an MIC of 8 μg/mL. To avoid the need to use colistin, I used TDM to maintain the blood concentration of doripenem at 32 μg/mL, or 4 times the MIC. With my colleagues, I submitted a case report about the affected patient (Figure 4)[19].

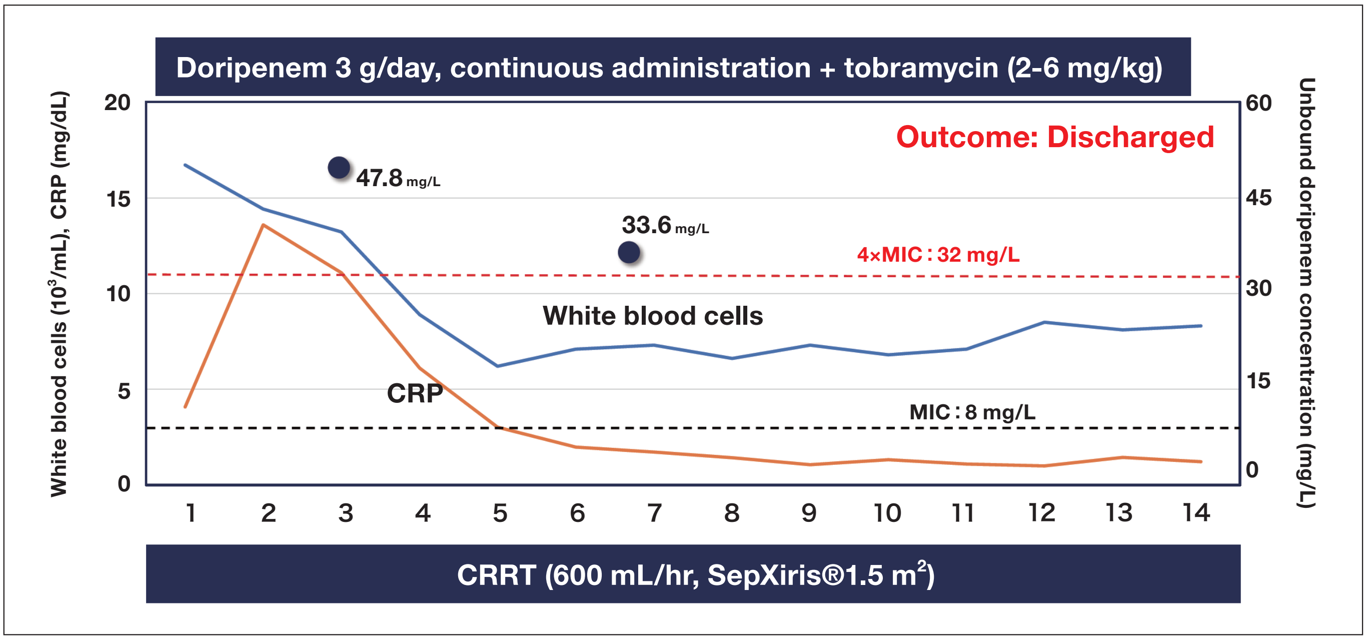

Fig. 4 TDM of doripenem to treat drug-resistant *P. aeruginosa*
Black circles indicate unbound doripenem concentrations in the serum.
CRRT: Continuous renal replacement therapy
Source : Oda K, et al. J Pharm Health Care Sci. 2019;5:15.

5-2. Avoiding adverse events

At excessive doses, cefepime causes encephalopathy[5]. TDM can be used to avoid this undesirable effect. I encountered a patient with aphasia who appeared to have cefepime-induced neurotoxicity. TDM showed a high cefepime concentration of 71.3 μg/mL. We would have considered switching to another drug but knew the patient had *P. aeruginosa* that had already become resistant to other drugs. We therefore decided to reduce the dose based on the pharmacokinetic analysis of cefepime. This approach cured the infection (Figure 5)[20].

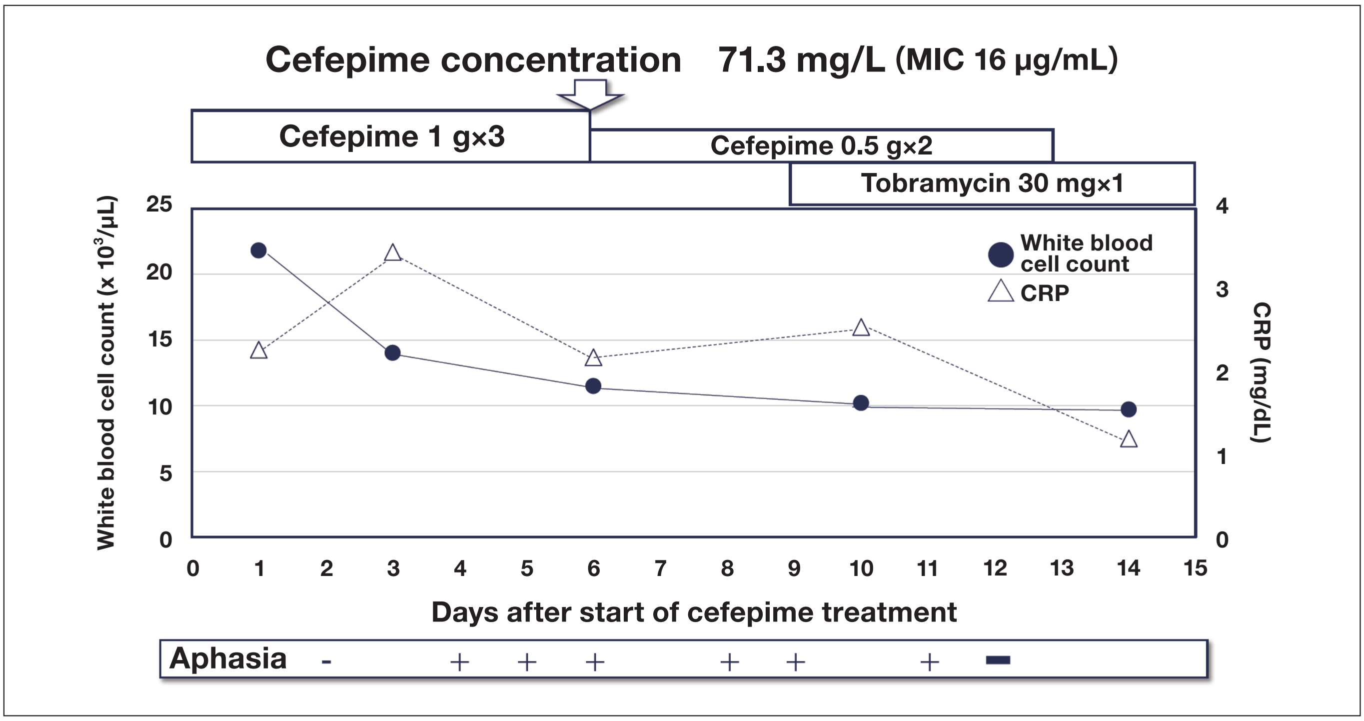

Fig. 4 Ongoing cefepime treatment for drug-resistant *P. aeruginosa*
TDM-based dose reduction of cefepime for neurotoxicity in this patient with aphasia cured the infection.
Source : Oda K, et al. J Infect Chemother. 2020;26(5):498–501.

5-3. A specially designed dosage regimen to keep a patient off carbapenems

Mediastinitis is a serious complication of cardiovascular surgery. Since information about antimicrobial uptake by the mediastinum is lacking, drugs must be selected with the utmost of care. A patient we treated had mediastinitis caused by an extended-spectrum beta-lactamase (ESBL)-producer. Since carbapenems are recommended as first-line treatment for infections by ESBL-producers, a carbapenem must be used in most instances. We, however, decided to continuously administer flomoxef and cefmetazole (which are known to be effective in mild urinary tract and other infections) while monitoring concentrations of the unbound forms of these drugs in the mediastinum and blood, thereby keeping the patient off carbapenems. The concentrations of the unbound drugs in the mediastinum were, relative to a target concentration of MIC $\leq$ 4 μg/mL, 10.6 μg/mL for flomoxef and 7.0 μg/mL for cefmetazole. These concentrations cured the infection.

5-4. Reducing costs

We were involved in the treatment of a patient with *P. aeruginosa* pneumonia. The patient's blood cultures remained positive for over 3 weeks despite treatment with the maximum dose of ceftazidime as an antibiotic to which the bacterium was sensitive. We determined the blood concentration to refer to just in case the drug concentration was too low and required switching to a carbapenem or other drug. *P. aeruginosa* remained sensitive because the MIC was 8 μg/mL. The patient, however, had extremely high trough and peak concentrations of 56 and 97.7 μg/mL. We told the team these concentrations were overkill. The dose was halved. The patient's blood culture subsequently tested negative. In this case, avoiding unnecessary antibiotic use helped reduce costs.

6. Conclusions

TDM is demonstrably useful in beta-lactam treatment design. Through my clinical experience, I realize that TDM helps caregivers avoid giving patients overly broad antimicrobials by providing information about therapeutic efficacy, as I have discussed in the above cases involving the use of flomoxef and cefmetazole, ongoing use of cefepime, and dose reduction of ceftazidime. After all, reducing the doses of broad-spectrum antimicrobials used is a critical step in solving the problem of antimicrobial resistance. Since Japan's national health insurance program does not cover beta-lactam TDM, personnel at most institutions will probably be hesitant to do beta-lactam TDM on a "volunteer" basis. However, given the high price of most broad-spectrum antimicrobials, avoiding their use, and avoiding high doses as in the above case involving ceftazidime, will help reduce costs for hospitals. In a future paper, I wish to show how beta-lactam TDM can increase profitability at individual medical institutions.

References

1) https://www.iatdmct.org/about-us/about-association/about-definitions-tdm-ct.html, accessed on September 12, 2023 (in Japanese).

2) https://jstdm.jp/yogo/basic_knowledge.html, accessed on September 12, 2023.

3) Roberts JA, Paul SK, Akova M, Bassetti M, De Waele JJ, Dimopoulos G, Kaukonen KM, Koulenti D, Martin C, Montravers P, Rello J, Rhodes A, Starr T, Wallis SC, Lipman J; DALI Study. DALI: defining antibiotic levels in intensive care unit patients: are current β-lactam antibiotic doses sufficient for critically ill patients? Clin Infect Dis. 2014 Apr;58(8):1072-83. doi: 10.1093/cid/ciu027. Epub 2014 Jan 14. PMID: 24429437.

4) Beumier M, Casu GS, Hites M, Wolff F, Cotton F, Vincent JL, Jacobs F, Taccone FS. Elevated β-lactam concentrations associated with neurological deterioration in ICU septic patients. Minerva Anestesiol. 2015 May;81(5):497-506. Epub 2014 Sep 15. PMID: 25220556.

5) Ajibola O, Aremu TO, Dada SO, Ajibola O, Adeyinka KO, Ajibola A, Oluwole OE. The Trend of Cefepime-Induced Neurotoxicity: A Systematic Review. Cureus. 2023 Jun 26;15(6):e40980. doi: 10.7759/cureus.40980. PMID: 37503476; PMCID: PMC10370502.

6) Satake K, Iijima K. Ceftriaxone-Induced Neutropenia Successfully Treated With Alternative β-Lactam Antibiotics: A Case Report and Review of the Literature. Cureus. 2023 May 18;15(5):e39176. doi: 10.7759/cureus.39176. PMID: 37332438; PMCID: PMC10276520.

7) Ichinose N, Yoshikawa G, Fukao E, Takahata T, Ichisawa M, Enoki Y, Taguchi K, Oda T, Tsutsumi K, Matsumoto K. Influences of protein levels on the cerebrospinal fluid distribution of ceftazidime & ceftriaxone in the cerebrospinal fluid of patients with inflamed meningitis. J Infect Chemother. 2022 Aug;28(8):1216-1219. doi: 10.1016/j.jiac.2022.04.021. Epub 2022 May 2. PMID: 35513971.

8) Guilhaumou R, Benaboud S, Bennis Y, Dahyot-Fizelier C, Dailly E, Gandia P, Goutelle S, Lefeuvre S, Mongardon N, Roger C, Scala-Bertola J, Lemaitre F, Garnier M. Optimization of the treatment with beta-lactam antibiotics in critically ill patients-guidelines from the French Society of Pharmacology and Therapeutics (Société Française de Pharmacologie et Thérapeutique-SFPT) and the French Society of Anaesthesia and Intensive Care Medicine (Société Française d'Anesthésie et Réanimation-SFAR). Crit Care. 2019 Mar 29;23(1):104. doi: 10.1186/s13054-019-2378-9. PMID: 30925922; PMCID: PMC6441232.

9) Charmillon A, Novy E, Agrinier N, Leone M, Kimmoun A, Levy B, Demoré B, Dellamonica J, Pulcini C. The ANTIBIOPERF study: a nationwide cross-sectional survey about practices for β-lactam administration and therapeutic drug monitoring among critically ill patients in France. Clin Microbiol Infect. 2016 Jul;22(7):625-31. doi: 10.1016/j.cmi.2016.04.019. Epub 2016 May 1. PMID: 27145210.

10) Matusik E, Lemtiri J, Wabont G, Lambiotte F. Beta-lactam dosing during continuous renal replacement therapy: a survey of practices in french intensive care units. BMC Nephrol. 2022 Jan 29;23(1):48. doi: 10.1186/s12882-022-02678-x. PMID: 35093011; PMCID: PMC8800323.

11) Ewoldt TMJ, Abdulla A, van den Broek P, Hunfeld N, Bahmany S, Muller AE, Gommers D, Polinder S, Endeman H, Spronk I, Koch BCP. Barriers and facilitators for therapeutic drug monitoring of beta-lactams and ciprofloxacin in the ICU: a nationwide cross-sectional study. BMC Infect Dis. 2022 Jul 13;22(1):611. doi: 10.1186/s12879-022-07587-w. PMID: 35831793; PMCID: PMC9277596.

12) Liebchen U, Paal M, Scharf C, Schroeder I, Grabein B, Zander J, Siebers C, Zoller M. The ONTAI study - a survey on antimicrobial dosing and the practice of therapeutic drug monitoring in German intensive care units. J Crit Care. 2020 Dec;60:260-266. doi: 10.1016/j.jcrc.2020.08.027. Epub 2020 Sep 4. PMID: 32932111.

13) Ewoldt TMJ, Abdulla A, Rietdijk WJR, Muller AE, de Winter BCM, Hunfeld NGM, Purmer IM, van Vliet P, Wils EJ, Haringman J, Draisma A, Rijpstra TA, Karakus A, Gommers D, Endeman H, Koch BCP. Model-informed precision dosing of beta-lactam antibiotics and ciprofloxacin in critically ill patients: a multicentre randomised clinical trial. Intensive Care Med. 2022 Dec;48(12):1760-1771. doi: 10.1007/s00134-022-06921-9. Epub 2022 Nov 9. PMID: 36350354; PMCID: PMC9645317.

14) McKinnon PS, Paladino JA, Schentag JJ. Evaluation of area under the inhibitory curve (AUIC) and time above the minimum inhibitory concentration (T>MIC) as predictors of outcome for cefepime and ceftazidime in serious bacterial infections. Int J Antimicrob Agents. 2008 Apr;31(4):345-51. doi: 10.1016/j.ijantimicag.2007.12.009. Epub 2008 Mar 4. PMID: 18313273.

15) Results of Fiscal 2022 Survey of Hospital Pharmacies. https://mhlw-grants.niph.go.jp/system/files/report_pdf/202222028A-sokatsu_shiryo1.pdf, accessed on September 12, 2023 (in Japanese).

16) Oda K, Iwamura K, Katanoda T, Narita Y, Uchino S, Kurogi K, Horikawa M, Matsumoto N, Yonemaru K, Yamaguchi A, Jono H, Saito H. Evaluation of the Performance and Precision of the LM1010 HPLC-based Blood Drug Concentration Analyzer (evaluation model). October 24 to November 1, 2020. 30th Annual Meeting of the Japanese Society of Pharmaceutical Health Care and Sciences, Kumamoto (held online) (in Japanese).

17) Oda K, Uchino S, Kurogi K, Horikawa M, Matsumoto N, Yonemaru K, Arakaki H, Katsume T, Matsuyama K, Katanoda T, Narita Y, Iwamura K, Jono H, Saito H. Clinical evaluation of an authorized medical equipment based on high performance liquid chromatography for measurement of serum voriconazole concentration. J Pharm Health Care Sci. 2021 Nov 9;7(1):42. doi: 10.1186/s40780-021-00225-8. PMID: 34749825; PMCID: PMC8576885.

18) 2022 Guidelines for the Clinical Practice of Antimicrobial TDM (in Japanese).

19) Oda K, Kamohara H, Katanoda T, Hashiguchi Y, Iwamura K, Nosaka K, Jono H, Saito H. Continuous high-dose infusion of doripenem in a pneumonia patient infected by carbapenem-resistant Pseudomonas aeruginosa: a case report. J Pharm Health Care Sci. 2019 Jul 8;5:15. doi: 10.1186/s40780-019-0144-4. PMID: 31321067; PMCID: PMC6613258.

20) Oda K, Miyakawa T, Katanoda T, Hashiguchi Y, Iwamura K, Nosaka K, Yamaguchi A, Jono H, Saito H. A case of recovery from aphasia following dose reduction of cefepime by bayesian prediction-based therapeutic drug monitoring. J Infect Chemother. 2020 May;26(5):498-501. doi: 10.1016/j.jiac.2019.10.006. Epub 2020 Mar 4. PMID: 32143960.

SCIENTIFIC INSTRUMENT NEWS
2024 Vol.21 MARCH
Technical magazine of Electron Microscope and Analytical Instruments.
Technical Explanation
2024 Vol.21

Introducing Hitachi's UH5200/5210 Double-Beam UV/Visible Spectrometer Series: Key Features and Measurement Examples

Jun Horigome

1. Introduction

A *UV/visible spectrophotometer* is an instrument that irradiates a sample with monochromatic light—obtained by passing white light through a prism or diffraction grating—and detects the transmitted light to identify substances present in the sample and measure their concentrations. Spectrophotometers are used in a wide range of academic and industrial fields, including materials science, environmental studies, pharmaceuticals, and bioengineering, and may be subdivided into categories—such as *photometers, single-beam* instruments, and *double-beam* instruments—based on the measurement precision and objectives. In particular, the high stability of double-beam spectrophotometers makes these instruments a common choice for applications in research and development, quality control, and environmental monitoring. More specifically, *R&D* applications of double-beam spectrophotometers include controlling the concentration of functional components of foods and beverages, quantifying nucleic acids and analyzing proteins, and identifying the functional properties of substances such as paints and light-absorbing agents; *quality-control* applications include analyzing food additives, measuring the purity of pharmaceuticals and controlling their ingredients, and confirming compliance with RoHS restrictions on hexavalent chromium and other toxic substances; and *environmental-monitoring* applications include measuring organic-matter content in drinking water and waste water and quantifying nutrient salts (such as phosphorus and nitrogen) in environmental water.

In this article we present key features of Hitachi High-Tech's UH5200/5210 double-beam UV/visible spectrophotometer (Figure 1), a new product designed for reliability and ease of use.

Fig. 1 The UH5200/UH5210 double-beam UV/visible spectrophotometer.

2. Key Features and Fields of Application

2-1. Choice of two operating configurations based on measurement objectives

The UH5200 series lineup consists of the UH5200, a standalone instrument, and the UH5210, a PC-controlled instrument.

The UH5200 features a 10.4-inch backlit color LCD display with 800×600-pixel resolution—higher than the previous-generation U-2900 system—to allow detailed visualization of calibration curves and measured spectra. The layout of the display screen is unchanged from that of previous-generation instruments, offering users a familiar operating experience with enhanced readability thanks to a new graphic design. A dedicated keyboard allows accurate, worry-free input (Figure 2).

The UH5210 is a fully PC-controlled instrument. Its control software is UV Solutions Plus, a new platform that is an update to the UV Solutions control software of the previous-generation U-2900 system with expanded functionality, including display of data lists and data-processing results in tabular form, report layouts, and performance validation (Figure 3). The UH5200 also offers the option of adding the UV Solutions Plus software platform to allow PC control.

Fig. 2 UH5200 measurement menu screen and keypad.

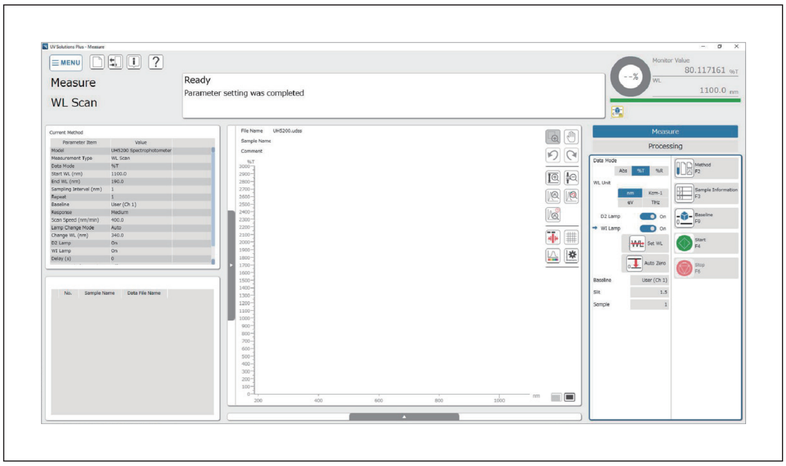

Ready

Parameter setting was completed

Current Method

Parameter Item	Value
Model	UH5200 Spectrophotometer
Measurement Type	WL Scan
Data Mode	%T
Start WL (nm)	1100.0
End WL (nm)	190.0
Sampling Interval (nm)	1
Repeat	1
Baseline	User (Ch 1)
Response	Medium
Scan Speed (nm/min)	400.0
Lamp Change Mode	Auto
Change WL (nm)	340.0
D2 Lamp	On
WI Lamp	On
Delay (s)	0

Baseline User (Ch 1)

Slit 1.5

Sample 1

Fig. 3 UV Solutions Plus home screen.

2-2. Basic performance: Reliability

The optical systems of UH5200 instruments use Seya-Namioka monochromators, a widely used type of monochromator based on a concave diffraction grating (Figure 4). Concave diffraction gratings serve both to focus and to disperse light, thus allowing optical systems to be implemented with fewer mirrors. Reducing the number of mirrors in a spectrophotometer not only reduces optical losses, but also shortens optical path lengths, yielding a brighter optical system. Hitachi's proprietary *ruling engine* technology for fabricating diffraction gratings enables bright, aberration-free optical systems. In addition, the use of a *double-beam* optical system—in which half-mirrors are used to split the optical path into two segments, compensating for variations in optical energy, including from the light source—ensures measurement stability over long periods of time.

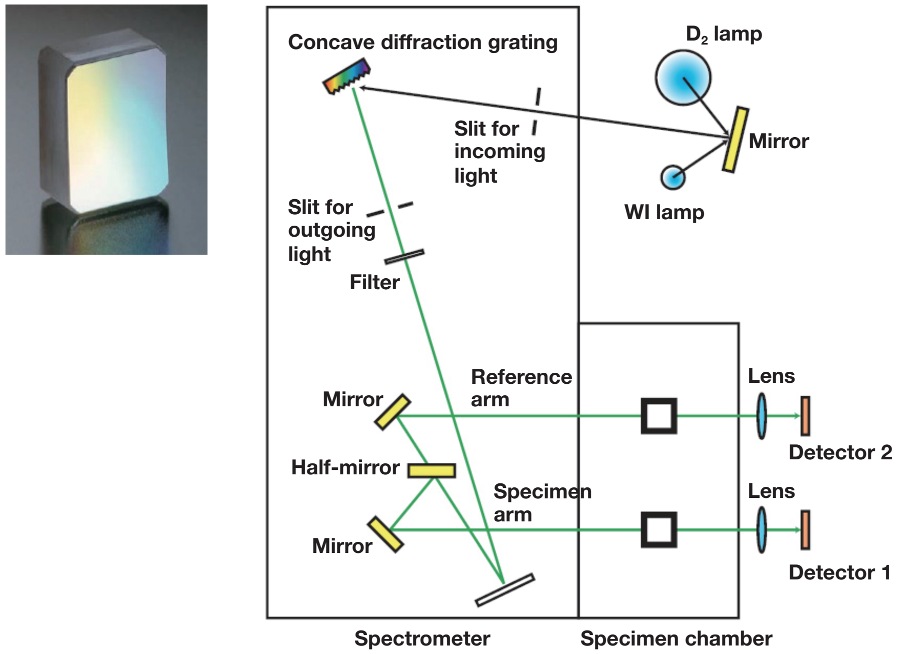

Fig. 4 Optical system of UH5200 series instruments.

2-3. New features

1) New lamp controls designed for safety and environmental impact

Making accurate spectrophotometer measurements requires a lamp capable of stable operation for long periods of time. UH5200 series instruments are equipped with the capability to turn the lamp on and off automatically, thus avoiding unnecessary on-time. When the lamp is turned on, the instrument monitors its output and automatically notifies the operator when this output has stabilized, indicating that measurements may now begin. Also, as a new safety provision, the UH5200 series now incorporates a sensor to detect whether the lamp chamber is open or closed during the lamp-replacement process (Figure 5).

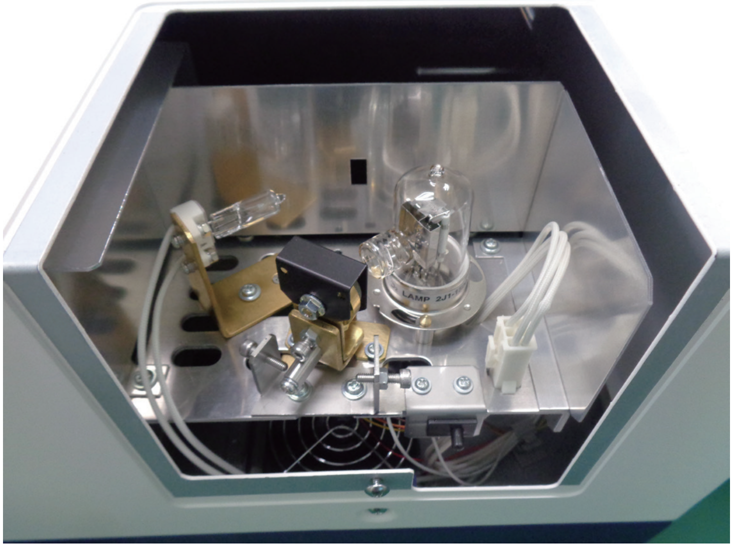

Fig. 5 The lamp chamber.

2) Support for bar-code readers in standalone configuration

UH5200 instruments provide USB ports for connecting external devices such as keyboards, bar-code readers, or thumb drives (Figure 6)*1). Bar-code readers may be used to streamline the process of specifying names for measurement specimens, while thumb drives (USB memory sticks) may be used for data storage.

*1) External input devices are provided by operators, not included with the UH5200 system.

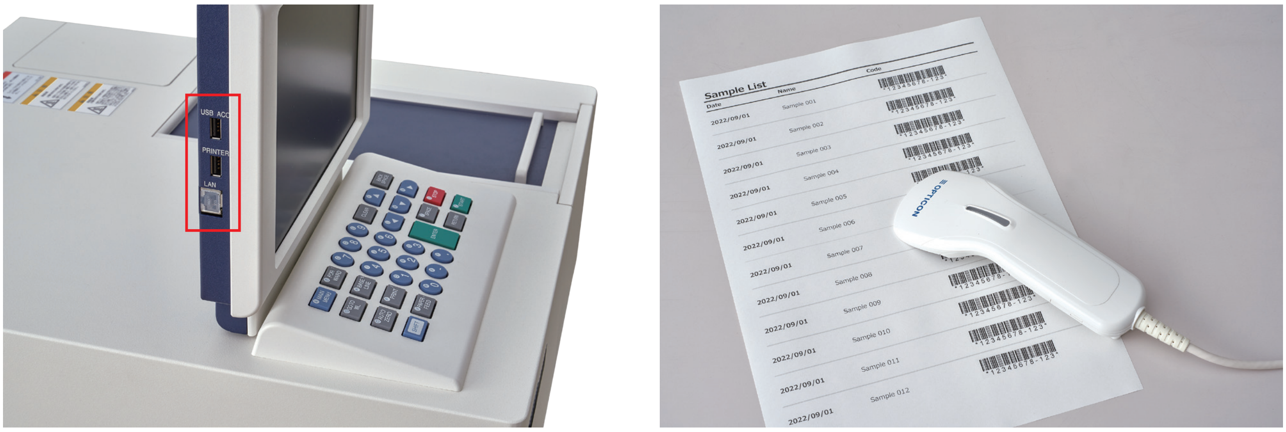

Fig. 6 UH5200-series instruments provide USB ports (left) for connecting external devices such as bar-code readers (right).

3. Sample Measurements

3-1. Measuring hexavalent chromium: absorption spectroscopy of diphenylcarbazide

Environmental regulations designed to protect the health of individuals affected by pollution of public bodies of water, as well as environmental regulations governing pollution in ground water, have tightened the permissible threshold for hexavalent chromium from 0.05 mg/L to 0.02 mg/L. In general, environmental regulations protecting human health specify that measurements are to be made using absorption cells with an optical path length of 50 mm. Here we present measurements of hexavalent chromium using an UH5200 equipped with a custom-made auto-sipper compatible with 50-mm optical-path-length cells. The autosipper improves measurement throughput—and, when combined with an autosampler to automate the mounting of measurement specimens in the instrument, can significantly reduce the effort required from human operators.

Figure 7 shows absorption spectra obtained in wavelength-scan mode (left) and a calibration curve obtained in photometry mode (right). For a peak absorption wavelength of 542 nm, the calibration curve over the range 0-400 µg/L exhibits a perfect linear relationship with a correlation coefficient R=1.000.

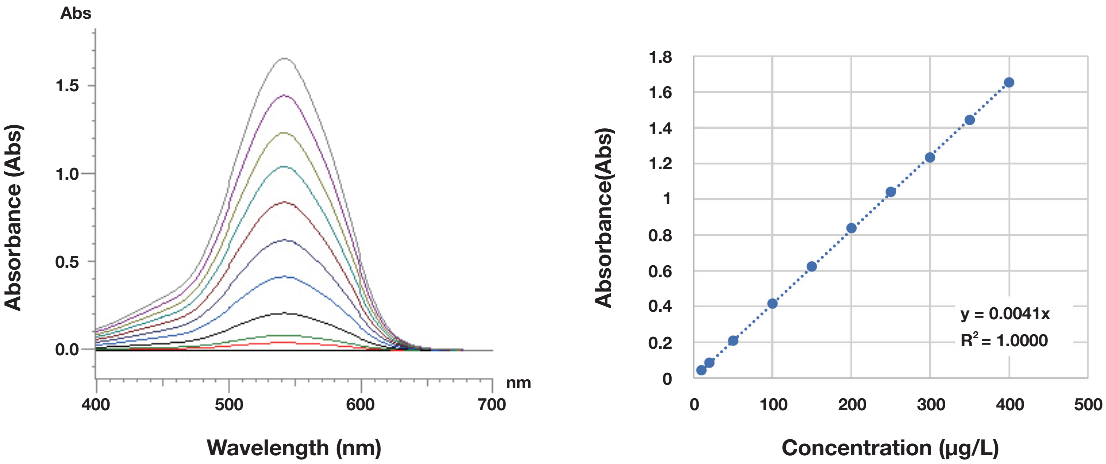

Fig. 7 Results of hexavalent-chromium measurements using a 50 mm cell.

3-2. Measuring DNA: UV absorption

DNA exhibits an absorption peak at 260 nm, and the DNA concentration of a specimen may be determined by measuring the absorbance at this wavelength. This allows the use of spectrophotometers for quantitative analysis of DNA extracted from test bodies. Figure 8 shows absorption spectra for specimens prepared with various lambda-DNA concentrations (left) and a calibration curve for quantitative analysis (right), measured using a 50 µL cell. We obtain high-quality spectra with absorption peaks near 260 nm. For measurement of trace specimens, the optional *micro-sample cell* may be used to measure specimen volumes as small as 1.5 µL.

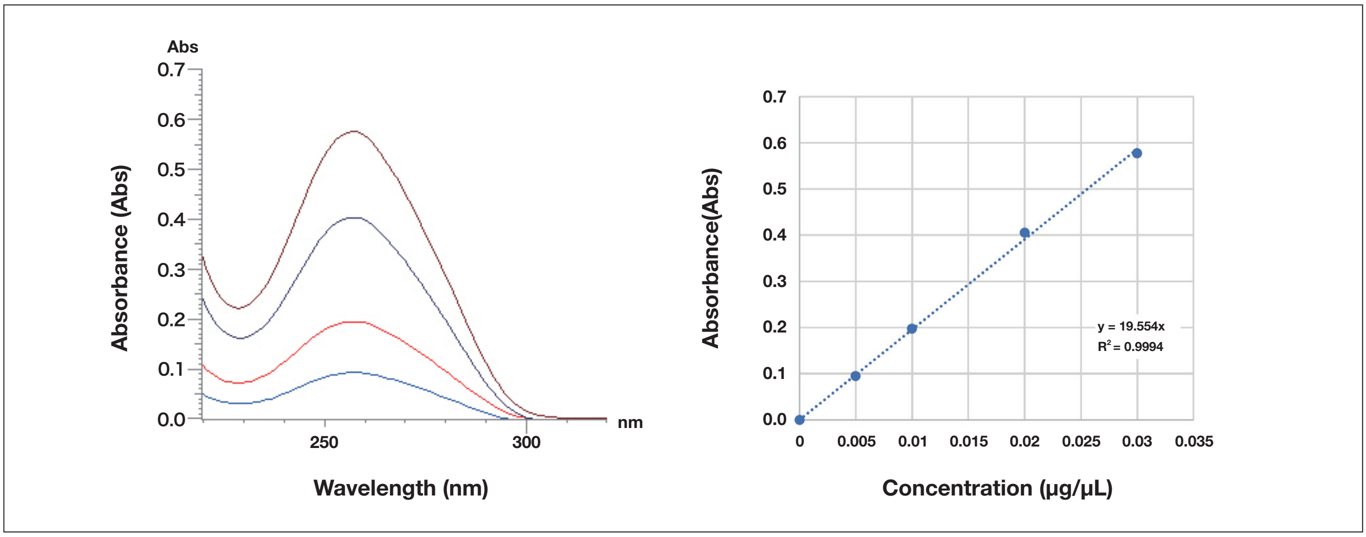

Fig. 8 Measurements of lambda-DNA

4. Conclusions

In this article we surveyed key features of the UH5200 spectrophotometer series and presented measurement examples to illustrate its capabilities. The UH5200 series is a new product line designed for reliability and ease of use, and we expect it to prove useful in a wide range of fields.

About the author

Jun Horigome
Global Sales Planning Dept.
Beam Technology & Analytical Systems Business Div.
Core Technology & Solutions Business Group
Hitachi High-Tech Corporation

Features and Applications of the Automatic Particle Search Function for the Hitachi HT7800 120 kV TEM System

Akiko Wakui*[1], Yasuyuki Nodera*[2]

1. Introduction

When performing transmission electron microscopy (TEM) observations of samples, searching for target samples in the field of view is a particularly time-consuming task. Operators often miss a target sample when viewing samples with which they are unfamiliar or lack experience observing. This is especially true when searching for virus particles in the field of view. The Hitachi Bio-TEM series was designed to overcome these challenges. The company developed a system for automatic detection for this series of TEM instruments. The system is used on negatively stained samples that contain large amounts of impurities and items similar to the target virus, which it automatically detects.[1)] The Hitachi HT7800 120 kV TEM system, which is the latest model in the series, uses a suited-to-purpose digital camera to facilitate the series of tasks from observation to image acquisition.

The automatic particle search function of the HT7800 uses matching techniques and other new technologies to identify target viruses more precisely.[2)] This paper discusses the features and some applications of this new automatic particle search function.

2. Overview of the HT7800 120 kV Transmission Electron Microscope

The HT7800 features a maximum accelerating voltage of 120 kV and a proprietary compound objective lens. Offering both wide-field, high-contrast observations in high-contrast mode and high-resolution observation in high-resolution mode,[3)] the microscope is used in fields spanning from biomedicine to nanomaterials (Figure 1). The HT7800's high-sensitivity screen camera for fluorescence observation enables observation of images of unstained samples barely perceptible to the naked eye and samples susceptible to electron beam damage, such as ice-embedded samples. The accelerating voltage can be adjusted from 20 to 120 kV to suit the sample being observed. The HT7800 also features an image navigation function that automatically images predefined locations as well as auto-focus and drift-correction functions that simplify operation.[4)]

Fig. 1 Exterior of the Hitachi HT7800 120 kV TEM system.

3. Features of the HT7800 Automatic Particle Search Function

The operating procedure for the automatic particle search function is illustrated in Figure 2. Once started, the function automatically moves the sample stage and assesses whether any target particles are present in the field of view. The function automatically records an image if particles are present or proceeds to the next field of view if no particles are present. An identification number is assigned to each particle identified in images with particles present.

Template matching is used in the automatic particle search function of the HT7800. Adjusting individual parameters allows the operator to increase particle hit rates and allows its use with certain samples that are not negatively stained.

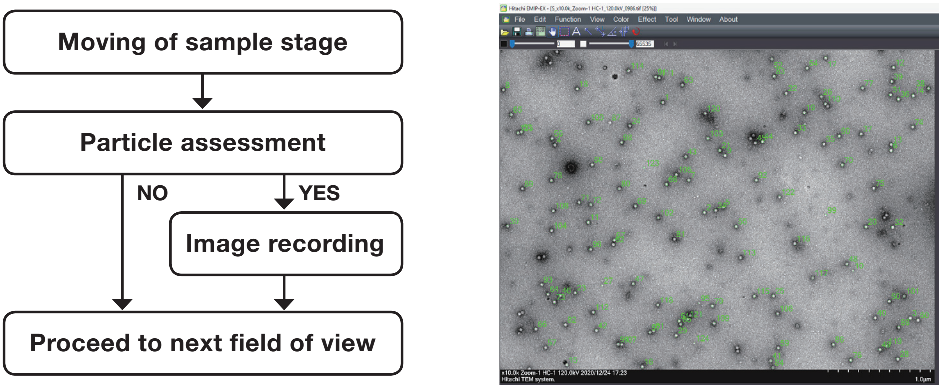

Flowchart for automatic particle search function

Image showing identified particles (This image was produced from a negatively stained sample.)

Fig. 2 Procedure for using automatic particle search function.

4. Applications of the HT7800 Automatic Particle Search Function

4-1. Negatively stained norovirus

This study used norovirus extracted from a human stool sample. A sample suspension was applied dropwise to a 400-mesh grid with a carbon-reinforced collodion film and then negatively stained with 2% uranyl acetate. The automatic particle search function performed at an accelerating voltage of 100 kV and magnification of 20,000 × produced 36 images. The results are shown in Figure 3. Since an identification number is assigned to each norovirus particle detected in the automatically captured images (Figure 3(a)), quantitative analysis of individual particles is possible. The particle diameters and areas measured in the sample using Image Pro Premier 2D image analysis software (Media Cybernetics Inc.) are shown in Figure 3(b). The mean particle size for all detected norovirus particles and a distribution of the particle diameters can also be determined. Quantitative analysis of 4096 norovirus particles detected in this study revealed a mean particle size of 25.2 nm and a mean area of 532.3 nm^2. A size distribution of the norovirus particles is shown in Figure 3(c). The distribution shows that 48% of the norovirus particles had diameters from 24 to 26 nm.

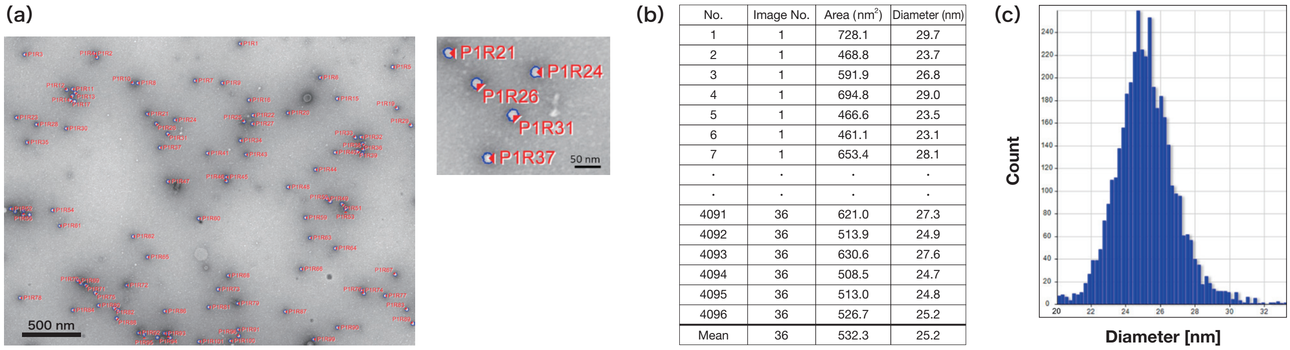

No.	Image No.	Area (nm^2)	Diameter (nm)
1	1	728.1	29.7
2	1	468.8	23.7
3	1	591.9	26.8
4	1	694.8	29.0
5	1	466.6	23.5
6	1	461.1	23.1
7	1	653.4	28.1
.	.	.	.
.	.	.	.
4091	36	621.0	27.3
4092	36	513.9	24.9
4093	36	630.6	27.6
4094	36	508.5	24.7
4095	36	513.0	24.8
4096	36	526.7	25.2
Mean	36	532.3	25.2

Fig. 3 Analysis of negatively stained norovirus by automatic particle search function.
(a) Particle image analysis, (b) quantitative analysis, (c) particle size distribution

4-2. Coronavirus in resin-embedded tissue sections

The automatic particle search function of the HT7800 uses template matching. Individual template matching parameters were adjusted in an attempt to enable automatic detection of a given type of virus particle in complex tissue.

Rat cerebral cortex stained with a coronavirus (porcine hemagglutinating encephalomyelitis virus) was used as a sample. The sample was fixed with aldehyde fixing fluid and osmium tetroxide, serially dehydrated in ethanol, and embedded in an epoxy resin. The resulting sample blocks were then cut into 80-nm ultra-thin sections with an ultramicrotome. The ultra-thin sections were subjected to electronic staining with lead citrate and uranyl acetate and then observed by TEM at an accelerating voltage of 100 kV. Transmission electron micrographs of this porcine coronavirus cerebral cortex-stained sample are shown in Figure 4. One reveals an electron-dense vesicular structure in cytoplasm rich with cellular organelles such as a nucleus (N) and mitochondria (M) (Figure 4(a)). A magnified view of this image shows viral cross sections measuring 50 to 90 nm in diameter (Figure 4(b)). The automatic particle search function was used on these virus particles.

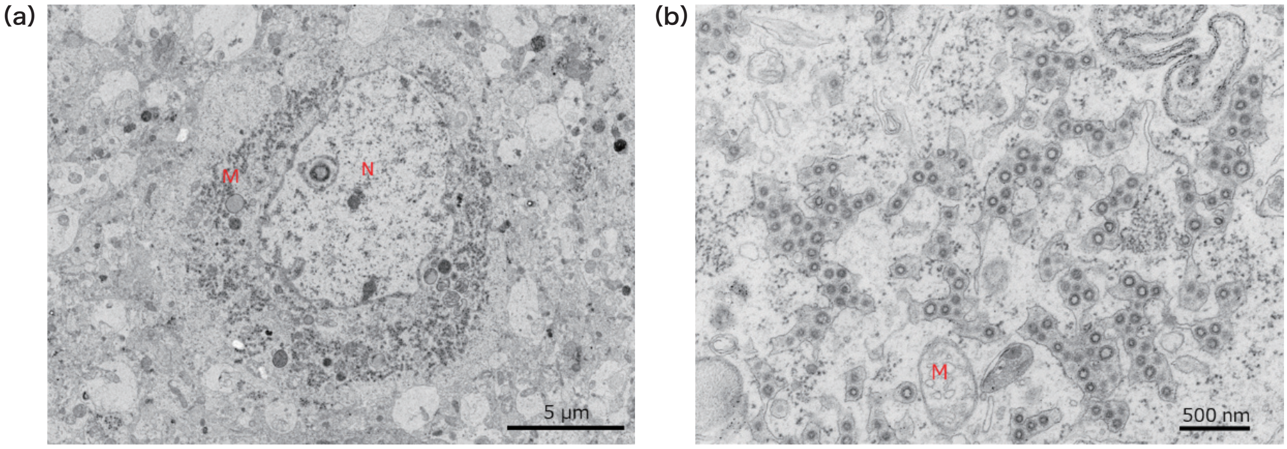

Fig. 4 Transmission electron micrographs of resin-embedded ultra-thin section of rat cerebral cortex stained with porcine coronavirus. (a) 2500× magnification, (b) 15,000× magnification (accelerating voltage: 100 kV, N: nucleus, M: mitochondrion)

Verification of parameters

The parameters for the automatic particle search function are listed in Table 1. The parameters are set to default values experimentally determined using standard samples. For analysis of the field of view shown in Figure 5, the parameters were optimized for 90-nm coronavirus particles. This field of view is known to contain 94 virus particles. The parameters were adjusted and optimized to maximize the hit rate* of the automatic particle search function.

*Hit rate: (Number of hits / (total number of virus particles (94)) × 100

Table 1 Description of parameters

Parameter	Description	Default value
Template rate (%)	The size of the template used in template matching.	147
Search range (%)	The range of particle sizes searched.	0
Matching rate (%)	The threshold of the accuracy rate during particle searches. Only particles with a correlation equal to or greater than the matching rate are assessed as target particles.	50
Area rate (%)	The threshold used when area assessments are added to the particles.	50
Set Search step	The number of matching steps in the range of particle sizes searched as configured in “search range.”	3
Optimal size search	If optimal size search is turned on, the mean template size for the leading 10 search correlation values is first calculated. Then the search is repeated using a template of that size.	ON

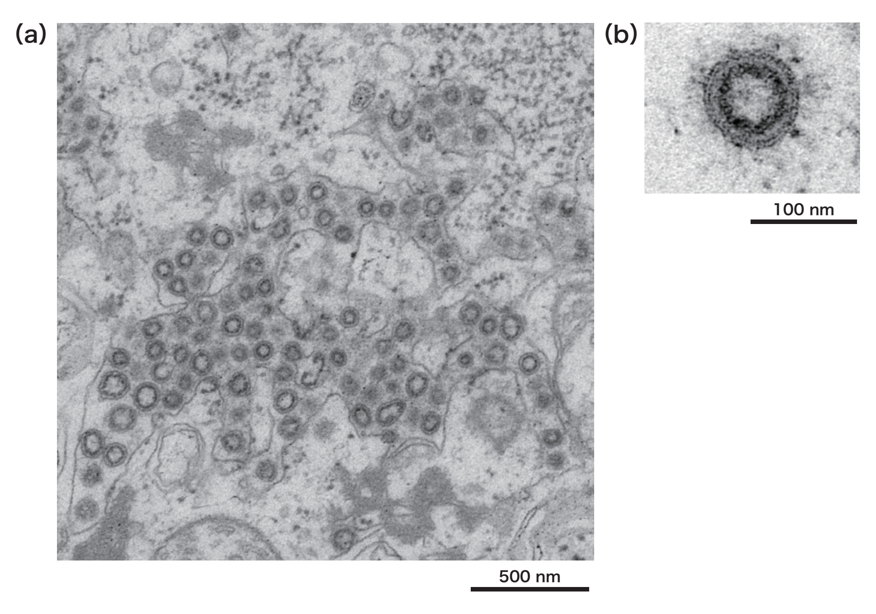

Fig. 5 Transmission electron micrograph of porcine coronavirus-stained rat cerebral cortex used to verify parameters.
(accelerating voltage: 100 kV, 10,000× magnification)

The results of verification of the search range and search steps are shown in Tables 2 and 3. The search range is a parameter for setting the particle size range. For a search range of 30% and a particle size of 90 nm, particles measuring from 63 to 117 nm are detected. As shown in Table 2, the hit rate for the default of 0% was 39%, while the hit rate increased to 66% for search ranges of 30% and 40%. A search range of 50% resulted in the highest number of detections at 81, but many misidentifications meant the hit rate was 49%. This is because a search range of 50% results in template matching from 45 to 135 nm.

Table 2 Verification of search range

Search range(%)	0	10	20	30	40	50
Particles detected	39	54	63	67	67	81
Hits	37	51	60	62	62	46
Hit rate (%)	39	54	64	66	66	49

(Default: 0%)

Search steps represent the number of steps used for matching the size of the target particle. A greater number of steps means a higher number of matches. Hit rates were determined for 3, 5, 7, and 9 search steps. Verification was performed with a search range of 30% and automatic particle searching. As shown in Table 3, the default of 3 search steps resulted in a hit rate of 66%, while 9 search steps produced the highest hit rate of 74%. The virus particles in the sample used were cross sections and therefore had a range of sizes. This verification showed that in such samples with large particle size variance, using a larger number of search steps produces more matches.

Table 3 Verification of number of search steps

Search step	3	5	7	9
Particles detected	67	71	75	76
Hits	62	66	69	70
Hit rate (%)	66	70	73	74

(Default: 3, search range of 30%)

Application

A micrograph produced by applying these optimized parameters is shown in Figure 6. Figure 6(a) shows automatically identified coronavirus particles that have been identified with a number. This demonstrates that the search function can automatically identify the target coronavirus against a complex background. The particle size distribution determined in a particle analysis of the detected coronavirus particles shows the variance in their sizes (Figure 6(b)). This large variance is attributable to the particles in the tissue section appearing as a variety of cross sections due to microtoming. Operators working with samples containing a range of particle sizes like this one are urged to optimize the search parameters so that the search function can detect the target particles with high precision and thereby improve the efficiency of TEM analysis.

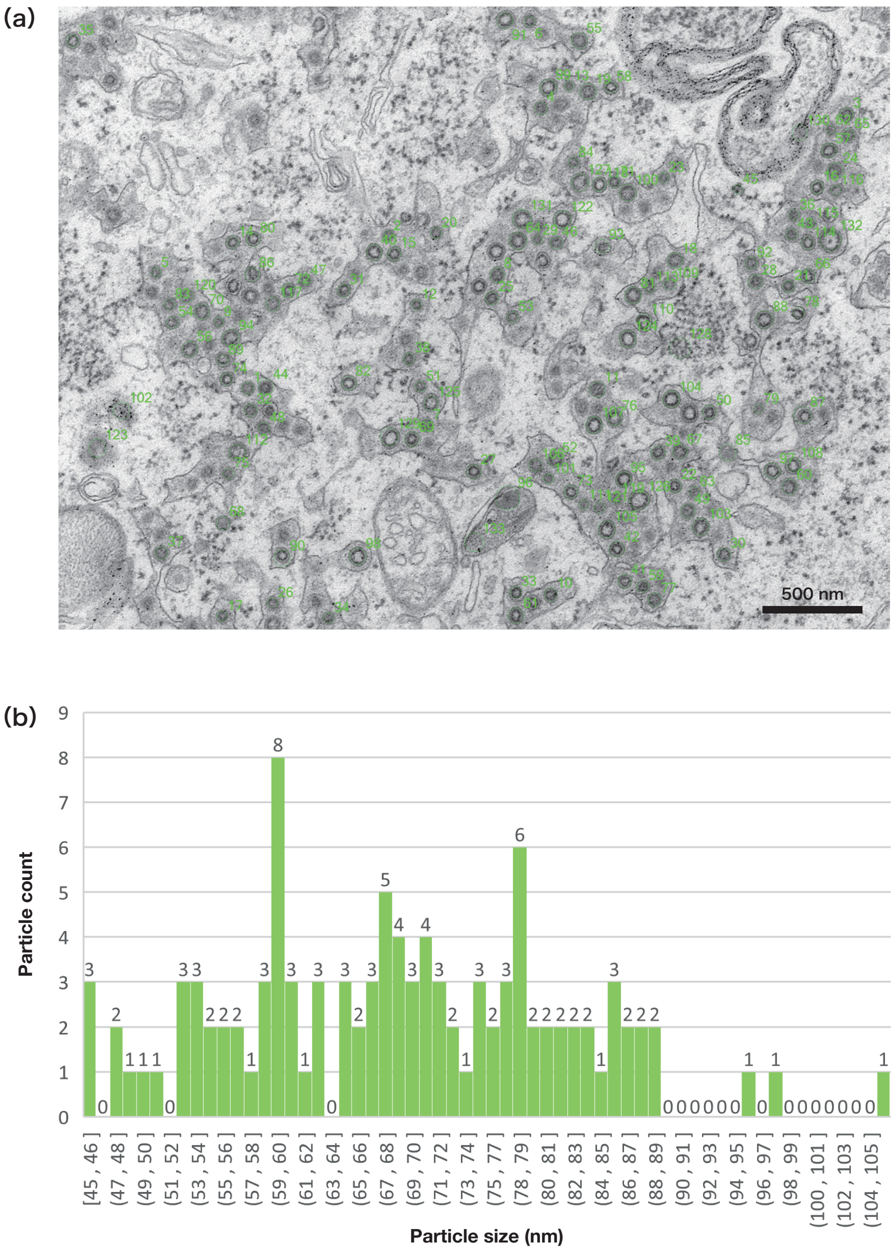

Fig. 6 Automatically detected particles in resin-embedded ultra-thin section of rat cerebral cortex stained with porcine coronavirus.
(a) Image produced by automatic particle search function (accelerating voltage: 100 kV, 15,000× magnification), (b) particle size distribution

5. Conclusions

This paper described the features and some applications of the automatic particle search function of the HT7800 TEM system. As has been discussed, the search function precisely detects the target particles in negatively stained samples and resin-embedded ultra-thin sections of tissue. TEM operators will benefit from better work efficiency and be able to precisely identify target particles with few if any misses.

References

1) Etsuko T. Utagawa *et al.*, *Journal of Virological Methods*, **100**, 49-56 (2002).

2) Kawamoto *et al.*, Electron Microscopy Technology for Medicine and Biology, Proceedings of the 38th Technical Conference, p. 50 (2022). (in Japanese)

3) Keiji Tamura *et al.*, Japanese Society of Microscopy, Proceedings of the 74th Annual Meeting, p. 4 (2018). (in Japanese)

4) Toshie Yaguchi *et al.*, Japanese Society of Microscopy, Proceedings of the 74th Annual Meeting, p. 35 (2018). (in Japanese)

Acknowledgments

We sincerely thank Dr. Etsuko Utagawa, Visiting Researcher, National Institute of Infectious Diseases and President, Science Lab. Yokohama, for providing the norovirus samples we used.

We also deeply thank Dr. Kinji Ishida, Institute for Biomedical Sciences, Iwate Medical University and Dr. Norio Hirano, formerly of the Department of Veterinary Microbiology, Faculty of Agriculture, Iwate University, for providing samples of rat cerebral cortex stained with coronavirus (porcine hemagglutinating encephalomyelitis virus). We are grateful for their kind contributions.

About the authors

*[1] Akiko Wakui
Solution Development Dept.
Beam Technology & Analytical Systems Product Div.
Core Technology & Solutions Business Group
Hitachi High-Tech Corporation

*[2] Yasuyuki Nodera
Software Design Dept.
Beam Technology & Analytical Systems Product Div.
Core Technology & Solutions Business Group
Hitachi High-Tech Corporation

SCIENTIFIC INSTRUMENT NEWS
2024 Vol.21 MARCH
Technical magazine of Electron Microscope and Analytical Instruments.
Technical Explanation

The Ion Milling Method with Improved Work Efficiency

Yuki Inagi

1. Introduction

Ion milling is a technique for preparing cross-sectional sample for observation via scanning-electron microscopy (SEM). The ease with which this approach can produce cross-sectional surface—without applying stress to the sample—has made it a widely-used tool in many fields of science and engineering, from semiconductor research to electronics and material science. In recent years, the increasing complexity of the sample structures observed by SEM, together with growing demand for streamlined workflows and improved operational efficiency, have created a need for sample-preparation techniques capable of handling a diverse variety of samples—while reducing the time required to prepare samples for observation.

Two varieties of ion milling are commonly used to prepare SEM samples: *cross-section ion milling and flat ion milling.*1) Hitachi High-Tech offers two hybrid ion-milling systems—the ArBlade5000 and the IM4000II, shown in Figure 1—with both systems supporting both types of milling. In this article, we first survey the basic principles of ion milling, then discuss the capabilities of Hitachi's newest ion-milling systems and present a number of illustrative applications.

Fig. 1 IM4000II (left) and ArBlade5000 (right) ion-milling systems.

2. Overview of Ion Milling

Ion milling exploits the phenomenon of *sputtering*—in which a sample is irradiated by a broad, unfocused ion beam from an ion gun, causing atoms to be ejected from the sample surface—to yield observation surfaces that are smooth over length scales on the order of millimeters.2) In general, argon gas, which induces minimal chemical transformation for most samples, is used as the ion source.

2-1. Cross-section ion milling

In cross-section milling, as shown in Figure 2, the ion beam is partially obstructed by a beam-blocking slab (known as a *mask*) placed between the ion gun and the sample, so that only the portion of the sample extending beyond the mask is irradiated. In this case, sputtering proceeds along the edge of the mask, removing the exposed portion of the sample and leaving behind a smooth cross-sectional surface. Typically, the sample is positioned with 10-100 µm of its length extending beyond the mask, and the sample holder is rotated over a swing angle of ±15-40° to avoid inducing line defects.

In general, cross-section milling is an effective tool for preparing observation-ready cross sections of samples that are difficult to polish mechanically, including hybrid samples comprising multiple distinct materials or fragile samples incorporating large numbers of voids.

The effectiveness of cross-section milling is illustrated by Figure 3, which shows cross-sectional surfaces of a thermal-paper sample prepared for SEM observation by (a) cutting with a razor blade and (b) cross-section milling. The structure of thermal-paper consists of multiple material layers—including heat-sensitive layers and protective layers—stacked atop a base paper material; in Figure 3(a) it can be seen that the stress exerted on the sample by razor-blade cutting has collapsed the various material layers, preventing accurate SEM observation of the layer structure. In contrast, Figure 3(b) shows that the ability of cross-section milling to prepare cross-sectional surfaces *without* subjecting samples to stress has preserved the layer structure of the thermal-paper, allowing precise observation of layer thicknesses and the dispersion of filler material.

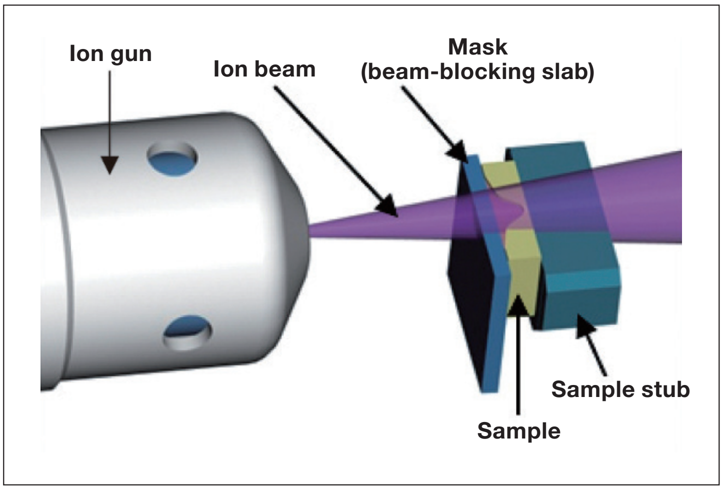

Fig. 2 **Schematic depiction of cross-section milling.**

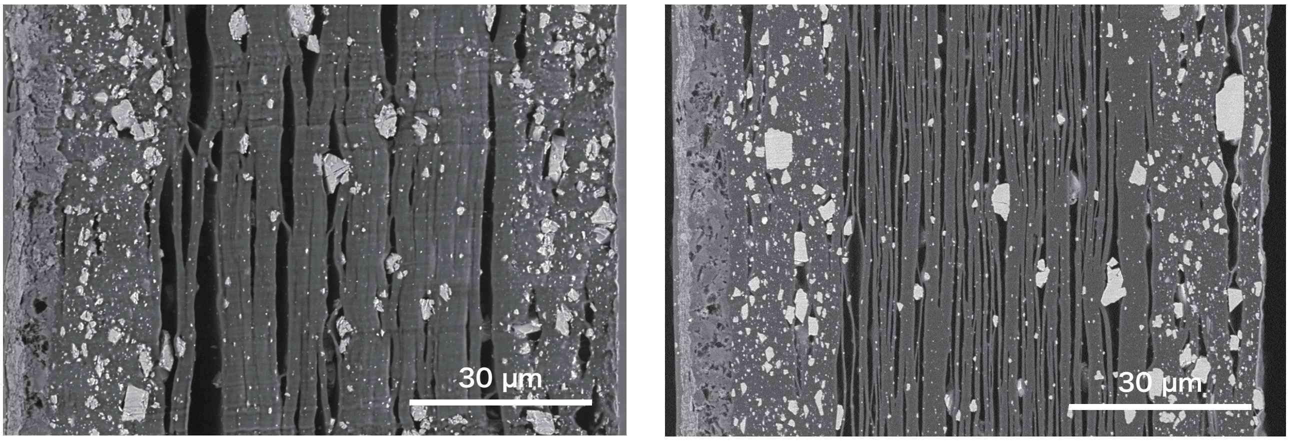

(a) Cutting by razor blade

(b) Cross-section milling

Fig. 3 **Cross-sectional SEM images of thermal-paper.**

2-2. Flat ion milling

In flat ion milling (or simply *flat milling*), illustrated in Figure 4, a broad ion beam is trained on a sample surface at a given angle of incidence, allowing large areas of samples to be processed simultaneously. The incidence angle θ may be set anywhere between 0 and 90 degrees; for incidence angles above 80°, the ion beam is nearly parallel to the sample surface, yielding a smooth processed surface and minimizing surface roughness due to variations in etching rate for regions of differing crystal orientation or material composition. This approach is used to eliminate abrasion defects induced by machine polishing of resin-embedded samples. On the other hand, selecting low incidence angles below 45° has the effect of accentuating surface protrusions and indentations due to differences in etching rate; this is useful for purposes such as characterizing the distribution of particles or material grains throughout a sample.

Figure 5 shows SEM images of (a) a mechanically-polished surface of a copper plate, and (b) a surface of the same plate that was subjected to flat milling after mechanical polishing. For the sample prepared by mechanical polishing alone, it can be seen in Figure 5(a) that crystal grains are difficult to observe due to residual polishing defects and strain effects. In contrast, Figure 5(b) shows that the flat milling step eliminates polishing defects and stress-induced distortion layers, allowing clear observation of crystal grains.

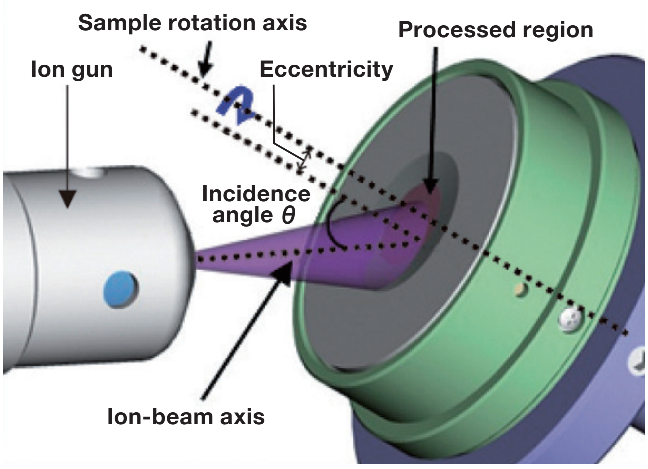

Fig. 4 Schematic depiction of flat milling.

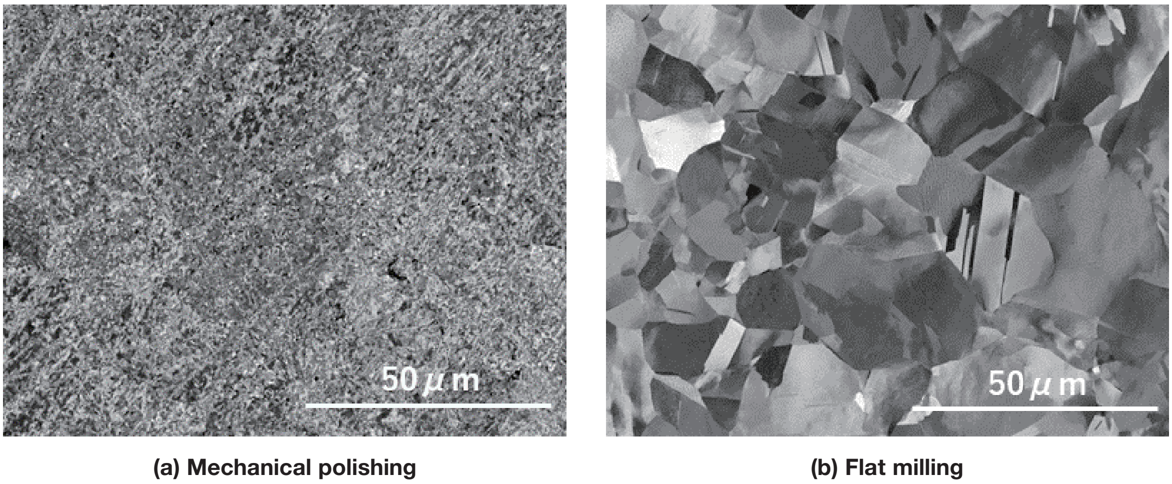

(a) Mechanical polishing

(b) Flat milling

Fig. 5 Cross-sectional SEM images of copper-plate.

3. Key Features of IM4000II and ArBlade5000 Ion-milling Systems

3-1. Features common to both systems

The ion-milling systems offered by Hitachi High-Tech are *hybrid* systems supporting both cross-section milling and flat milling, making them useful for a broad spectrum of applications involving a wide variety of materials. These systems are easily controlled through simple touch-panel interfaces. The range of samples that can be processed by these systems can be further extended by the addition of various optional capabilities, including a cooling mechanism—in which polymeric materials and other samples with low melting points are cooled during the ion-milling process to avoid thermal damage from ion-beam irradiation—and an air protection mechanism for analyzing samples such as lithium-ion battery materials without exposure to the ambient environment.

To illustrate the usefulness of sample cooling, Figure 6 shows the results of cross-sectional processing of a low-melting-point solder sample (a) without cooling (i.e., at room temperature) and (b) with cooling.[3] The sample is cooled indirectly using liquid nitrogen and may be maintained at an arbitrary user-specified temperature in the range 0 to −100°C. For the sample processed without cooling, heating due to ion-beam irradiation results in melting of Pb—a metal with a low melting point—yielding the void regions visible in Figure 6(a). In contrast, sample cooling during the milling process restricts the increase in sample temperature, yielding the smooth, defect-free cross-sectional surface shown in Figure 6(b).

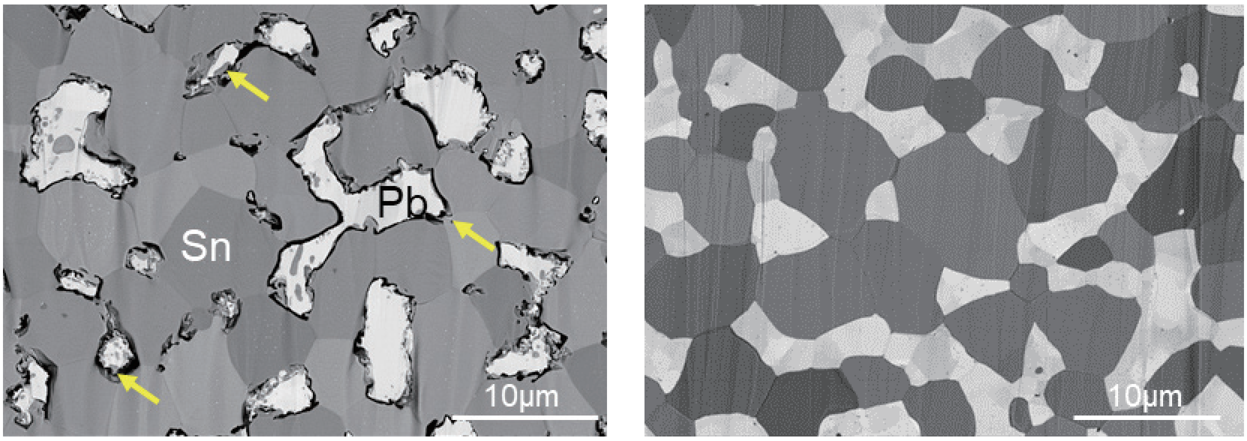

(a) Ion milling at room temperature (without sample cooling)

(b) Ion milling with sample cooling

Fig. 6 Cross-sectional SEM images of low-melting-point solder.

For processing samples such as battery materials—which, when exposed to ambient environments, suffer significant shape distortion due to reactions with the oxygen and water present in air—it is convenient to perform ion milling using a hermetically-sealable air protection sample holder. This allows processed cross-sectional surfaces to be analyzed via SEM or atomic-force microscopy (AFM) without exposing samples to the ambient environment. To illustrate the usefulness of this capability, Figure 7(a) shows a SEM image of a lithium-ion battery anode material processed by cross-section ion milling and then transported to the SEM using the air protection mechanism, while Figure 7(b) shows a SEM image of the same sample after environmental exposure.[4] For the air protection sample, Figure 7(a) clearly shows the distribution of conduction-assisting agents surrounding graphite. In contrast, in Figure 7(b) it can be seen that, after exposure to the ambient environment, the sample surface is covered by deposits resulting from contact with oxygen and water.

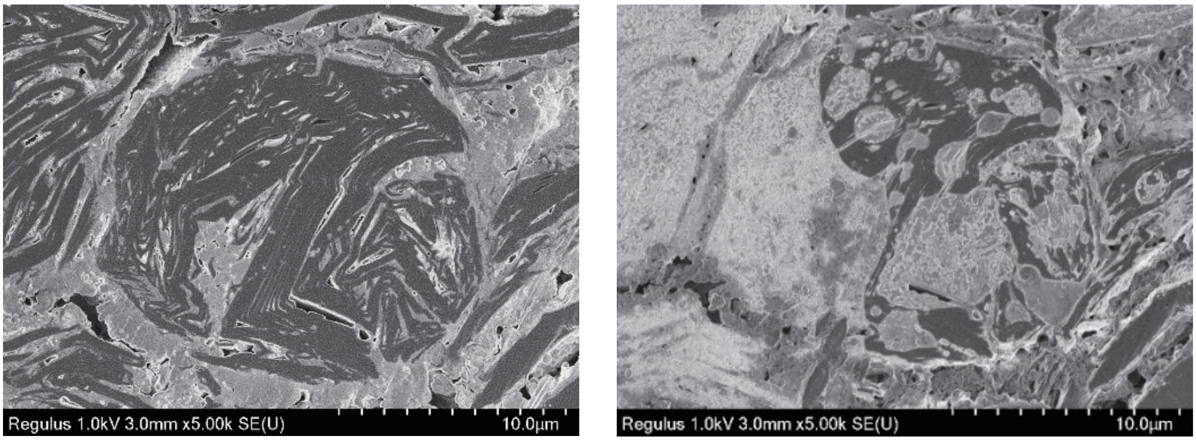

(a) Air protection sample

(b) Same sample after exposure to environment

Fig. 7 Cross-sectional SEM images of lithium-ion battery anode.

3-2. Highly efficient sample processing with ArBlade5000

Conventional cross-section milling systems are capable of processing sample regions with widths of approximately 1 mm. In contrast, the ArBlade5000 boasts wide-area cross-section milling capability that allows preparation of cross-sectional surfaces with widths as large as 8 mm. With this capability, a single processing step suffices to prepare smooth cross-sectional surfaces for samples that would require multiple steps with conventional systems, increasing operational efficiency. Figure 8 shows SEM images and energy-dispersive X-ray (EDX) data for a cross-sectional surface of an ultra-hard drill-bit sample processed using the wide-area cross-section milling capability of the ArBlade5000.[5)] Figures 8(a) and 8(b) respectively show the entire processed surface and an enlarged region of the coating layer, while Figure 8(c) is an EDX map of the enlarged region. The large 8 mm processing range of the ArBlade5000 allowed the entire milling procedure to be completed in 5 hours, demonstrating the ability of this system to prepare large cross-sectional surfaces rapidly via high-throughput processing—even for ultra-hard materials that are difficult to polish. The enlarged image of the surface coating layer reveals a structure consisting of a stack of ultra-thin layers with thicknesses below 50 nm, while the EDX map indicates that this layer stack contains aluminum and titanium. This example demonstrates that wide-area cross-section milling using the ArBlade5000 can yield high-quality cross-sectional surfaces allowing high-magnification observation and analysis.

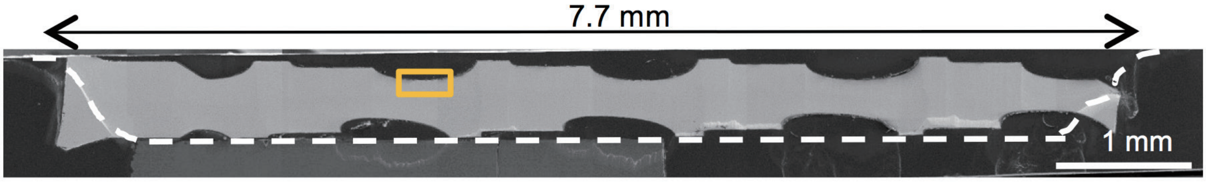

(a) Full sample region processed by wide-area cross-section milling

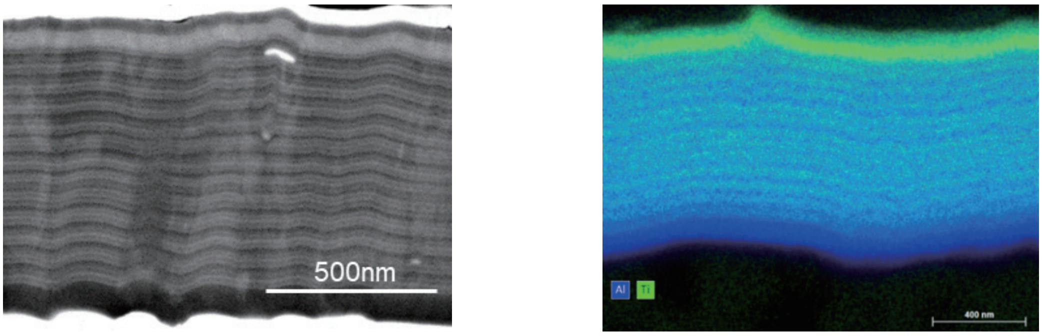

(b) Enlarged region of coating layer (c) EDX mapping image (blue: aluminum, green: titanium)

Fig. 8 SEM and EDX images of ultra-hard drill-bit sample prepared for observation by wide-area cross-section milling.

Connecting the ArBlade5000 to a PC allows the system to be controlled by the Advance Control Software (ACS) package, which can transmit and receive processing conditions and compile arbitrary sequences of milling steps to be saved and executed at will. Using the ACS also has the advantage of allowing samples to be processed at multiple sites and under multiple sets of milling conditions. The effectiveness of this capability is demonstrated by Figure 9, an optical microscopy image of an electronic circuit board prepared for observation via ACS multi-site processing. Processing this entire sample via wide-area cross-section milling would be extremely time-consuming, but ACS multi-site processing targets only those sample subregions that require preparation for observation—and processes those subregions under milling conditions optimized for the sample in question—thus preparing cross-sectional surfaces at desired observation sites in just a few hours. Because the system can process samples automatically under arbitrary pre-specified milling conditions, instrument operators are freed from any need to attend to the system until the full processing sequence is complete, reducing processing times and improving operational efficiency.

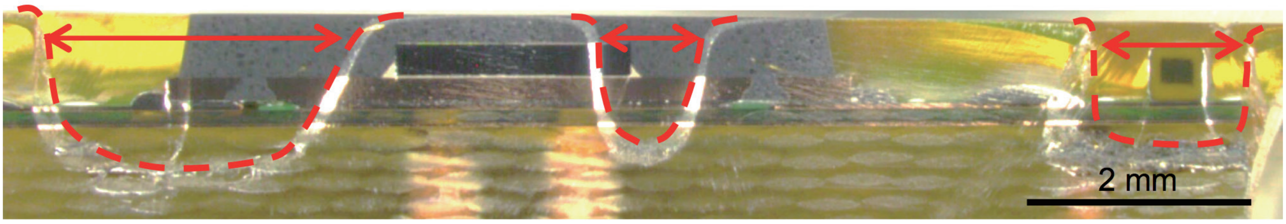

Fig. 9 Optical microscopy image of electronic circuit board sample prepared for observation using multi-site processing capabilities of ACS.

The capabilities of the ACS, when used together with a newly-developed multi-sample holder, allow as many as 3 test samples to be processed in a single milling operation, with milling conditions specified separately for each sample. This reduces the burdensome operations of pumping to achieve a high vacuum and venting to the ambient environment, allowing fully-automated operation of all steps needed to complete the processing of multiple samples—and freeing instrument operators to attend to other tasks while the milling procedure is in progress.

The multi-sample holder, shown in Figure 10, uses spring-loaded sample mounts to hold samples in place via spring action, eliminating any need for hot waxes or pastes.

The usefulness of the multi-sample holder is illustrated by the example in Figure 11, in which the multi-sample holder was used to process three types of test samples: (1) an electronic circuit board, (2) a metal plate with a coating layer, and (3) a thermal-paper sample. Milling conditions were configured separately for each sample; for example, the circuit board and the metal plate were milled for short times at high accelerating voltages, while the thermal-paper was milled at low accelerating voltage to minimize damage due to ion-beam irradiation. Each sample was subjected to a specific sequence of milling steps, including multi-site processing and wide-area cross-sectional processing for the electronic circuit board, for example, both edges were processed, and a region with a width of 3 mm near the left edge was processed via wide-area milling. This example demonstrates the ability of the multi-sample holder to automate complex multi-site milling procedures involving multiple samples, offering significant improvements in operational efficiency.

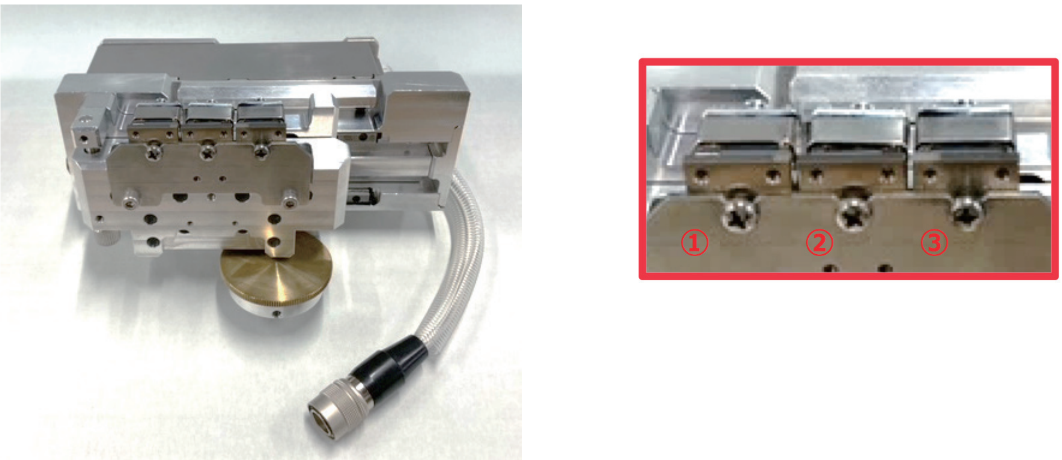

Fig. 10 Multi-sample holder (left) and enlarged view of spring-loaded sample mounts (right).

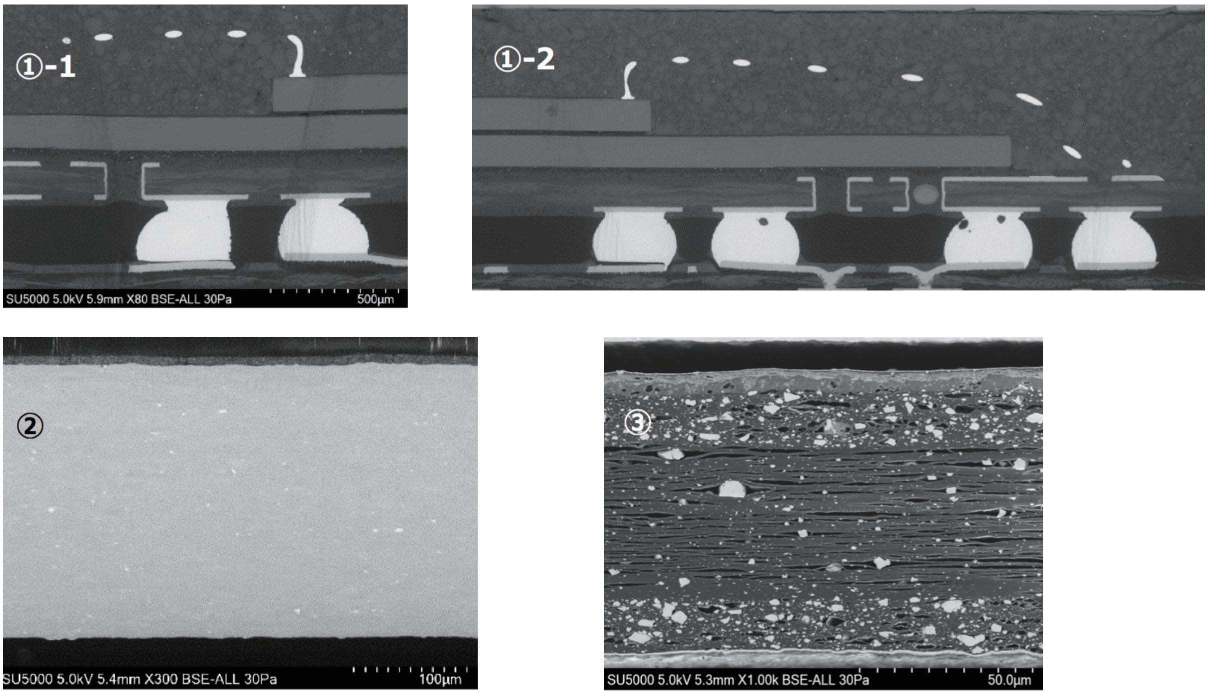

Fig. 11 Multi-sample holder allows one-step processing of multiple test samples: (1) electronic circuit board, (2) metal plate with coating layer, and (3) thermal-paper sample.

4. Conclusions

Ion-milling systems, augmented by sample-cooling and air protection capabilities, allow preparation of cross-sectional observation surfaces for a vast range of samples. The high-throughput operation of Hitachi High-Tech's milling systems reduces the time needed to process samples, while multi-site processing and the multi-sample holder can automate the preparation of cross-sectional surfaces at multiple sites on multiple samples, increasing operational efficiency. These features significantly streamline the preprocessing of SEM observation samples.

References

1) Japanese Society of Microscopy, Kanto Branch, *Scanning Electron Microscopy* (*New Edition*), Kyoritsu Shuppan Co., Ltd., 195 (2011) (in Japanese).

2) Masao Hirasaka and Kentaro Asakura, *Q&A on FIB and Ion Milling Techniques*, Agne Shofusha, 8 (2002) (in Japanese).

3) S.I.navi (Hitachi High-Tech Membership Site), Application Datasheet HTD-SEM-202

4) S.I.navi (Hitachi High-Tech Membership Site), Application Datasheet HTD-SEM-124

5) S.I.navi (Hitachi High-Tech Membership Site), Application Datasheet HTD-SEM-025

About the author

Yuki Inagi
Surface Structure Analysis Group
Solutions Development Department
Beam Technology & Analytical System Products Division
Core Technology & Solutions Business Group
Hitachi High-Tech Corporation

SCIENTIFIC INSTRUMENT NEWS
2024 Vol.21 MARCH
Technical magazine of Electron Microscope and Analytical Instruments.
Technical Explanation
2024 Vol.21

Thermal Analyzer Differential Scanning Calorimeter NEXTA® DSC Series

Shinya Nishimura

1. Introduction

Differential scanning calorimetry (DSC) is a method of thermal analysis that allows observation of various physical transitions in materials—including melting and fusion, glass transition, crystallization, and thermosetting—as well as measurement of physical properties such as the specific heat and purity from analysis of the thermal history. These capabilities make DSC an essential tool for analyzing the thermal behavior of materials, and the technique is widely used both in Japan and around the world for research, development, and quality control in fields such as polymeric materials, inorganic materials, pharmaceuticals, and petroleum chemistry.

Since the 1970s, Hitachi High-Tech has been developing proprietary heat-flux DSC systems and marketing them around the world. In 2020, Hitachi High-Tech released two instruments in its NEXTA DSC series of next-generation thermal analyzers: the standard-model DSC200 system and the high-end DSC600 system.

Fig. 1 The DSC600 differential scanning calorimeter thermal analysis system.

2. Overview of the NEXTA® DSC Series

In recent years, the growing trends toward hybridization and high functionality of materials and material constituents have created increasingly diverse, increasingly complex demands for thermal analyzers capable of characterizing the thermal properties of materials—and, specifically, how the functional properties and effects of various materials vary with changing temperature—from researchers in many fields of science and engineering, from basic research to product development. Defect analysis for electronic products—which are constantly increasing in performance while shrinking in size—requires analyzing, and identifying the constituents of, minuscule samples containing only trace quantities of materials. This demands high-sensitivity instruments capable of high-precision measurements and high baseline performance to enable stable, reproducible measurements. High baseline performance is also a key prerequisite for accurately measuring the thermal properties of polymers, including the highly-functional polymer materials and films used in the automobile and aerospace industries and many other fields.

The NEXTA® DSC series of instruments offers three key features to meet these challenging market needs: (1) high measurement sensitivity, (2) stable baseline reproducibility, and (3) the Real View unit for observing samples at low temperatures.

3. High Measurement Sensitivity

The basic temperature sensor used to detect differential heat signals in DSC measurements is the *thermocouple*. Multiple thermocouples may be connected in series to yield a compound detector known as a *thermopile*. The NEXTA® DSC600 features a proprietary Hitachi-developed thermopile DSC sensor capable of high-precision measurements with a sensitivity below 0.1 μW, enabling accurate measurements of challenging samples such as blended resin materials or trace quantities of additives within parent materials.

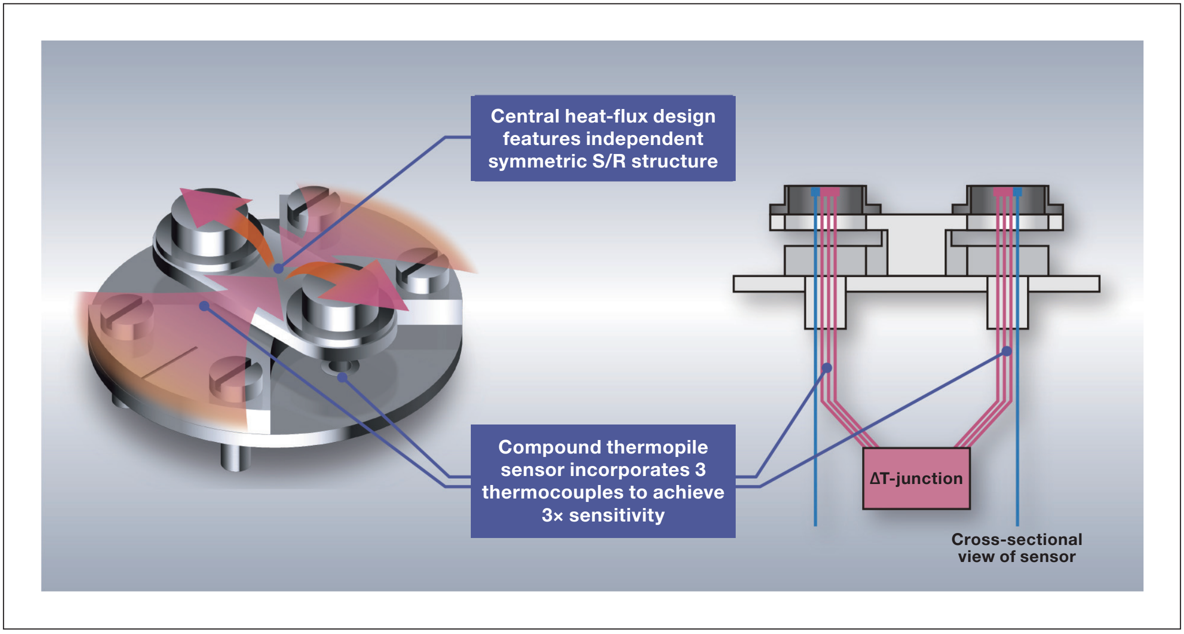

Fig. 2 Structure of the DSC sensor in the DSC600 system

The high measurement sensitivity of the DSC600 is demonstrated by an application case study involving high-sensitivity measurements of a carbon-fiber-reinforced epoxy resin used as a structural material for automobiles and aircraft. This material is an epoxy resin produced by adding carbon fibers to a resin material for increased mechanical strength. Because the resin fraction of the resulting material is lower than that of pure epoxy resin, accurate detection of its glass transition and exothermic peaks requires high measurement sensitivity and baseline stability.

To begin, Figure 3 shows the results of DSC measurements heated at a constant rate. The DSC curve for the first measurement run indicates a glass transition in the range 50-60°C.

On the other hand, looking at the portion of the curve above 100°C we see features that may be suggestive of a endothermic peak at 126.7°C and of a thermosetting exothermic peak at 150.8°C—but the data are difficult to interpret.

When faced with ambiguous measurement data of this sort, one strategy for reaching accurate conclusions is *temperature-modulated DSC*, in which the heating profile is periodically modulated by a sinusoidal temperature perturbation. The advantage of temperature-modulated DSC is that, by analyzing the resulting measurement data, effects due to a *reversible* phenomenon such as a glass transition can be separated from effects due to an *irreversible* phenomenon such as enthalpic relaxation or thermosetting exothermic reaction.

A temperature-modulated DSC measurement yields three distinct curves, plotted in Figure 4: (A) the total heat flow, (B) the reversible component of the heat flow, and (C) the irreversible component of the heat flow. Curve (A) simply reproduces the results of the ordinary DSC measurement. On the other hand, inspecting the region near 60°C of curves B (reversible component) and C (irreversible component), we see in curve B a clear signature of a glass transition—allowing accurate determination of the glass-transition temperature—while in curve C we see a endothermic peak due to enthalpic relaxation. Because these two peaks occur at similar temperatures, they cannot be accurately distinguished by ordinary DSC measurements.

Finally, inspecting curve (C) near 150°C, we see that the phenomenon whose interpretation was ambiguous in Figure 3 is now clearly identified as a exothermic peak, and not a endothermic peak—suggesting that previously uncured epoxy resin cure around this temperature.

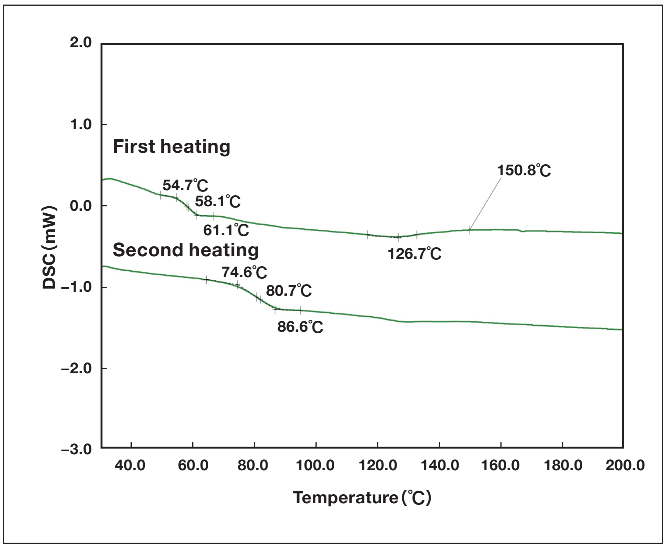

Fig. 3　**Ordinary DSC measurement data.**

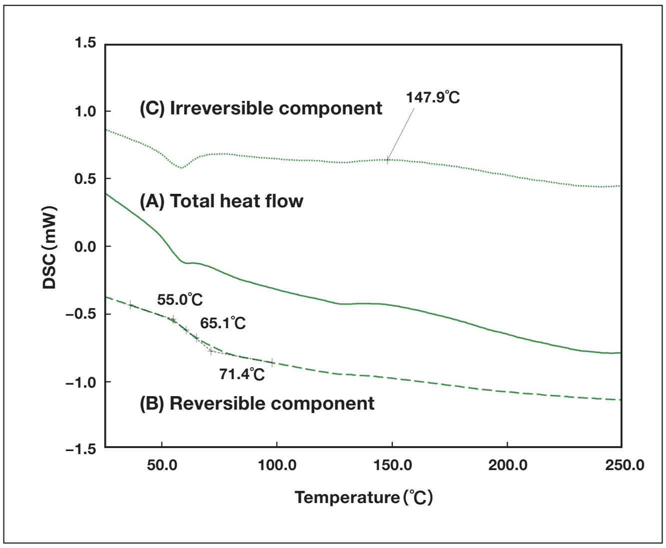

Fig. 4　**Temperature-modulated DSC measurement data.**

4. Stable Baseline Reproducibility

Instruments in the NEXTA® DSC boast two key structural features: a furnace designed with seamless junction technology extending throughout the entire apparatus—all the way from the heat sink, which constitutes the heater unit, to the cooling-system unit—and heat-insulating walls featuring a 3-layer structure made from low-heat-capacity metals. These structural features allows NEXTA® DSC systems to achieve extraordinarily high baseline stability, with a reproducibility of ±5 μW over the entire measurable temperature range, which extends from −50 to 300°C using an electrical cooling system. This allows accurate evaluation of the thermal properties of even minuscule system components.

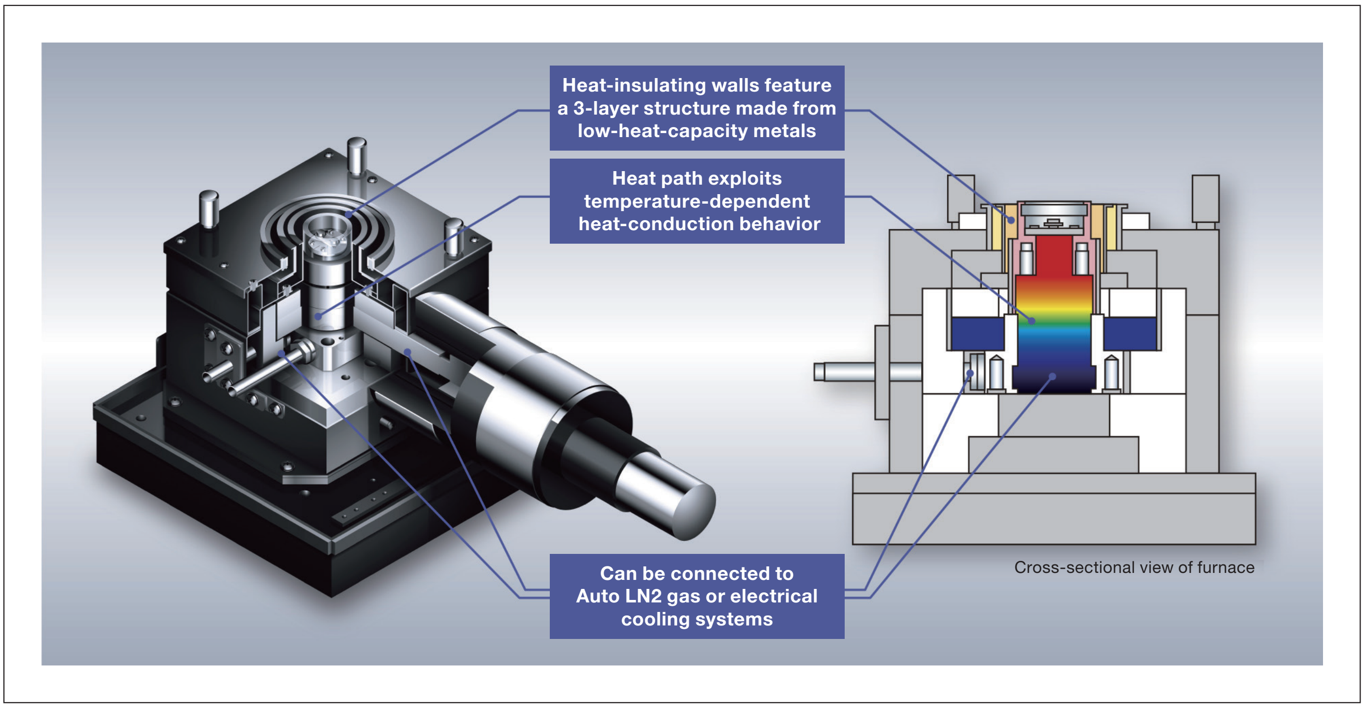

Fig. 5　**NEXTA DSC furnace structure.**

5. The Real View Unit for Sample Observation at Low Temperatures

The Real View® sample-observation thermal analysis unit enables real-time observation of samples during thermal-analysis measurements, which was not possible with previous-generation systems. Sample-observation images obtained using Real View® are time-synchronized with thermal-analysis data—for example, it is easy to view an image of a sample at the precise moment it passes through a DSC peak.

NEXTA® DSC series instruments are equipped with a high-resolution 2-megapixel camera to enable observation of localized subregions of samples, while their viewports incorporate a heating mechanism to extend the observable temperature range—restricted in conventional instruments to temperatures at or above room temperature—to temperatures as low as −50°C, deep within the low-temperature regime. In addition to allowing samples to be observed at low temperatures, this also opens the door to new methods of *color-space analysis*—quantitative analysis of phenomena that were conventionally characterized by simple visual inspection, including melting points and thermal-insulation behavior accompanying changes in sample color—to address a broader range of measurement needs.

The power of these capabilities is illustrated by an application case study involving real-time observation of an engine-oil sample during low-temperature DSC measurements to determine the cloud point. The *cloud point* of an oil, a threshold temperature below which the fluidity of the oil itself begins to change rapidly, is a key property of great interest in the oil industry—but one which, to date, has often been characterized only by visual inspection.

When engine oil is cooled at a constant rate from room temperature to negative temperatures, a exothermic peak is observed in the vicinity of −15°C. This peak is accompanied by crystallization, a transformation corresponding to the cloud point.

Visual inspection of images indicates that the sample begins to exhibit cloudiness at a temperature near −25°C, an observation corroborated quantitatively by color-space analysis: the brightness L* begins to decrease around this temperature, in conjunction with the exothermic peak. As this example demonstrates, the ability to plot brightness variations in graphical form simplifies the analysis of thermal phenomena and enables measurements at higher precision than can be achieved by visual inspection.

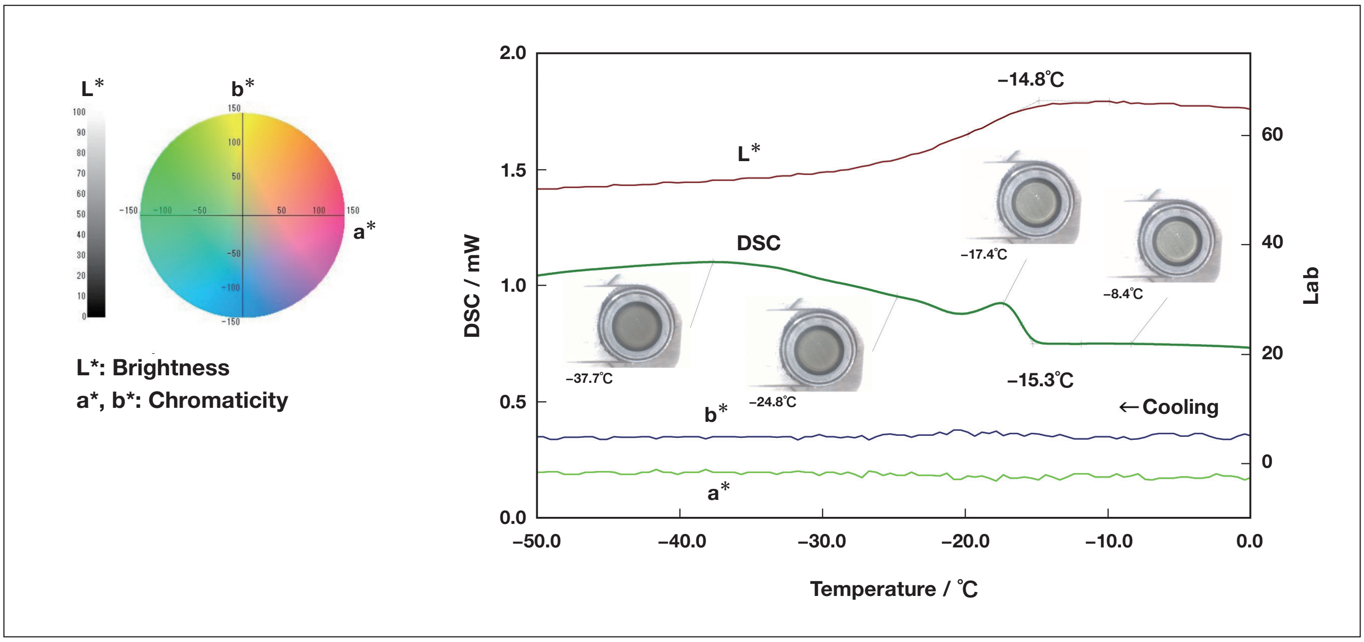

Fig. 6 Cloud-point measurement for an engine-oil sample.

6. Conclusions

The NEXTA® DSC series of thermal analyzers offers high-sensitivity measurements, stable baseline performance, and sample-observation capabilities. These instruments are ideal for high-precision measurements and for analysis or component identification of small-volume samples.

About the author

Shinya Nishimura
Focused Solution Design Department 1
Analytical Instruments Design Development Division
Hitachi High-Tech Science

SCIENTIFIC INSTRUMENT NEWS
2024 Vol.21 MARCH
Technical magazine of Electron Microscope and Analytical Instruments.
Topics

Gel Shift Assay Using DS3000 Compact CE DNA Sequencer

Noriyuki Sumida
PhD
Bio Systems Design 1st Department
Life & Medical Systems Product Division
Analytical & Medical Solution Business Group
Hitachi High-Tech Corporation

Yoshiyuki Ohtsubo
PhD
Associate Professor
Microbial Genetics and Evolution Laboratory
Graduate School of Life Sciences
Tohoku University

1. Introduction

The DS3000 Compact CE Sequencer (DS3000) is a capillary electrophoresis system featuring a high-sensitive fluorescent signal detector. The DS3000, currently marketed as a DNA sequencer, can be adapted into a capillary electrophoresis system with a broad range of applications by selecting appropriate separation media (polymers) and conditions. In particular, polymers are supplied to capillaries from pop-in cartridges that are readily installed, allowing the polymer type to be easily changed from one type to another depending on the analytical demand. Due to our innovative polymer-filling system, in which the polymer in the cartridge is supplied to capillaries through direct contact of the cartridge and capillaries, switching of the polymer cartridge does not result in waste of polymer. These product features enable flexible system operation with a different choice of polymer for each different analytical objective, making the system a powerful tool for researchers studying DNA, RNA, proteins, and etc. In this article, we demonstrate the versatile capabilities of the DS3000 by utilizing it to conduct a gel shift assay.

Gel shift assays, also known as electrophoretic mobility shift assays (EMSA), are extensively employed in molecular biology to investigate protein-DNA interactions. During electrophoresis, DNA devoid of proteins migrates at a certain speed, while when complexed with proteins, it moves at a slower pace due to alterations in size and shape. These assays have been widely utilized to study a variety of biological processes involving DNA-binding proteins, such as transcriptional regulation, DNA replication, recombination, and etc.

2. Results

2-1. Electrophoresis under non-denaturing conditions

In DNA sequencing, the DS3000 and other DNA sequencers separate single-stranded DNA under denaturing conditions by electrophoresis. Typical methods for achieving denaturing conditions include running samples at high temperatures— typically 60°C—and using polymers containing urea or other denaturing agents. In contrast, gel shift assays require electrophoresis under non-denaturing conditions to maintain DNA-protein binding. To achieve the non-denaturing conditions, it is important to choose polymers that are free of denaturing agents and to conduct electrophoresis at relatively low temperatures below 40°C.

The polymer used in this work is a POP™ conformational-analysis polymer (CAP, Thermo Fisher Scientific, 4340379) which does not contain denaturing agents. We set a low electrophoresis temperature of 40°C. The DS3000 controls the electrophoresis temperature by keeping capillaries in an oven; the oven temperature can be changed from the DS3000 control screen. In this work we set the oven temperature to its lowest possible setting, 40°C.

We next sought for a proper CAP concentration. If the CAP concentration is too low, double-stranded DNAs are not separated; on the other hand, if the CAP concentration is too high then it cannot be filled inside the capillary. After the investigation, we determined to dilute 9% stock solution to 6% with the standard electrophoresis buffer which simultaneously allows separation of double-stranded DNAs while ensuring that capillaries are filled (Figure 1A).

2-2. Electrophoresis of samples containing salts

Analysis of DNA-protein binding is often carried out in a 10-150 mM salt solution, in order to mimic the intracellular environment. However, the presence of salt in sample solutions decreases the efficiency with which analytes in sample solutions are injected into capillaries, reducing the intensity of fluorescent signals (Figures 1B,C). This is because salt reduces the electrical resistance of sample solutions, preventing the application of sufficient voltage to the sample solution during sample injection (Ref. 1). The sample-injection efficiency can be improved by modifying the sample-injection conditions. The run-control software of the DS3000 sequencer allows for the adjustment of injection time and injection voltage settings. The injection voltage and injection time are positively correlated with signal intensity, but negatively correlated with resolution (Ref. 2), and thus these sample-injection conditions must be carefully tuned to achieve a good balance between signal intensity and resolution. Figure 2 compares signal intensities obtained by sample-injection voltages of 1.6 and 6.4 kV. For an injection voltage of 6.4 kV, we achieved robust signal detection even for a sample containing 150 mM salt (Figure 2AB).

The fluorescence signal intensity is further increased by adding salt to the polymer (Figure 2C). The addition of salt reduces the electric resistance of the polymer, allowing for a higher voltage to be applied to the sample-solution portion.

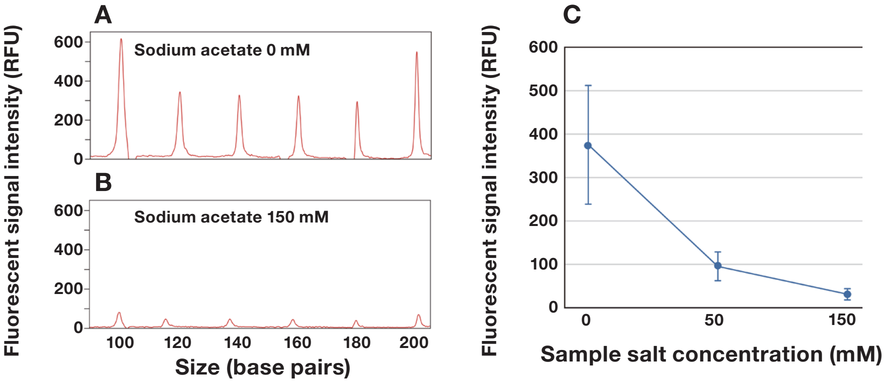

Fig. 1 Detection of double-stranded DNA via capillary electrophoresis and impact of salt concentrations on signal intensity.

A. Electropherogram obtained by analyzing a double-stranded DNA solution. A 9% CAP stock solution was diluted to 6% with an electrophoretic buffer for this run.

B. Electropherogram obtained after adding 150 mM (final concentration) sodium acetate to double-stranded DNA solution. Although peaks can be observed, the signal intensity is lower than in plot A.

C. Relationship between the signal intensity and sample salt concentration. Plotted values are average intensities of 44 peaks obtained over two electrophoresis runs. The signal intensities represent peak heights computed using GeneMarker v3.0.1 (SoftGenetics). Electropherograms are shown only for lengths ranging from 100 to 200 base pairs.

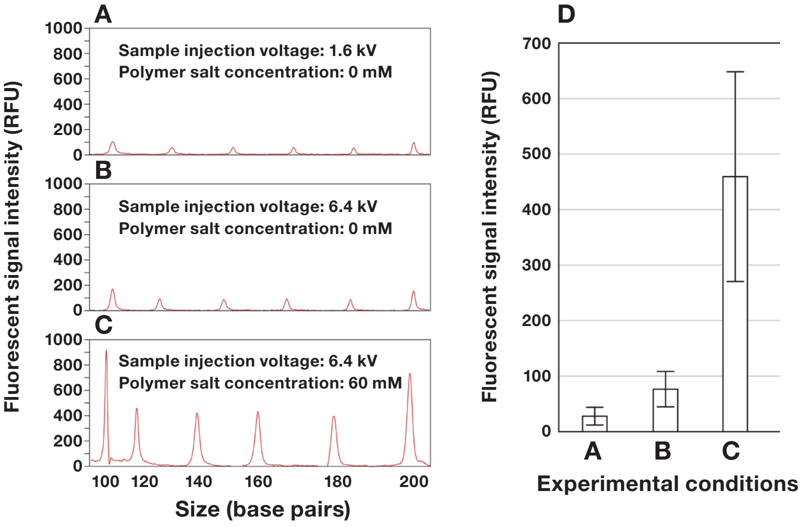

Fig. 2 Injection efficiency for salt-containing samples.

A-C. Electropherograms obtained by analyzing double-stranded DNA in a solution containing 150 mM (final concentration) sodium acetate. Sample-injection voltages and polymer salt concentrations are indicated in each subplot. Electropherograms are shown only for lengths in the range of 100-200 base pairs.

D. Mean values of 88 peak signal height obtained from 4 electrophoresis runs under various conditions. Error bars indicate standard deviations. Labels A-C corresponds electrophoresis conditions (sample-injection voltage and polymer salt concentration) in panels A to C.

2-3. Gel shift assay using BphS protein

BphS protein is a transcription repressor that binds to specific DNA sequences. The interaction between BphS protein and a specific DNA sequence (pE promoter) has been studied in detail and serves as an excellent model system (Ref. 3). In electrophoresis runs carried out under the conditions indicated in Figure 3, we observe the emergence of two peaks as the concentration of BphS protein increases. These shift peaks were observed at BphS concentrations of 45 nM and higher. All of these observations agree with the results reported in Ref. 3. These findings highlight the capability of the DS3000 to measure the binding of BphS protein to the pE promoter.

3. Conclusions

This report demonstrates that the DS3000 can be used to conduct gel shift assays. Using the DS3000 for this purpose offers several advantages, including the following:

1. It allows for easy setup of the electrophoretic system: Runs can be prepared simply by inserting a polymer cartridge into the designated position on the DS3000. This eliminates the need for handling toxic acrylamide and the necessity of hardening gels.
2. It eliminates the need to manually track electrophoresis: All fluorescent signals detected during electrophoresis are automatically recorded minimizing the risk of missing desired signals due to overrun, as can occur with traditional gel electrophoresis.
3. It automates all operations beyond the sample-preparation stage: Simply load the sample, then wait for results.

4. Experimental Conditions

To prepare the polymer, we purchased POP Conformational Analysis Polymer (concentration 9%; Thermo Fisher Scientific, 4340379), then diluted the polymer concentration to 6% by adding water together with 310 And 31xx Running Buffer, 10× (Thermo Fisher Scientific, 402824). (The final concentration of Running Buffer was 1×.) 310 And 31xx Running Buffer (final concentration 1×) was also used as an electrophoresis buffer. DNA used for the gel shift assay (pE promoter) and BphS protein were prepared following the procedure described in Ref. 3.

DNA-protein complexes were formed using 0.1 nM DNA in 0.1× PBS with various concentrations of BphS protein (listed in Figure 3). The size standard we use is an ILS600 (Promega®, DG1071). Electrophoresis was carried out at an applied voltage of 13 kV and an oven temperature of 40°C.

The sample injection conditions are indicated in the figures above. The peak-waveform plots in Figures 1 and 2 were prepared based on numerical data from individual frames obtained via GeneMarker v3.0.1 (SoftGenetics); this software package was also used to compute the peak heights used to calculate fluorescence signal intensities. The electrophoresis diagrams in Figure 3(A, B) were prepared using TraceViewerForMolecularBiology (Ref. 4).

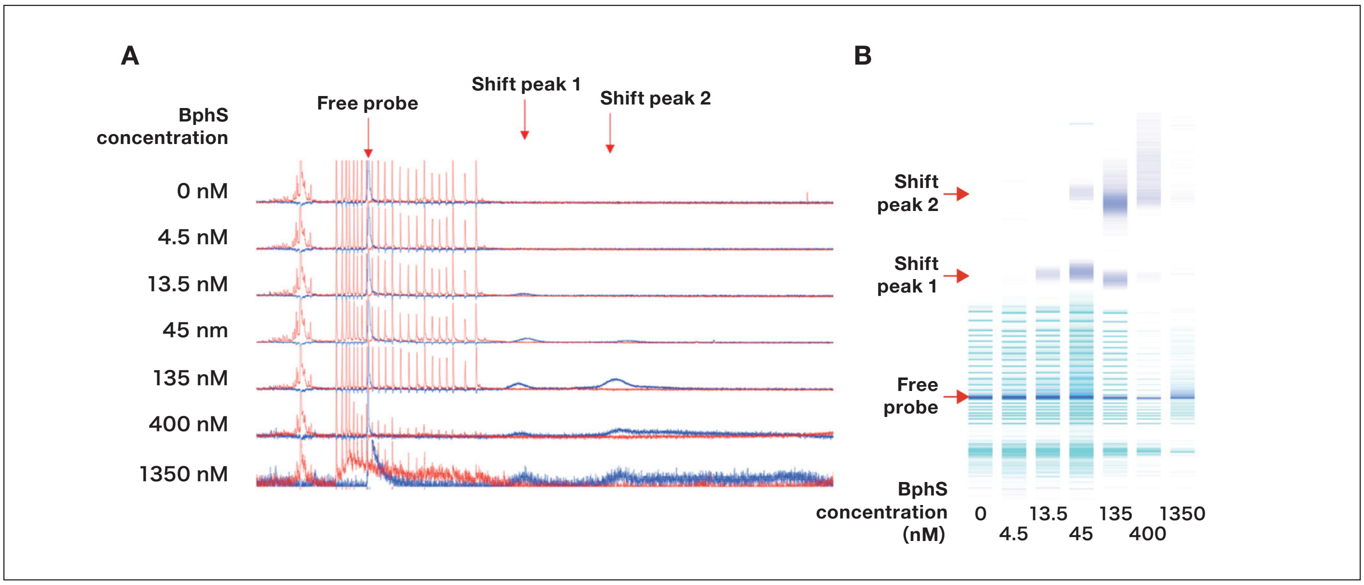

Fig. 3 Analysis of interactions between BphS and DNA (pE promoter).

A. Electropherograms obtained by electrophoresis of a solution containing BphS protein and pE promoter. Red peaks indicate signals from the size standard. Blue peaks indicate signals from the pE promoter DNA.

B. Gel-like image. Cyan peaks indicate signals from size standard. Blue peaks indicate signals from pE promoter DNA. At BphS concentrations of 45 nM and higher 2 shift peaks were observed. The label "free probe" indicates signals from pE promoters unbound to BphS, while the shift peaks indicate signals from pE promoters bound to BphS. Signals from the size standard grow weaker as the concentration of BphS protein increases, which could be attributable to salt contained in the protein solution. The sample was injected under an applied voltage of 9.6 kV with an injection time of 9 s.

References

1) Society of Genome Microbiology, Japan, Newsletter No. 25 (in Japanese)
https://www.sgmj.org/pdf/newsletter/sgmj_no25.pdf

2) Effect of sample injection conditions on performance of DS3000 Compact CE Sequencer
https://biz.hitachi-hightech.com/sinavi/ASI_ContentDistribution?viewLanguage=en_US&id=a102x0000020lq7AAA&fileId=05D2x0000004xNOEAY
A (free) registration procedure is required to view this document.
Please use the following link to register:
https://www.hitachi-hightech.com/global/en/support/sinavi/

3) Ohtsubo Y., Delawary M., Kimbara K. *et al.*, BphS, a Key Transcriptional Regulator of bph Genes Involved in Polychlorinated Biphenyl/Biphenyl Degradation in Pseudomonas sp. KKS102, *J. Biol. Chem.*, **276** (39), 36146-36154 (2001).

4) Ohtsubo Y., Nagata Y., Tsuda M., Efficient N-tailing of blunt DNA ends by Moloney murine leukemia virus reverse transcriptase, *Scientific Reports*, **7**, 41769 (2017).

The gel shift assay performed in this work involves using the DS3000 in ways that differ from standard operating procedures. Readers interested in further details of this technique are encouraged to contact Noriyuki Sumida at Hitachi High-Tech Corporation.

SI NEWS
INTERVIEW

Vol. 24

A Chance Encounter with Ionic Liquids Yields a Strong Bond to the World of Electron Microscopy

The Development of Real-time Methods for Observing Chemical Reactions

Professor Susumu Kuwabata is Dean of the Osaka University Graduate School of Engineering and Director of Osaka University's Research Center for Ultra-High-Voltage Electron Microscopy; his specialty is electrochemistry, and he has professed a boundless love for electron microscopy. We asked Professor Kuwabata to discuss his research—and how he came to be involved with electron microscopy.

Dr. Engineering
Dean, Graduate School of Engineering
Director, Research Center for Ultra-High-Voltage Electron Microscopy
Osaka University

Susumu Kuwabata

Osaka University: A pioneering institution pulling Japan into the modern era of electron microscopy

The expansive grounds of Osaka University's Suita Campus are home to one particularly distinctive building exuding an unmistakable sense of history: the Research Center for Ultra-High-Voltage Electron Microscopy.

The long history of electron microscopy at Osaka University (OU) dates all the way back to the completion of Japan's first electron microscope in 1939. Later, OU also played a pioneering role in leading Japan into the era of ultra-high-voltage electron microscopy: in 1970, a joint team of researchers from OU and Hitachi Central Research Laboratory developed the world's first ultra-high-voltage electron microscope—with a standard operating voltage of 2 million volts—and installed it at the Suita Campus. This was the impetus for the founding, in 1974, of the Research Center for Ultra-High-Voltage Electron Microscopy as a campus-wide shared educational facility.

The Research Center for Ultra-High-Voltage Electron Microscopy at Osaka University's Suita Campus was founded in 1974. Today, the Center is a campus-wide shared educational facility used by researchers in a wide range of academic disciplines.

Today, the Center is home to some 20 electron microscopes, ranging in size from small to large and crowned above all by one prize possession: the H-3000, a 3-million-volt ultra-high-voltage system developed by Hitachi Central Research Laboratory. These instruments are used by OU researchers spanning a diverse spectrum of scientific and engineering fields to investigate specimens ranging from inorganic materials to biological samples. The Director of the Center is Professor Susumu Kuwabata, who also serves as the Dean of OU's Graduate School of Engineering.

Professor Kuwabata describes the H-3000 this way: "This microscope boasts the highest accelerating voltage of any ultra-high-voltage electron microscope in the world, and one of its key features is that its electron beam can pass through even the thickest specimens to yield high-resolution microscope images. More specifically, depending on the type of specimen, the beam can pass through biological samples with thicknesses on the order of 10 microns and through inorganic samples with thicknesses on the order of 3-5 microns. For example, blood vessels have circular cross sections, and conventional electron microscopes weren't able to see anything but just plain rings. But the realization that there was some thickness there finally allowed the first observation that in fact we were looking at tubes. And there are many other examples like this, where the ability to observe thick specimens allowed new things to be understood for the first time. The ability of the H-3000 to acquire 3-dimensional images by rotating specimens during observation is another major advantage."

Today, ultra-high-voltage electron microscopes like the H-3000 are installed not only at OU but at many other universities as well. This has spurred the creation of a nationwide network of universities possessing these instruments, who come together to share a broad diversity of microscopy images. Efforts are also in progress to develop remote-control protocols through which ultra-high-voltage electron microscopes can be used by researchers at universities and other institutions lacking systems of their own.

The H-3000 electron microscope at OU's Research Center for Ultra-High-Voltage Electron Microscopy is a 3-million-volt system developed by Hitachi Central Research Laboratory. Images acquired by this instrument may be shared not only among users of the Center, but more broadly through a nationwide consortium of universities equipped with ultra-high-voltage electron microscopes.

Focusing on the non-volatility of ionic liquids

Professor Kuwabata specializes in *electrochemistry*, a branch of chemistry that studies chemical reactions induced by electron-motion between substances and chemical species. Electrochemistry encompasses the study of common devices such batteries and of familiar phenomena such as electrolysis and artificial photosynthesis.

But how did electron microscopy become a tool so near and dear to Kuwabata's heart? Kuwabata credits a chance encounter with *ionic liquids*. Discovered in 1914 by the chemist Paul Walden (1863-1957), ionic liquids are varieties of salts that can stay as liquids even at room temperature; here the term “salts” refers to compounds consisting of positive ions electrostatically bound to negative ions. Most salts, including common table salt (sodium chloride, $NaCl$), are solids at room temperature, and for this reason it was long believed that *all* salts share this property; indeed, ionic liquids continued to attract minimal attention for many years following Walden's discovery, and it wasn't until the 1990s, with the development of ionic liquids that remain stable in air, that interest in ionic liquids began to explode. "It was around this time that I first learned of the existence of ionic liquids, and I found them incredibly fascinating," Kuwabata explains. "Of course, my fellow electrochemists were all thinking about applications to electrolytic solutions, whereas my ideas"—as he recounts with an impish glint in his eye—"went in a very different direction."

Kuwabata focused on what he saw as the single greatest advantage of ionic liquids: their *non-volatility*. "Ionic liquids are the only liquids that don't evaporate," he explains. "For example, the electrical neutrality of the water molecule, H_2O, has the consequence that water molecules are easily separated from each other via boiling or evaporation. But the atoms comprising ionic liquids, although not so tightly bound as in solid salts, are nonetheless held together by strong electrostatic attractions between positive and negative ions, making them particularly difficult to separate and send off in separate directions—even when subjected to heating or vibration. So one day it dawned on me"—and here the Professor's eyes are positively *shining*—"that this non-evaporating behavior could be exploited for electron-microscope observation of specimens *as they exist in their natural state*, with no need to dry specimens for observation."

The need to preserve the high-vacuum state within electron microscopes had conventionally required observation specimens to be completely dried before they could be observed. But the ability to observe specimens immersed in ionic liquids could allow direct investigation of living organisms in their natural state—and of the progress of chemical reactions in ionic liquids. Moreover, Kuwabata reasoned that the high ionic conductivity of ionic liquids should prevent the accumulation of static charge under electron-beam irradiation, avoiding a phenomenon that could otherwise prohibit image acquisition.

Doing his best to keep his excitement in check, Kuwabata immersed a biological sample in an ionic liquid, mounted the specimen in his laboratory's scanning electron microscope, and conducted an observation. The results confirmed his hypothesis: the electron beam passed through the ionic liquid without generating static-charge buildup, yielding clear microscope images. As expected, the ionic liquid did not evaporate inside the SEM. Kuwabata's next attempted the challenge of following the detailed evolution of battery charging/discharging processes and other electrochemical reactions through real-time SEM observation. This was followed by yet another breakthrough: in 2008, Kuwabata and a research group at Nagoya University dissolved silver ions in an ionic liquid, passed an electric current through the liquid, and carried out the world's first successful observation of the dendritic growth process of silver deposits on electrode surfaces—a result that was widely heralded in newspapers and other media outlets.

Ionic liquids, which exist in liquid form at room temperature, are compounds consisting of positive ions bound to negative ions by attractive electrostatic forces. The strength of these forces ensures that ionic liquids, unlike water and most other liquids, staunchly resist evaporation—even when heated or placed in a vacuum.

Kuwabata's achievements noted in high-school chemistry textbooks

"As it turned out, placing ionic liquids in SEM specimen chambers required a little retuning of the basic SEM system," Kuwabata recalls. "So we asked the folks at Hitachi High-Tech if they could help us out, and they came up with some perfect solutions."

With a track record of successful SEM observations bolstering his confidence, Kuwabata next started thinking about using ionic liquids for transmission electron microscope (TEM) experiments. Compared to SEM, TEM offers higher resolution and higher performance—but at considerably higher cost. "So, anybody with a little common sense understood that, just because you could put one of these things in a SEM, it didn't necessarily follow that you could put one in a TEM!" Kuwabata laughs. "Back then, when I told the folks at Hitachi High-Tech that I wanted to put an ionic liquid in a TEM, they looked at me and said—'Stick an ionic liquid in a TEM? Absolutely no *way* we're doing that!' But eventually they were gracious enough to give it a try. And I still remember the moment we all saw the first TEM image of an ionic-liquid specimen—the Hitachi High-Tech guys all got really excited and kept saying 'Holy cow! This is incredible!' And ever since then," Kuwabata laughs, "I've had a very favorable relationship with the folks at Hitachi High-Tech."

"You know," he continues, "if it hadn't been for all the cooperation we got from the Hitachi High-Tech team back then, we may well have been scooped by some overseas researcher in attempting the world's first TEM observations in ionic liquids. This is another reason I've always been grateful to Hitachi High-Tech."

Kuwabata's accomplishments have even made their way into high-school chemistry textbooks. Previous-generation textbooks contained statements like "Ionic crystals, such as sodium chloride, typically have high melting points and are solids at ambient temperature and pressure." However, many newer textbooks follow the lead of Keirinkan's high-school chemistry text, which now includes a sidebar noting that "Salts existing as liquids at room temperature are known as *ionic liquids*"—and features an electron microscope image of scales on a butterfly wing captured by Professor Kuwabata.

"When that textbook arrived," Kuwabata recalls, "I immediately turned to the Acknowledgements section at the end, where they list credits for all materials supplied to the book, and, sure enough,

"My laboratory's achievements have even made it into high-school chemistry textbooks." Kuwabata says. Newer editions of the textbook in question include a sidebar discussion stating "Salts existing as liquids at room temperature are known as *ionic liquids*."

there it was, right there in print: *Kuwabata Laboratory, Osaka University Graduate School of Engineering*. I was so thrilled that I took the book into the lab and showed all my students, who were pretty excited as well—'That's so cool!' they all said. So then I asked them: 'By the way, when you guys were in high school, did you ever open your textbook to the Acknowledgements page and read all the names?' And of course they all said 'No, sir—we never even knew such pages existed!' And I said 'That's right—because the only reason these pages *do* exist is to flatter the people listed on them!' and we all laughed."

As awareness of ionic liquids continues to grow, Kuwabata says he dreams of that happy future day when their existence will merit not just sidebars—but *full sections* in chemistry textbooks.

Electron microscopes as extensions of film cameras

But how did Kuwabata first hit on the idea of putting ionic liquids in electron microscopes? "Actually," he explains, "I had been a total camera freak ever since elementary school." This was before the days of digital cameras, when photographers had to take film to photo studios to have pictures developed and printed. But young Kuwabata was developing and printing his *own* snapshots already by his first year of junior high school.

Of course, the digital cameras in modern smartphones are extremely high-performance instruments allowing anyone to take close-up shots with ease, but things weren't so easy with the film cameras of Kuwabata's youth. Capturing close-up images—of, say, a tiny insect—required specialized tools, such as close-up lenses, and the photographic skills to use them. "All through those years, from elementary school to high school," recalls Kuwabata, "my burning passion was to use film cameras to capture the microscopic world in the greatest possible detail."

But later, when Kuwabata became a student at Osaka University and belonged to a research laboratory one day, he got a big surprise—the lab was equipped with a Hitachi S450 SEM system. He asked a professor in the laboratory how to use the instrument, and was told "Just put the specimen in here and go like this to make an observation—and you can even push this button to capture an image." Kuwabata was astonished to see how easy it was

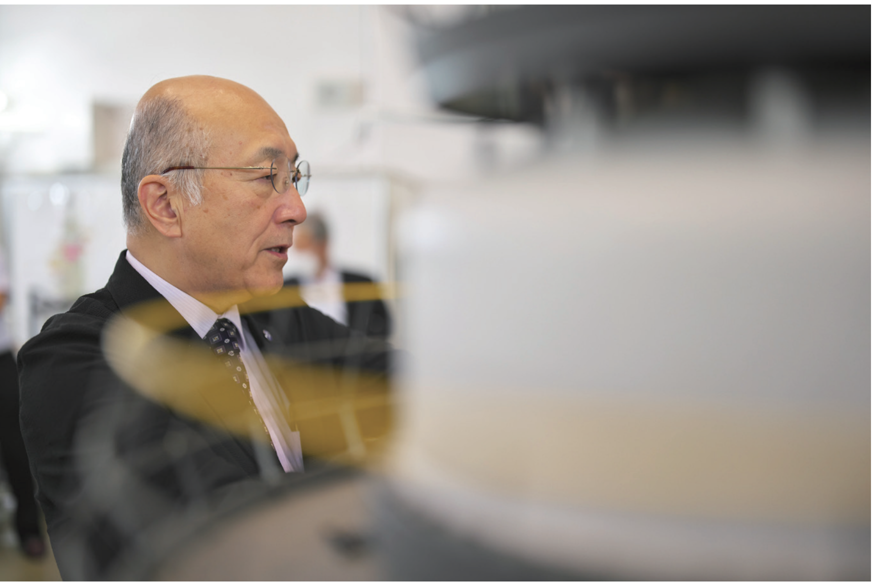

Kuwabata says he's been a total camera freak ever since elementary school—and that he sees electron microscopes as extensions of ordinary cameras.

to observe the microscopic world—and even to acquire high-resolution images with just the touch of a button.

"In our electrochemistry research, using electron microscopes wasn't something we needed to do every day, but in my heart I always held on to the hope that someday I'd use electron microscopes to capture images that would take people's breath away," Kuwabata recalls. "Because, to me, electron microscopes were just extended versions of ordinary cameras. I think that's how I wound up asking myself why I couldn't use ionic liquids for electron-microscope observations."

Choosing a life of electrochemistry research

How did Kuwabata wind up choosing electrochemistry as his field of specialty? "The experience that first got me interested in electrochemistry," he recalls, "was my discovery of batteries, probably around my 3rd year of junior high school."

At that time, most batteries were of the disposable dry-cell variety, but one day young Kuwabata came across a radio and cassette player in his house, and, reading through the user's manual, his eyes fell on the phrase *NiCad battery*—and specifically what came after: *Battery may be recharged and reused multiple times*. This was music to Kuwabata's ears: Having long been forced to save up his paltry allowance to purchase costly batteries, "now I could just charge up my batteries at home—and save my allowance!" he grinned. "Of course, at that time, NiCad batteries were pretty expensive—I remember it's around 6,000 yen. But, in the long run, it seemed obvious to me that they represented an enormous savings compared to disposables."

Kuwabata treasured his precious NiCad batteries so much he barely used them—and yet, after constant recharging, the devices stopped working after just a month or so. "It wasn't until after I became an electrochemistry researcher that I learned that NiCad batteries quickly stop working after repeated recharging," he recalls. "I hadn't understood this back in junior high school, and I found it so incredibly disheartening that I vowed, right then and there, to build a battery someday that could be recharged over and over again without ever breaking down."

Kuwabata's high-school years were rocked by another calamitous event: In 1973, the oil-producing nations of the Middle East raised crude-oil prices by 70%, plunging Japan into a full-blown oil shock. Amid the ensuing search for alternative energy sources, the discovery of the Honda-Fujishima effect cast a bright spotlight on research into photocatalysts as ideal sources of energy. This effect involves a titanium-dioxide electrode and a platinum electrode immersed in water; when light shines on the titanium-dioxide electrode, the water decomposes to yield oxygen and hydrogen, generating a flow of current between the electrodes. The possibility of a revolutionary new technology, capable of converting light energy simultaneously into electrical energy and chemical energy, became a focus of intense global interest—and, to this day, Kuwabata still has several carefully-preserved newspaper articles from that time. "That's what convinced me I wanted to major in something at college that would give me a chance to study batteries and photocatalysts," Kuwabata explains. "And it was right around then that my father gave me a pamphlet for Osaka University, and right there on the page for the Applied-Chemistry Major in the School of Engineering was the word *electrochemistry*! I said, yes! This is it! This is exactly what I want to study!"

Kuwabata eventually got his wish, entering the Osaka University School of Engineering and majoring in applied chemistry. What sort of research did he pursue? "In battery research, interfaces between solid electrodes and liquid electrolytes are extremely important," Kuwabata explains. "And yet, what's surprising is that, if you look at these interfaces under electron microscopes, you can't tell where the solid ends and where the liquid begins—the boundary is actually quite fuzzy. In fact, the boundary between liquid and gas isn't very clear either. The professor in the laboratory I joined used to say 'If you think of it like an ocean, then these interfaces are like the beach.' When waves come in, there's a moment when you can't tell where the ocean ends and where the sand begins—and interfaces in batteries are very similar. So that got me interested in studying interfaces in batteries and other systems."

Interfaces in batteries are crucial indeed—the scant few nanometers of interface between electrodes and electrolytic solutions are responsible for generating current flows, and thus, without the ability to observe interfacial phenomena, it is nearly impossible to understand the mechanisms governing power generation. This was the impetus that made Kuwabata so eager to observe solid/liquid interfaces with electron microscopes. Of course, at the time, the notion of inserting liquids into electron microscopes was totally unheard of, and it would be another ten-plus years before Kuwabata experienced his fateful encounter with the world of ionic liquids.

Continuing to solve energy problems —well beyond retirement

Professor Kuwabata retires in 2023 academic year, but says he plans to continue working on energy problems.

At present, Japan's Ministry of Education, Culture, Sports, Science and Technology, together with the Japan Science and Technology Agency (JST), are promoting a program known as Green Technologies of Excellence (GteX), to be implemented over a five-year interval beginning in October 2023. Amid efforts toward carbon neutrality from nations around the world and a rapid growth in investments targeting green transformation (GX), GteX represents a collaborative effort among Japanese government, academia, and industry players to create new technologies and train new leaders to promote GX innovations and achieve carbon neutrality by 2050. More specifically, GteX focuses on three specific sectors—*revolutionary batteries* (*energy-storage technology*), *hydrogen-conversion technology*, and *biomanufacturing technology*, and Professor Kuwabata serves as a Program Officer (PO) in the revolutionary-batteries sector.

"Going forward, I'm hoping to continue using electron microscopes for electrochemistry research, while helping to supervise researchers working today in R&D for revolutionary new types of batteries," Kuwabata explains with an air of fierce commitment. "I am not at all ready to just kick back and relax!"

Professor Kuwabata poses in front of the H-3000 ultra-high-voltage electron microscope.

Reported and written by Kumi Yamada. Photographs by Yuki Akiyama.

SI NEWS

INTERVIEW

Vol. 23

The Challenge of Observing Physical Phenomena via Electron Microscopy

V-shaped double-slit electron-interference experiments bring scientists one step closer to understanding mysterious wave/particle duality

RIKEN Senior Scientist Ken Harada, in collaboration with Osaka Metropolitan University, Meijo University, and Hitachi, has conducted experiments probing wave/particle duality. The results of these experiments, conducted from 2018 to 2019, bring us one step closer to understanding the mysterious wave/particle duality of quantum mechanics—and promise to help clarify the relationship between interference and electron propagation trajectories. We asked Dr. Harada to explain how he uses electron holography to see exotic physical phenomena.

**Senior Scientist,
Emergent Phenomena Observation Technology Research Team,
RIKEN Center for Emergent Matter Science,
RIKEN**

Ken Harada, PhD

In 1991, Ken Harada completed his PhD in applied physics at the Osaka University Graduate School of Engineering and joined Hitachi Advanced Research Laboratory, where he worked on observing magnetic flux quanta in superconductors. From 2001 to 2007 he was assigned to RIKEN's Frontier Research System, where he assembled the research team that later evolved into his current research team, focusing on the development of biprism-based optical systems for two-stage electron beams. In 2015 he joined RIKEN, where his research interests have included double-slit experiments, electron vortex beams, and schlieren optical systems.

Experimental Results Offer Clues for Which-way Experiments

According to quantum mechanics, electrons have both wave-like and particle-like properties, but the laws of nature seem to prohibit these two types of properties from being measured simultaneously. Perhaps for this reason, the results of double-slit experiments have never moved beyond "exhibiting the mystery of wave/particle duality." The notion that individual electrons—which are only detected as particles—could simultaneously pass through two slits seems far removed from everyday human intuition. Indeed, if electrons are particles it should be possible to trace the trajectories of their motion, and this reasoning has motivated many researchers to conduct experiments using a broad array of instruments and techniques. For double-slit experiments with particles, one strategy is to detect interference fringes after determining which slit the particle passes through; experiments based on this approach are known collectively as which-way experiments.

With the goal of clarifying the relationship between electron trajectories and interference phenomena, Harada and his collaborators began experiments in 2017 using a holography electron microscope, which offers access to the highest-coherence electron beams available in the world today.

"I'm targeting the very observation of physical phenomena themselves," Harada explains, "and to that end I've thought endlessly about questions like how to exploit highly coherent electron waves, how to assemble rational optical systems, and what sorts of physical phenomena we should optimize our apparatus to observe."

In 2018, the researchers used a 1.2 MV field emission transmission electron microscope (FE-TEM) to conduct an asymmetric double-slit interference experiment, with biprisms controlling the width of each slit. To determine which slit an electron passed through, they used pre-Fraunhofer conditions corresponding to reductions in the travel distance from the double slit to the image plane; however, when interference fringes form, it becomes impossible to distinguish which slit the electron passed through. This is because, when electrons behave like waves, they are diffracted after passing through the slits even if the propagation distance is short, creating interference between pairs of electron waves. This illustrates the difficulty of controlling interference when electron waves propagate naturally, and Harada says it was their desire to solve this problem that led the team to devise an optical system operating under in-focus conditions.

The experiments mentioned in the title proceeded as follows.

In the FE-TEM system, two electron biprisms were placed beneath the objective lens to control and superpose waves; this gave the researchers control over interference fringes consisting of dot images. Then they used a V-shaped double slit to observe and record interference phenomenon—under pre-interference conditions, interference conditions, and post-interference conditions—via a direct-detection camera system.

"We set up an electron-optics system in which our V-shaped double slit allowed us to observe all three interference conditions (pre-interference, interference, and post-interference) simultaneously in a single field of view," Harada explains. "The upper biprism was positioned on the image plane of the double slit used to deflect the propagation of waves placed at the objective plane. The lower biprism was positioned between the objective lens and the image plane to deflect waves in such a way as to ensure that the two waves overlapped to produce a slit-shaped pattern on the image screen. Thus we designed an electron-wave double-slit experiment in which the double-slit positions produced an image precisely at the detector surface under conditions corresponding to zero propagation distance in the optical sense."

As a result, the team concluded that interference fringes could be observed only when information on the trajectories of individual electrons could not be obtained.

Ken Harada at the controls of a Hitachi HF-3300S TEM system. In the darkened microscopy laboratory, Harada inspects captured images with an intimidating intensity of focus.

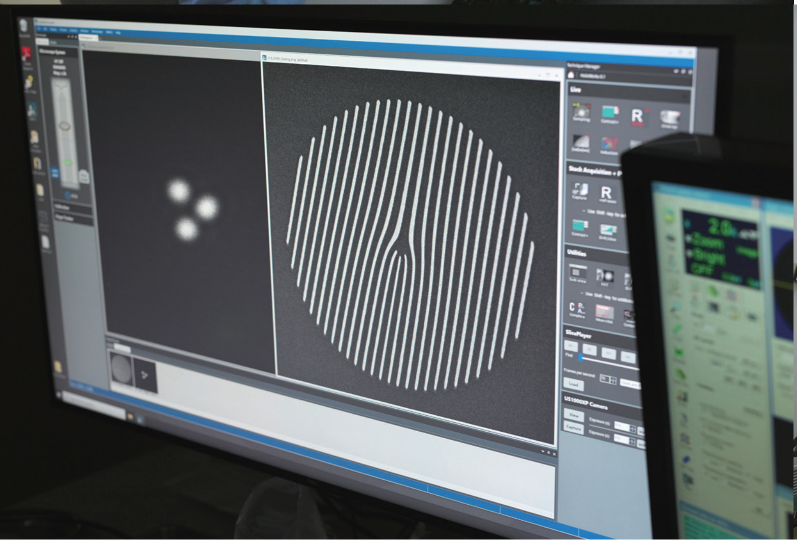

An Idea for Observing Magnetic Flux Quanta Redefines the Term Performance

As it turned out, it was another double-slit experiment that set Harada on the road to his current research using electron microscopes. This experiment, conducted by the late Akira Tonomura—a Hitachi fellow—clearly demonstrated wave/particle duality and showcased the mysterious nature of quantum mechanics. In 1987, while a master's course student at Osaka University, Harada saw a movie of Tonomura's experiment at a physics conference in Nagoya—and remembers to this day the shock it delivered.

"To save money, I bought a discount railway ticket and traveled to Nagoya on a rickety local train that departed Osaka at 4 AM," Harada recalls. "The moment I joined Hitachi Advanced Research Laboratory in 1991, I found Dr. Tonomura and told him I wanted to perform that experiment," Harada recounts with a smile, "and he said 'Whoops! I already threw away that camera.'"

Thereafter, Harada began his career as a researcher working under Tonomura, with an initial assignment to observe magnetic flux quanta in superconductors.

"At that time, there were instances in which superconducting materials been observed, but we were the first in the world to take on the challenge of observing the actual phenomena," says Harada. "When I started my experiments I wasn't sure if I would be able to see anything or not, but Tonomura said 'Well, if the conclusion is that the phenomenon is unobservable, then that's the conclusion—but don't ask me to bail you out when someone else succeeds in observing it!' Happily, the experiment was successful, and in 1992 we observed magnetic flux quanta in the conventional superconducting metal niobium. After that we turned our attention to Bi-based high-temperature superconductors, and in 1993 we successfully carried out a dynamical observation of magnetic flux quanta in a high-temperature superconductor."

In high-temperature superconductors, superconductivity occurs at the temperature of liquid nitrogen, which is much easier to work with than the ultra-low temperatures required for conventional superconductors. However, one problem is that electrical current flows can produce Joule heating, which may destroy the superconductivity. It was considered that Joule heating is caused by the motion of magnetic flux quanta, and the successful observation of the dynamics of such quanta was a major breakthrough that sent shockwaves throughout the research field.

Harada recounts this achievement with humility: "Of course this was not just my work—it was built on a foundation created by many previous experiments. I just happened to receive the final handoff of the baton—and had the good fortune to get involved at precisely the right time." Harada's breakthrough clearly represented dramatic progress, but further conceptual advances were needed to achieve the goal of using electron microscopes—originally developed to observe materials—for the purpose of observing phenomena.

"Of course, if you want to look at smaller materials, increasing the magnification is the

The 1 MV holography electron microscope. Akira Tonomura scoured Japan to find a site with the optimal geology and environment for this instrument, and eventually settled on its current location, Hatoyama. The instrument was built on a foundation of extremely hard ground rock.

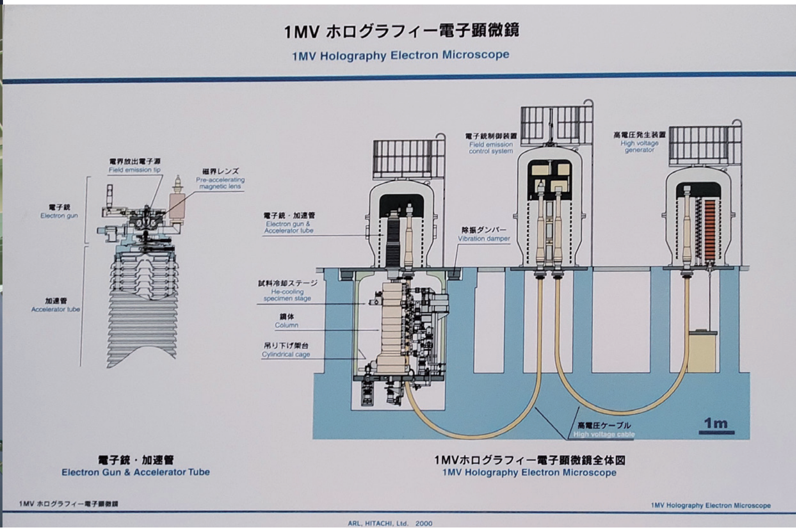

obvious thing to do," Harada notes. "What was truly revolutionary here was that we did the opposite: we worked at low magnification—less than 100×—and worked to improve the parallelism of the world's highest-coherence electron beam. Dr. Tonomura's realization that direct observation of physical phenomena wouldn't require high magnification redefined the meaning of the term performance."

Torrential Cascades of Ideas Reveal a Spirit of Intellectual Adventure

Harada's research style is to conceive of a technique for observing some subject, develop an experimental apparatus, and use it to observe a physical phenomenon—the phenomenon itself—that nobody had seen before. Keiko Shimada, a member of RIKEN technical staff, says that Harada "is passionate about seeing things—when he gets an idea he can't rest until he's tried it out." Harada admits as much: "Sometimes it occurs to me that if I just do things a little differently, a goal that was previously out of reach may suddenly become achievable—and when that happens I get very excited and start making all sorts of requests—and since I can't help but want to attempt it, I end up asking them to do various things for me.

In response, "He has so many ideas that it's very important for me to write them down so I don't forget them," she notes with a smile.

Today's world tends to emphasize and reward rapid results, but too much focus on the short term will eventually deplete our store of fundamental knowledge. What drives Ken Harada as a researcher seems to be a powerful spirit of adventure—a desire to see and learn about new things without known precedents, even if it's unclear what benefits may result.

The technology that connects Harada to Hitachi is the holography electron microscope (HEM). In this specialized type of electron microscope, designed to take maximal advantage of the wave nature of electrons, a base transmission electron microscope

Harada confides that he considers all work in the field of electron-wave interference to be something that he should be doing. Even with regard to double-slit experiments, his passion for research knows no bounds: "You can't be satisfied with simply achieving a demonstration."

(TEM) system is equipped with a field emission electron gun emitting a high-brightness, high-coherence beam of electrons, together with electron biprisms to deflect this beam. By exploiting the phase change that occurs when electron waves pass through electromagnetic fields, HEMs can measure electromagnetic fields and related phenomena with high sensitivity and atomic-scale resolution.

Tonomura developed the world's first practical system in the 1970s and went on to develop higher-performance versions that notched up a number of key accomplishments in physics, including Harada's observation of magnetic flux quanta in superconductors.

Center for Exploratory Research is surrounded by an expanse of untrammeled nature, with wild weasels and raccoon dogs making frequent appearances.

The history of electron microscopy dates back to the early 20th century, with the first instrument developed in Germany in 1931. In Japan, where information from the outside world was hard to come by during World War 2, a national development effort led to Hitachi's first prototype in 1941 and, in 1942, to the market launch of Japan's first commercial electron microscope, the Hitachi HU-2.

"The fact that Japanese researchers had to think through everything, starting from scratch, turned out to be very useful for the later development of the technology," says Harada. "I agree with the late Noboru Masuko, an Emeritus Professor at the University of Tokyo, who said 'With technology, you don't necessarily need to be its parent, but if you don't have memories of it from the cradle then it won't bear fruit.'"

Using Electron-wave Interference to Demonstrate Violation of Bell's Inequality

In the V-shaped double-slit experiment mentioned above, the operating positions of the two electron biprisms were rigorously defined by electron optics, a point that Harada says was a subject of vigorous discussions. Harada hoped not only to repeat an experiment he had witnessed over 30 years earlier, but to create his own—more advanced—version, a purpose for which Hitachi technology provided no small amount of assistance.

"In the absence of electron-wave interference, we had the information needed to determine whether the electron passed through the left or the right slit," Harada explains. "Our understanding had progressed at least that far. Of course, demonstrating this still required surmounting some rather tall hurdles, but my view is this: You may not be as smart as Einstein or Bohr, but as long as you have an electron microscope and a camera then you're able to do experiments. And if you're able to do experiments, then declining that challenge is really not an option."

Thanks to recent technological advances, double-slit phenomena—long the province of thought experiments devised by ingenious theorists and accessible only by sophisticated, groundbreaking experimental techniques—are slowly shedding their exotic mystique and acquiring a more realistic real-world flavor. Ken Harada, for one, gives every indication of having become even more motivated by these developments.

"The experimental demonstration of quantum entanglement, which won the Nobel Prize for Physics in 2022, was based on experiments using photons," he notes, then continues with a note of resolve: "This may sound like a pipe dream, but I'd love to try using electrons to demonstrate violations of Bell's inequality."

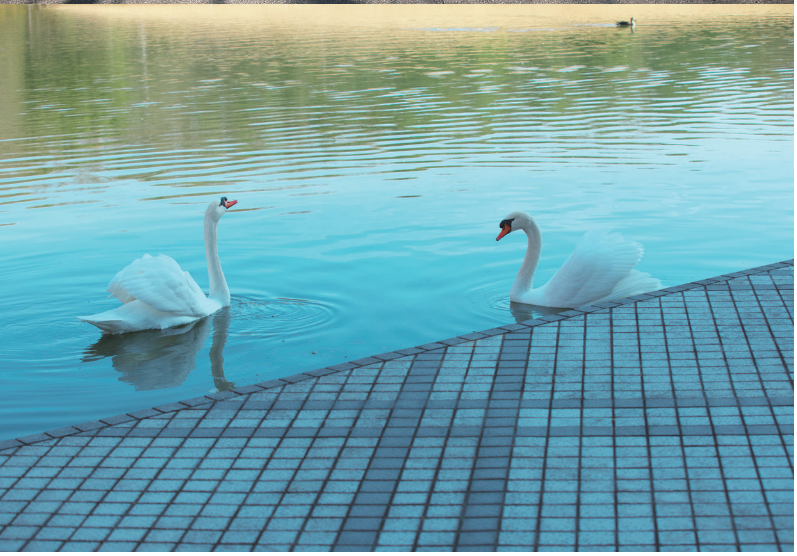

Editor's Postscript

Double-slit experiments and wave/particle duality, which so captivated a young Ken Harada traveling to Nagoya on discount rail tickets, have been a subject of continuous experimental inquiry for more than half a century—and it's easy to see why: exploring and interpreting phenomena that so thoroughly confound our everyday intuition is no simple task. And yet, in facing such deep riddles, Harada's motto—"If you're able to do experiments, then declining that challenge is really not an option"—seems to me a perfect crystallization of the researcher's mission and mindset. Which slit did the particle pass through? Reporting this story leaves me eagerly awaiting the day when this question finally finds an answer.

(Reported and written by Toshinari Yamaguchi;
photography by Yuki Akiyama.
Interviewed on January 13, 2023)

Hitachi High-Tech Corporation